DISSERTATION SUBMITTED IN PARTIAL FULFILMENT FOR THE REQUIREMENT OF THE DEGREE MAGISTER TECHNOLOGIAE IN THE FACULTY OF APPLIED AND COMPUTER SCIENCES AT VAAL UNIVERSITY OF TECHNOLOGY

BY

Ms. Nokhanyo Mbewana (215238729)

Supervisor:

Prof. Makwena Justice Moloto (MSc: UWC, PhD: UZ)

Co-Supervisors:

(1) Dr. Kalenga Pierre Mubiayi (MSc & PhD: WITS)

(2) Dr. Fanyana Mthunzi (MSc & PhD: NWU)

DECLARATION STATEMENT

I hereby declare that the work on "Antimicrobial activity of the synthesized copper chalcogenides (copper oxide, copper sulphide and copper selenide) nanoparticles and plant extracts" is my work and all sources used are acknowledged by referencing.

Student: N.G. Mbewana

Signature……..... **Date……**

Supervisor: Prof M.J. Moloto

Signature……..... **Date……**

ABSTRACT

Chemical precipitation method is the most widely used of all methods for preparing good quality semiconductor nanoparticles. Several conditions are optimized for producing the desired size and shape of particles. The parameters such as capping molecule, precursor concentration, time and temperature were investigated using the colloidal hot injection method. The effect of capping agent was the first parameter investigated in the synthesis of copper selenide, copper sulphide and copper oxide nanoparticles. The capping agents of interest in this study were oleylamine (OLA) and trioctylphosphine (TOP), due to their ability to act as reducing agents, surfactant, solvent and enhancement of colloidal stabilization. The use of oleylamine and trioctylphosphine were carried out at 220 °C for 30 minutes. The optical and structural properties of the yielded nanoparticles were characterize using UV/Vis spectroscopy, TEM and XRD and showed dependence on the type capping interactions from the two agents. Nanoparticles synthesized using TOP produced two phases whereas a single phase was observed from OLA as confirmed by XRD. OLA produced bigger particle sizes compared to TOP but with a wider variety of shapes. The wide variety of particle structures of OLA capped nanoparticles was advantageous since different types of bacteria were targeted in this work. Therefore, other synthetic parameters were investigated using OLA as both solvent and capping molecule.

Precursor concentration ratio showed bigger effect in the size, and shape of the yielded nanoparticles. For copper selenide and copper sulphide (Cu: Se/ S), 1:1 concentration ratio gave the best optical and structural properties while copper oxide (CuO) nanoparticles demonstrated its best optical and structural properties in 2:1 ratio (Cu: O). Nonetheless, 1:1 precursor concentration ratio was used to optimise other parameters. Since reaction time has a profound effect on the nanocrystals size and shapes, the effect of reaction time in OLA was also investigated. The reaction time showed no effect on the phase composition of the synthesized copper sulphide, copper oxide and copper selenide nanoparticles. Reaction time of 30 minutes gave the best optical (the shape of the absorption band edge and emission maxima values) and structural (size distribution of particles) properties for CuSe and CuS compared to other reaction times (15 min, 45 and 60 min). 15 min reaction time gave the best optical and structural properties for copper oxide but nonetheless, 30 min was used as the optimum reaction time for further optimization.

Temperature showed an effect in size, shape and the stoichiometry of the reaction. These effects were confirmed by the optical and structural properties of the synthesized nanoparticles. XRD patterns revealed some differences with the temperature change, indicating an effect on the phase composition of CuS and CuO but not on CuSe nanoparticles. CuSe and CuS nanoparticles synthesized at 220 °C gave the ideal optical and morphological features compared to other temperatures that were selected (160 ºC, 190 ºC and 240 ºC). Nonetheless, CuO revealed its best optical and structural properties at 160 ºC. 220 ºC was deduced to be the optimum temperature for the synthesis of these three materials under the synthetic conditions. The optimum parameter (220 ºC, 30 min and 1:1 ratio) were used to synthesize the three copper chalcogenides which were then tested against Gram-negative (*E. coli* and *P. aeruginosa)*, Gram-positive (*S. aureus* and *E. faecalis*), and fungi (*C. albicans).*

The plant species, *Combretum molle* and *Acacia mearnsii* were phytochemical screened for the presence of active organic compounds and the content of total phenols, flavonoids and antioxidants using different solvents. Both *C. molle* and *A. mearnsii* revealed the highest phenolic content in acetone extracts. *C. molle* revealed its highest flavonoid content in methanol extract and its highest free radical scavenging activity in acetone extract. Acetone extracts demonstrated the highest flavonoid content as well as the highest free radical scavenging activity of *A. meansii.* The solubility of copper chalcogenides and plant extract was tested in four different solvents and the solvent that demonstrated highest solubility was used for the coordination of the plant extract and copper chalcogenides. The plant extract coordinated nanoparticles were tested for their antibacterial and antifungal activity. Their results were compared to those of the active ingredient in their respective solvents from the medicinal plants as well as those of copper chalcogenides nanoparticles without plant extracts using diffusion disk and MICs methods. The synthesized nanoparticles showed better performance than plant extracts with copper oxide performing the best, followed by copper selenide and lastly by copper sulfide. The performance of plants extracts highly dependent on the solvent of extract with acetone showing the best performance for both *C. molle* and *A. Mearnsii* followed by ethanol. The addition of active ingredients from *C. molle* and *A. mearnsii* to the synthesized nanoparticles did not enhance the performance of these nanoparticles.

DEDICATION

I dedicate this work to my parents, my lovely son Likho Mbewana-Ntshanka and my loving husband Siphamandla Ntshanka.

ACKNOWLEDGEMENTS

- First and foremost, I would like to give all the glory to the most high God, the source of my strength, the author and the finisher of my life, the pillar that holds my life.
- Prof M.J Moloto. You have been more than just a supervisor, at times you played a role of being a father, you have always believed in me even when I did not believe in myself, if it was not because of you, I would not be where I am today. I am grateful to have met you.
- Dr P. K Mubiayi and Dr F Mthunzi. Thank you for your guidance, supervision and all your efforts to ensure that my project is successful.
- My gratitude goes to the department of biotechnology at VUT, and a special thanks to Samkeliso Takaidza. Thank you for the opportunity and the assistance that you have given me, you made my life to be much easier, you have a heart of gold.
- To the NCAP group, my wonderful colleagues and friends Z. Nate, D. Makanyane, K. Mokubung, T. Mofokeng, K. Mnqiwu, D. More, P. Ngoy, W. Bout, T. Ntuli, S. B. Sibokoza, N. Mabungela, L. Maremeni, A. Makamu, S. Nkabinde, M. Olifant, L. Dhlaba, M. Tsoku, T. T. Dammie thank you for your contribution to my work, I would not have acquired all the skills and the knowledge I have without you.
- VUT, especially the department of chemistry thank you for giving me the opportunity to study in your institution.
- To the national research foundation (NRF) and VUT research directorate, thank you for granting me funds to further my studies.
- To my husband, my better half. Thank you for love and support you have given me. You have compromised a lot so that I can be able finish my studies. At time you had to be a father and a mother to our son and you did that without complaining. Thank you Sikhosi.
- To my son, the love of my life, the apple of my eye, the source of my strength, my sunshine. For you being alive just makes me content. The hope of giving you a better future is what drives me to study day and night.
- To my loving mother Nothembikhaya Mbewana, the strongest woman I have ever met, thank you for everything you have done for me, I am a graduate, a mother, a wife, a sister and an aunt today all because of who you are. Thank you Mom.

- To my loving father, Siyambonga Mbewana. Thank you for always believing in me, your positive attitude towards life is what enables me to wake up every morning and see life as a precious gift.
- To my siblings, Nombulelo, Sindiswa, Bonginkosi, Bathandwa, Bathabile and Lisolethu. Thank you for all the support that you have given me. Your passion and dedication towards education have always inspired me to study further.
- A special thanks to everyone else who has contributed to my work, your inputs are highly appreciated.

Table of Contents

LIST OF FIGURES

LIST OF TABLES

LIST OF ABBREVIATIONS

NPs: nanoparticles

NCs: nanocrystals

FWHM: full width at half maximum

OLA: Oleylamine

TOP: tri-n-octylphosphine

XRD: X-ray diffractometry

TEM: transmission electron microscopy

UV-Vis: Ultraviolet Visible

PL: Photoluminescence

FTIR: Fourier transform infrared

MICs: minimum inhibitory concentrations

C.m: *Combretum Molle*

A.m: *Acacia Mearnsii*

Eg: band gap energy

VB: valance band

CB: conduction band

SPR: Surface Plasmonic Resonance

LSPR: Localized surface plasmon resonances

ASPL: Anti stokes shift photoluminescence

NIR: near-infrared

MHB: Muller-Hinton broth

MHA: Muller-Hinton Agar

MEB: Malt-Extraction broth

DNA: Deoxyribonucleic acid

MEA: Malt-Extraction Agar

mRNA: messenger ribonucleic acids

DPPH: 1.1-diphenyl-2-picryl hydrazyl

MICs: minimum inhibitory concentrations

nm: nanometre

a.u: arbitrary units

SCV: scavenging activity

QU: quercetin

GA: gallic acid

AS: ascorbic acid

RA: relative activity

aB: Bohr radius

λmax: wavelength maximum

CHAPTER 1

General Background and Literature Review of nanoparticles and medicinal plant extracts

1.1. General background of colloidal nanoparticles and plant extracts

1.1.1. Colloidal semiconductor nanoparticles

Colloidal nanocrystal are nanometer-sized, inorganic particles that are stabilized by a layer of surfactants that are attached to their surface. Each of these colloidal nanocrystals are made up of hundreds and thousands of atoms and can be easily controlled by adjusting their physical properties such as the size and shape as well as its crystal composition. Their properties can be controlled by varying synthetic parameters such as temperature, time of the reaction, concentration of precursors and of the capping molecule, binding energy of the surfactant and the surface energy of crystal facets. Their size range is usually from 2 to about 100 nm which allows their band gap to be tuned hence the Plasmon Resonance shifts (Alivisatos *et a*l. 1996; Alivisatos *et al*. 1998; Ustis *et al.* 2006; Link *et al*. 1999; Sherry *et al*. 2005). When the material size is physically changed to be in the similar magnitude as the Bohr radii, quantum confinement effects are observed (Rogach *et al.* 2008) and the new properties emerging at the scale length that can be controlled by tuning the density of their electronic states. When the resulted properties are due to the systematic transformation in the density of electronic energy levels as a function of size of the interior and are known as quantum size effects (Burda *et al*. 2005; Murray *et al*. 2001; Brus *et al*. 1985). Different types of morphologies can be attained by a delicate adjustment of the equilibrium between kinetics growth and thermodynamic growth regimes (Burda *et al*. 2005; Jun *et al*. 2005). Various types of morphologies include symmetry-controlled spheres, cubes, discs (Ahmadi *et al.* 1996; Yu *et al*. 1997; Li *et al*. 2011; Cho *et al*. 2005; Chen *et al*. 2002; Shen *et al*. 2012) and anisotropic geometries like rods, disc, arrows (Manna *et al*. 2000), nanowires (Sun *et al*. 2008; Bonfield *et al*. 2000 and tetrapods (Cozzoli *et al*. 2005; Teng *et al*. 2005; Cozzoli *et al*. 2006; Hu

et al. 2005; Milliron *et al*. 2004). Therefore, the growth process of nanocrystals requires a delicate balance between kinetic and thermodymic parameters.

Colloidal nanocrystal materials have gained tremendous attention from researches due to their great importance in materials physical and chemical properties (Brus *et al*. 1991; Wang *et al*. 1991). Due to their novel electronic, magnetic, optical, chemical and mechanical properties, they are currently exploited as active components in a wide range of technological applications such as composite materials (Morris *et al*. 1999; Caruso *et al*. 2000), chemical sensing, biomedicine (Bawendi *et al*. 1990; Ray *et al*. 2010; Lin *et al*. 2011), optoelectronics (*Jin et al*. 2012; Moloto *et al*. 2008), and nanoelectronics (Lui *et al*. 2010; Santra *et al*. 2005; Muller *et al*. 2005). They are promising candidates as building blocks for new electronic and optical nanodevices such as quantum computers, light emitting diodes (Jin *et al*. 2012; Hu *et al*. 2009; Zhao *et al*. 2010), solar cells or lasers, photovoltaic devices (Anikeeva *et al*. 2007; Ray *et al*. 2007), biological labelling and diagnostics (Lin *et al*. 2011; Jin *et al*. 2012). The size- and shape-dependant physical properties as well as ease of fabrication makes nanocrystals to be promising building blocks for materials with designed functionalities (Alivisatos *et al*. 1997; El-Sayed *et al*. 2004).

1.1.2. Properties of semiconductor nanoparticles

(a) Optical properties of semiconductor nanoparticles

The optical properties of nanocrystal semiconductors are based on size related fundamental unlike nanocrystals which are associated with three-dimensional quantum confinement of their charge carriers (Hu *et al*. 2001). Semiconductor crystalline are characterised by their band gap energy (*Eg*) that falls within the range between $0 < Eg < 4\ eV$ and can be thought of as the minimum energy required to excite an electron from the valence band to the conduction band as schematically shown in Figure 1.1 (Gupta et al. 2009).

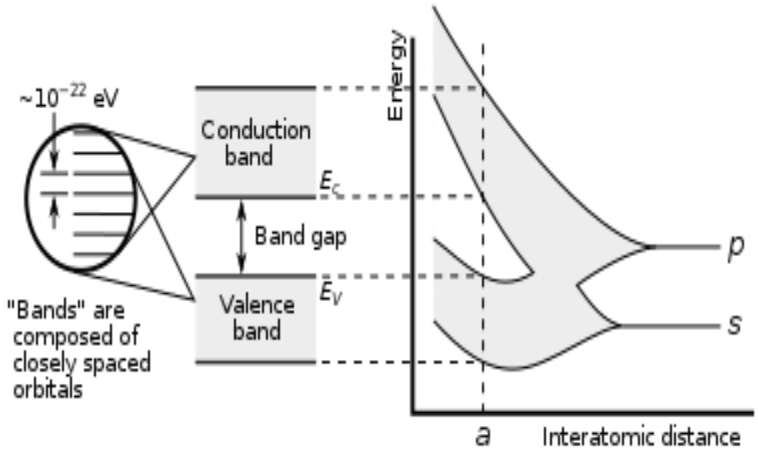

Figure 1.1: Electronic band structure (Holgate *et al*. 2009)

The dependence of the energy of electron transitions between quantized levels of the valance and conduction bands on the particle size is used to estimate the particle size. Such transition is often called excitonic (Chestnoy *et al*. 1986), because an electron-hole pair generated by light absorption is similar to the Wannier-Mott exciton in a bulk crystal. The photons of higher energy (4.1eV) excite electrons from valence band (VB) to conduction band (CB) by vertical transitions and within 10-11sec the electrons comes to the bottom of CB dissipating the excess energy as lattice vibrations. Then the electrons drop to the VB and recombine with hole emitting the photons of lower energy as the Franck Condon principle. The absorption peak corresponds to vertical upward transition from the top of VB whereas emission peak corresponds to vertical downward transition from lowest level of CB (Gupta et al. 2009).

The shape of nanocrystals affects the electronic structure as well as the electron distribution within the nanocrystals. By confining the excitation in different dimensions and band gap they can be tuned to a precise energy depending on the dimensionality and degree of confinement. This enables them to be used as active materials in various applications and fields (Hu *et al*. 2001). Nanocrystals with dimensions smaller than the Bohr excitation diameter –aB demonstrate quantum size effects of size-dependant absorption and fluorescence spectra with discrete electronic transitions and results in the shifted band gap in emission spectra. Bohr excitation radius is defined as a dimension describing the spatial extension of excitons (i.e., electron-hole pairs) in semiconductors and can be expressed as:

$$\alpha_b^* = \varepsilon_r (m/\mu)\alpha_b \quad (1)$$

where, ε_r is the dielectric constant (relative permittivity), m is the mass, μ is reduced mass, and ab represents the Bohr radius (~0.053 nm) (Alivisatos et al. 1996).

When the radius of the particles decreases, the band gap increases and emit energy at a higher wavelength (blue region) but when the radius of the particle is increased, the energy gap will be less and therefore emit light in red region. The energy gap is therefore, inversely proportional to the radius of the particle.

$$E \propto \frac{1}{r} \quad (2)$$

Elongation of short rods induces extra length dependent properties such as dipole moment, conductivity and linearly polarized emission along the c-axis whereas the diameter dependant properties such as band gap can be largely preserved (Li *et al*. 2003). Since up to half the atoms making up a nanocrystal may be on its surface as the crystal becomes smaller, the optical properties of nanocrystals can be impacted by the surface properties as well (Underwood *et al*. 2001) which probably arises from the modulation of surface energy states formed by the ‘’dangling orbital’’.

(b) Plasmonic properties

Surface Plasmonic Resonance (SPR) is an optical technique used to study molecular interactions (Schuck *et al*. 1997; Ramakrishnan *et al*. 2006). The interaction between an electromagnetic wave and the conduction electrons in the nanocrystal relies on the shape and size of the metal nanoparticles and on the nature and composition of the dispersing medium. The size of noble metals is reduced in to tens of nanometres due to the collective oscillated ion of the electron on the conductions band resulting to a new very strong absorption. The oscillation occurs at the frequency that can be span from the visible IR and the strong oscillation can be achieved if the oscillation is in resonance with the incident light. At this resonant frequency, the incident light is absorbed by the nanostructure some of these photons will be released with the same frequency in all directions and this process is known as scattering. Some of the photon will simultaneously be converted to phonons or vibrations of the lattice and this is referred to as absorption process (Wolf *et al*. 2015).

Several degenerately doped copper chalcogenide nanoparticles have been discovered to have a Near Infrared (NIR) absorption band which originates from plasmonic properties. These includes $Cu_{2-x}Se$ (Dorfs *et al*. 2011; Balitskii *et al*. 2010; Wang *et al*. 2014), $Cu_{2-x}S$ (Luther *et al*. 2011; Zhao *et al*. 2009: Xie *et al*. 2013; Kriegel *et al*. 2013), $Cu_{2-x}Te$ (Kriegel *et al*. 2013; Li *et al*. 2013), and their alloys (Dilena *et al*. 2012; Saldanha *et al*. 2014; Lui *et al*. 2013). A number of reports also appeared on localized surface plasmon resonance (LSPRs) (Kajikawa *et al*. 2006), which occurs in metallic nanostructures such as rough surfaces and nanoparticles. Mnqiwu *et al*. 2017 reported plasmonic phenomena of copper sulphide which resulted from the collective oscillation of electrons in the conduction band when irradiated with an incident light of appropriate wavelength. The broad range of applications of the LSPRs has been shown extensively (Sau *et al*. 2010; Jain *et al*. 2008; Halas *et al*. 2011; Sepulveda *et al*. 2009). However, the tuning of LSPRs metals into the NIR region can only be possibly done with very large particles such as nanorods, core–shell structures, *etc*. (Sau *et al*. 2010; Oldenburg *et al*. 1998; Murphy *et al*. 2005) or *via* shape control (Link *et al*. 1999; Ziegler *et al*. 2011).

1.1.3. Synthesis of nanocrystals

(a) Basic Synthesis of nanocrystals

Properties of nanocrystals strongly depend upon the size, the shape, the composition, the structure and the surface functionality of the nanocrystal. The mentioned characteristics also depend on the synthesis approach of the nanocrystals. Therefore, a controlled synthesis approach is required to tailor and optimize properties of the nanocrystals to establish their dependency on the physical and chemical parameters that define them. It is of great interest to separate nucleation event from the growth event as this is a critical parameter to obtain nanocrystals with a narrow size distribution (Cao *et al*. 2010).

(i) Nucleation event in colloidal synthesis

During the synthesis of nanocrystals, nucleation occurs only when the superstation reaches a critical value above the solubility which corresponds to the energy barrier defined by the equation:

$$\Delta G^* = 16\pi\gamma/3(\Delta G_v)^2 \quad (3)$$

where ΔG^* is the critical Gibbs free energy i.e. the energy barrier that a nucleation process must overcome to produce a seed (nuclei), γ is the surface energy of the new phase and ΔG_v is the change of Gibbs free energy per unit volume of the solid phase (Kwon *et al.* 2011). This means that nucleation occurs when the concentration of the medium reaches the minimum saturation required to generate the critical free energy. In a colloidal synthesis, nucleation should occur on a short time scale and can be possibly achieved by the hot-injection technique whereby the nucleation takes place rapidly right after injection of the precursor molecule into a hot solvent. When such a technique is used, the nucleation process continues until the temperature and the monomer concentration drop below a critical threshold and then only the growth event occurs at a lower temperature. The morphology of the final nanocrystal material is determined not only by the growth process but also by several parameters such as crystalline phase of the material formed, the nucleation rate (Cao *et al.* 2010; De Mello *et al.* 2005; Peng *et al.* 2001; Shevchenko *et al.* 2003; Peng *et al.* 1995), and monomer concentration during the nucleation process. The rate of nucleation J can be expressed by the equation;

$$J=A \exp (-\Delta G^*/kT) \quad (4)$$

where, J is the rate of nucleation, ΔG^* is the critical Gibbs free energy, k is the Boltzman constant and T is the temperature. Considering the basic Gibbs-Thomson relationship for non-electrolyte is given by

$$\ln S=2\gamma v/kT \quad (5)$$

(S is the ratio of solution concentration to that of equilibrium saturation concentration at a given temperature; γ is the interfacial tension, v is the molar volume and r is the nucleus' radius)

Finally, we can deduce that

$$J=A \exp [-16\Pi v^2\gamma^3/3k^3 (\ln S)^2] \quad (6)$$

This indicates that the rate of nucleation is determined by the three main variables which are namely temperature (T) and degree of supersaturation (S) and interfacial tension (γ). Amongst the above mentioned, nucleation rate is more sensitive to the change of temperature compared to the growth rate because of the highest activation energy needed for the nucleation process than that of

the particle growth (Sugimoto *et al*. 2001). This makes the balance between nucleation and growth rate to be tuned via changing of the temperature.

(ii) Growth event in colloidal synthesis

The growth processes of the nuclei involve multiple-steps. The major steps include generation of growth species, diffusion of the growth species form bulk to growth surface, adsorption of the growth species on to the growth surface, and surface growth through irreversible incorporation of growth species onto the solid surface. These steps can be grouped into two processes which are namely; growth of consuming molecular precursors from surrounding solution known as ''focusing of size distribution'' and Ostwald ripening or coarsening when large particles grow at the expense of dissolving smaller ones that is also known as defocusing of the size distribution. For different applications, highly monodispersed nanocrystals with narrow size distribution are always favoured. When the concentration of growth species reduces below the minimum concentration for the nucleation, nucleation stops and growth continues. In this way, narrow size distribution is obtained. When nanocrystals are very small, it becomes unstable due to the large fraction of active surface atoms and they need to keep growing. Growth is accompanied by the decrease of surface-to-volume ratio unit the critical size is achieved by the crystal becoming relatively stable. At critical size, the nanocrystals neither grow nor shrink (dG/dr=0). The critical size and the growth rate are determined by this equation;

$$r_c = 2\gamma v/kT\ln S \qquad (7)$$

where, S represents the monomer concentration. Ostwald-ripening broadens the size distribution and this means that the smaller nanocrystals with higher chemical potential evolve monomer and dissolve whereas larger nanocrystals consume monomer and grow. This means high concentration of monomers is required for the smaller nanocrystals to grow faster than the bigger ones and the size distribution can get narrow (Peng *et al*. 1995; Sugimoto *et al*. 2001).

(iii) Hot-injection method

Hot injection method produces nanoparticles of high quality and mono dispersed by controlling the precipitate of colloidal solution. In colloidal hot-injection method, the precursor is quickly

injected to a hot coordinating solvent which leads to thermal decomposition of the precursor reagents and supersaturation of the "formed" monomer to generate nucleation. This nucleation is arrested by the decrease in temperature following the injection. Growth then proceeds by the addition of monomer from solution to the nanoparticle nuclei. Monomer concentrations are below the critical concentration for nucleation; thus, these species only add to existing particles, rather than forming new nuclei. This is then followed by the addition of the solvent to a cooled solution, thereby increasing the barriers to flocculation. Solid particles are separated by centrifugation.

(b) Parameters that influence size and shape control of nanocrystals

The quality of metal chalcogenide nanocrystals influences their properties as well as their final applications. Attempts to control the growth are through variation of the reaction parameters that affect the synthesis. Time taken for the reaction to complete, the temperature of the reaction, the concentration of the precursors, the type of the capping molecule and its concentration, and the solvent used are critical parameters that influence the size and the morphology of the nanoparticles. Cheon and co-workers (2006) demonstrated the influence of these parameters on the shapes of the nanoparticles as well as the size. Cheon *et al*. (2006) showed that the use of high precursor concentrations increased the time taken for the growth of the particles which resulted in morphology variation. They also demonstrated that different temperatures favoured different crystalline phases which resulted in growth at different crystalline planes hence affected the morphology. The shape of the nanocrystals can also be controlled by using surfactants that bind differently to the crystallographic faces (Robel *et al*. 2006).

(i) The effect of capping agents

The capping molecule used in the synthesis of nanoparticles is one of the most important parameters that strongly affect the size and the morphology of particles in a colloidal method. The agent molecules are adsorbed on the surface of the growing crystal when high temperatures such as 200 - 400 °C are used. The choice of surfactants varies depending on the method used. A strong coordinating molecule is usually not suitable, as it would not allow the crystal to grow, while a weak coordinating molecule would yield large particles, or aggregates. At low temperatures, the

surfactants are strongly bound to the surface of the nanocrystals and provide appreciable solubility in organic solvents (Robel *et al*. 2006; Bi *et al*. 2013; Balis *et al*. 2013; Swapnil *et al*. 2006).

(ii) The effect of time

In colloidal method the investigation of reaction time is the main feature for particle growth and size distribution in order to get nanocrystals with desired properties (Kalenga *et al*. 2012; Hung *et al*. 2008). The availability of a large number of nuclei at a given time induces a decrease in the nanoparticle size, hence many nuclei are preferred. Shorter nucleation time is better for control of size distribution (Dung *et al*. 2011). Furthermore, the particles with smaller sizes dissolve and recrystallize because of their higher surface energy. This suggests that time has a profound effect on the nanocrystals size and shapes with longer time reaction favouring large particle size (Ramasamy *et al*. 2010). The size and the shape of particles are determined by Ostwald ripening process (Murray *et al*. 1993). The key point to accomplish the desired nanocrystals is to balance the nucleation and growth processes kinetically because the size distribution of initial nuclei may increase or decrease depending on the kinetics of the subsequent growth process. This may also prevent the formation of bulk crystals (Li *et al*. 2013).

(iii) The effect of temperature

The size distribution of nanocrystals is highly affected by the kinetics of nucleation, growth process, as well as the thermodynamic regime (Cheng *et al*. 2010). The temperature is therefore one of the factors affecting the synthesis of nanoparticles. Crystallographic phases of the nuclei are the major critical factor responsible for the shape determination of the nanocrystals during nucleation process. The nuclei formed may contain different types of crystallographic phases, which are dependant on the temperature of the synthesis (Lee *et al*. 2003). When the prefered crystallographic phase have been determined during the initial nucleation stage, the subsequent growth stage and the final shape of the nanocrystalls are determined through a delicate balance between the kinetic growth and thermodynamic growth regimes. When excess thermal energy is employed, larger sizes of the nanocrystals are favoured and aggregation with chain-like structures is observed (Moloto *et al*. 2008). There are several factors influencing the anisotropic growth of nanocrystals. These include the crystalline phase of the nucleating seeds, surface energy, colloidal

stability, aging process, control of the growth regime and supersaturation (Lee *et al*. 2003). Supersaturation is generally highly dependant on solution temperature, thereby a high supersaturated solution possesses high Gibbs free energy. Lowering of the Gibbs energy can be achieved through a driving force of nucleation and growth of particles. Such relation can be expressed by the following equation:

$$\Delta G_v = - [kT/\Omega] \ln (C/Co) = - [kT/\Omega] \ln (1+\dot{O}) \quad (8)$$

where C is the concentration of the solute, Co is the equilibrium concentration or solubility, K is the Boltzman constant, T is the temperature, Ω is the supersaturation that is defined as (C-Co)/Co according to Cao *et al*. (2004) report. This mean that no nucleation will take place when there is no supersaturation ($\dot{O} = 0$), $\Delta G_v = 0$. According to this equation, Gibbs free energy change per unit volume (ΔG_v) can be significantly increased by increasing the supersaturation in a system. At low temperatures, a higher supersaturation leads to a large reduction in gibbs free energy and small sizes of particles are produced. At higher temperatures, increased solubity is observed which leads to less supersaturaion of the solution which results in large particles being produced (Ravi *et al.* 2009).

Peng *et al*. (2000) investigated the mechanisms of shape evolution of CdSe nanocrystals and observed that the solubility of crystals increases as the size of the nanocrystals decreases. This was expresssed by the following equation:

$$\Delta G = \Delta G_s + \Delta G_v = 4\pi r^2 y + 4\pi r^3 \Delta G_v /3 \quad (9)$$

where ΔG_v is the Gibbs free energy change per unit volume, and r is the radius of the spherical nucleus.This equation explains the fact that particles that are smaller than r_c will dissolve while the particle grows bigger to reduce the Gibbs free energy. This indicates that the nucleation rate is determined by three variables which are: temperature, degree of supersaturation and interfacial tension. Amongst the three, nucleation rate higly depends on temperature because of the high activation energy needed for nucleation than for growth process (Sugimoto *et al*. 2001).

Li *et al*. (2013) investigated morphology evolution of disks over a range of temperature from 180 °C to 210 °C. The authors proved that at elevated temperatures nanoparticles have increased sizes, well ordered into multilayers which could be due to enhanced growth rate but with no morphological evolution of the nanodiscs. Kalenga *et al*. (2012) also investigated the effect of

temperature on the synthesis of copper selenide nanoparticles and found out that when the temperature is increased up to 300 °C, a slow growth of the existing nuclei were observed with no further nucleation and this allows for nanocrystals to anneal and form nearly defect-free crystal lattices, which are identical to the bulk lattice.

(iv) The effect of precursor concentration

The concentration of the precursors and capping moecule have an impact on the properties of the synthesized nanoparticles. A solution containing a solute that exceeds solubility or supersaturation possesses a high Gibbs free energy and this energy can be reduced by both nucleation and growth force. Therefore, the change of Gibbs free energy per unit volume of the solid phase is highly dependent on the concentration of the solute which is expressed by equation (8) above.

High initial concentration or supersaturation and low critical energy barrier favour the production of large number of nuclei. This can be expessed by the following equation:

$R_N = nPT$ and (10)

$P=\exp(-\Delta G^*/KT)$ therefore; (11)

$R_N = \{(CoKT/3\pi\lambda^3\eta)\} \exp(-\Delta G^*/KT)$ (12)

where R_N is the rate of nucleation per unit volume and per unit time , P is the probability, ΔG^* is the thermodynamic flacuation of critical free energy, λ is the diameter of growth speies and η is the viscocity of the solution. For a given concentration of solute, a large number of nuclei means smaller sized nuclei (Ravi *et al*. 2009).

Moloto *et al*. 2012 investigated the influence of the precursor concentration, temperature, and capping enviroment as factors that affects the size and morphlogy of the nanoparticles and discovered that when the concentration of a precursor was increased, the size of particles also increased and the morphology evolved from spherical to rod-shaped nanoprticles. Cheon *et al.* (2006) argued that using high concentratations of precursor prolongs the time taken for the particles to grow and thus results in morphology variation. Sibokoza *et al*. (2017) investigated the effect of concentration on the sythesis of cobalt sulfide and his findings were inconsistent with the previous authors who reported an increased particle size with an increase of precursor

concentration. Sibiya *et al*. (2014) investigated the influence of pH and precursor concentration on the size and shape of nanoparticles and reported a similar trend when the precursor concentration was increased.

1.1.4. Copper chalcogenide nanoparticles

Copper chalcogenide nanoparticles are being sought in both fundamental science and technological applications (Dorfs *et al*. 2011). Copper-based semiconductors have recently gained recognition as biocompatible alternatives due to bacterial infections which has become a concern globally mainly due to the development of antibiotic resistance. In the past years, there has been an increased resistance in gram-negative bacteria (Pallet and Hand. 2010). The World Health Organization (WHO) estimated that approximately 80% of the population of the developing country rely on traditional medicines mostly plants or derived products for disease treatment (WHO, 1993) (Noumedem *et al*. 2013).

Numerous therapeutic approaches are being used to control different diseases. A current approach is the development of new compounds such as nanoparticles that have been synthesized with and without plants extracts. These nanoparticles will need to be in the right size range and adequate cell biocompatibility (Zhang *et al*. 2012). The reason for this is because the use of nanoparticles for biological related applications is strongly affected by their sizes. These nano-sized semiconductors have been synthesized by a variety of methods for tuning the properties for specific applications. The methods that have been used for their synthesis includes precipitation methods (Suleiman *et al*. 2013), sol gel methods (Aparna *et al*. 2012), Solid-Liquid discharge (Yao *et al*. 2005), electrochemical radiolysis alcohothermal (Son et al., 2009), alcohothermal (Lim *et al*. 2012), direct thermal (Darezershki *et al*. 2011), sonochemical (Narongdet *et al*. 2011), microwave radiation (Wang *et al*. 2002), colloidal-thermal methods (Honary *et al*. 2012) etc. Some of these methods are complicated and have drawbacks such as the drastic conditions, difficult control of particle growth, higher energy consumption etc. (Honary *et al*. 2012). The colloidal hot injection method which was employed in this work has been reported to produce nanocrystals with a narrow size distribution. It enables one to control the conductive properties of the material by controlling the size of the crystals. It has an advantage of separating nucleation and growth stages during the synthesis which leads to high mono dispersed material without having to do post synthesis size-

selective technique (Mahajan *et al*. 2013). This method requires high but not extreme temperatures. Under those conditions particles with good crystalline structure are obtained and can relatively be isolated after a short time of synthesis.

1.1.5. Applications

(a) General applications of copper chalcogenide nanoparticles

Copper chalcogenide nanoparticles can be useful in daily life applications such as nano-electronic devices, nano-optical devices, photovoltaics, medicine (Lui *et al*. 2008), catalyst (Jianliang *et al*. 2011; Sang *et al*. 2002), antioxidant (Sun *et al*. 2008), gas sensors (Grozdanov *et al*. 1994; Yang *et al*. 2007), super conductors, water purification, solar cells (Greenwood *et al*. 1990; Jess *et al*. 2009), field emission (Bohr *et al*. 2009; Lane *et al*. 2010), optoelectronics (Swankar *et al*. 2010), antimicrobial agent (Stoimenov *et al*. 2002; Honary *et al*. 2012), and their efficiency as nanofluids in heat transfer application (Chen *et al*. 2018).

(b) Biological and medical applications of nanoparticles

The biological and medical research communities have exploited the unique properties of nanomaterials for various applications (Syed et al. 2012). Semiconductor nanoparticles have been proven to have a wide range of potential biomedical applications, especially when combined with antigen specific coatings or functional groups on their surfaces (Tachan *et al*. 2010). The extremely high surface areas and unusual crystal morphologies endow copper oxide nanoparticles with antimicrobial activity. The dose dependently inhibits *Eschericial coli* strains, but not *Salmonella tryphimurium* (Wiley *et al*. 2005). This finding provides a way to develop novel and specific antimicrobial agent (Stoimenov *et al*. 2002).

Numerous therapeutic approaches are being used to control different diseases. A current approach is the development of new compounds such as nanoparticles possessing biocompatible properties. These nanoparticles need to be in the right size range and adequate cell biocompatible properties (Zhang *et al*. 2012). Their optimal sizes should be between 10 and 50 nm for some diseases treatment and therapies particularly for *in vivo* studies through photoexcitation, optical diagnostic imaging and photo thermal therapy. Larger nanoparticles are removed by the reticuloendothelial system, primarily by the liver and spleen, and smaller particles by the renal system (Hu *et al*. 2012).

Semiconductor nanoparticles have also been used in DNA or mRNA tracking. Several groups have done their studies on quantum dot, which are covered by a surfactant that includes carboxylic group, conjugated oligonucleotide sequences that bound to DNA or mRNA (Gao *et al*. 2004; Santra *et al*. 2001). Semiconductor nanoparticles are also used as detectors for pathogens, virulence and toxins (Dung *et al*. 2011; Yang *et al*. 2006). Magnetic nanoparticles, bound to a suitable antibody, are used to label specific molecules, structures or microorganisms. Gold nanoparticles tagged with short segments of DNA can be used for detection of genetic sequence in a sample (Jain *et al*. 2003). Nanotechnology could be used in medical field for delivering of drugs to specific cells using nanoparticles. The overall drug consumption and side-effects can be lowered significantly by depositing the active agent in the morbid region only and in no higher dose than needed. This highly selective approach reduces costs and human suffering (Quan *et al.* 2011; Sala *et al*. 2002).

1.1.6. Medicinal plants (Combretum molle and Acacia mearnsii)

From previous studies, many African plants have demonstrated good antibacterial activities against both gram-negative and gram-positive Multiple Drug Resistance (MDR) bacteria (Noumedem *et al.* 2013). Species of the genus *Combretum molle* and *Acacia mearnsii* are some of these plants that are rich in terpenoids. Terpenoids are known to have a broad spectrum of biological activities including analgesic, anti-inflammatory, antibacterial, anticancer antiprotozoal and antioxidant (Sala *et al*. 2002). With regards to antioxidant systems, they either prevent active species from being formed or remove them before they cause damage to vital components of the cell. The reaction of oxygen species are produced by human body's use of oxygen, such as in respiration and some cell-mediated immune functions which include hydrogen peroxide (H_2O_2), hypo chloric acid (HOCl), free radicals such as the hydroxyl radicals (•OH) and the superoxide anion (O_2^-) (Praveen and Ashish., 2012). Plant extracts are widely used in food (cereals, vegetables, and fruits) to provide healthy alternatives and replacement of medication (Shi *et al*. 2011), as well as in pharmaceutical, and cosmetics industry. Because these medicinal plant extracts contain lot of flavonoids, alkaloids, starch, proteins, sugar, phenols and antioxidant molecules which all bearing the important compounds such as hydroxyl and carbonyl. Both these functional groups allow plant extracts to act as bio reducing agent and the molecules of these plants further acts as a

stabilizing agent on the synthesized nanoparticles. When these functional groups are attached to the synthesized nanoparticles, the reactivity of the nanoparticles might be enhanced, and their microbial activity might be increased.

Different types of extraction techniques have been widely investigated and used to obtain valuable natural compounds from plants for commercialization. These techniques include conventional and non-conventional techniques. In this study, a conventional technique was employed to extract phenols, flavonoids and antioxidant which were used for the synthesis of copper chalcogenide nanoparticles as well as for bacterial activity.

(a) Phenols

Phenolic compounds can be classified into soluble compounds such as phenolic acids, phenylpropanoids, flavonoids and quinones and non-soluble compounds such as condensed tannins, lignins, and cell-wall bound hydroxycinammic acids (Harbone *et al*. 2000). Phenolics are of interest due to wide range of ecological effects from organisms to ecosystem level (Tosun *et al.* 2009). Their most significant characteristic is their involvement in redox reactions and neutralization of active oxygen species (Karpova *et al*. 2009). Their scavenging ability on free radicals due to their hydroxyl group highlights their significance. They contribute directly to their antioxidant action. The phenolic oxidants also provide for their anti-inflammatory, antimicrobic, spasmolytic and neuroprotective actions (McDonald *et al*. 2001). Phenols are categorized as polyphenols and phenolic acid. Polyphenols can be further classified as Hydroxycynnamic acids, lignins, stilbenes, suberins, cynnamic aldehydes, coumarins and flavonoids as shown in figure 1.2 below and phenolic acid are classified as benzoic acids and cinnamic acids.

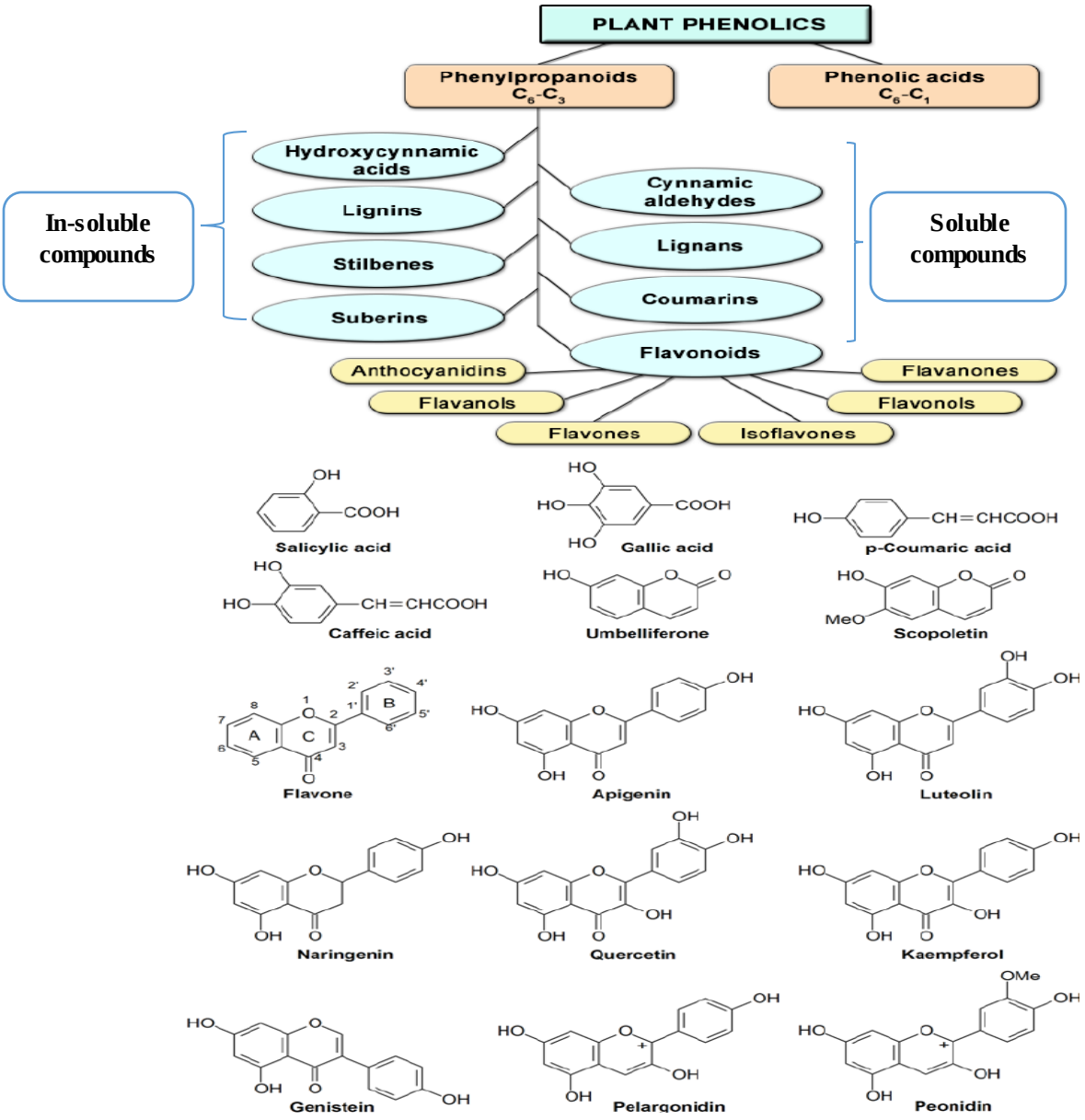

Figure 1.2: Chemical structures and classification of phenolic compounds (Katerova *et al*. 2013)

(b) Flavonoids

Flavonoids are a group of polyphenolic secondary metabolites compounds which are presented broadly in plants with bioactive effects. Their beneficiary effects on health include free radical scavenging, inhibition of hydrolytic and oxidative enzymes, anti-viral, antibiotic, and anti-inflammatory action (Krych *et al*. 2013; Ragad *et al*. 2014). They can be extracted very easy with polar solvents such as methanol. The basic structures of flavonoids consist of C_6-C_3-C_6 rings with

different substitution patterns to produce a series of sub-class compounds. The correlations between chemical structures and bioactivities that have been studied before (Tian *et al*. 2014; Zhang *et al*. 2015; Aokie *et al*. 2000). Based on their chemical structure, they may be categorized into six classes which are: anthocyanidins, flavan-3-ols, flavanones, flavones, flavanols, and isoflavones. All these types of compounds are composed of three aromatic rings, having different substitutions of methylation and hydroxylation (Wu *et al*. 2013).

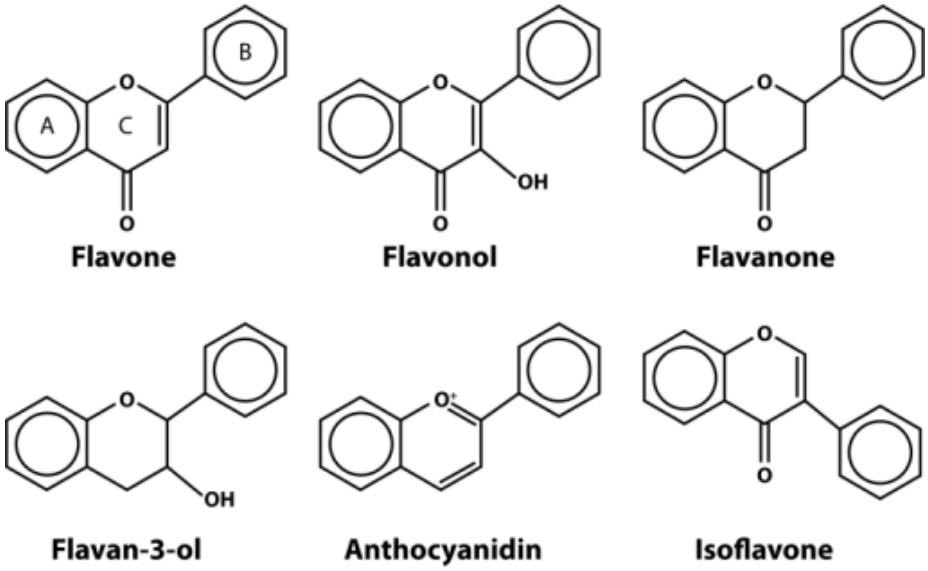

Figure 1.3: Chemical structures and classification of flavonoids (Tian *et al*. 2017)

Flavons and flavonols contain the largest number of compounds, representing the narrow-sense flavonoids namely 2-benzo-*y* pyrone category. Flavanones and flavanonols possess saturated C_2=C_3 bonds and often coexist with relevant flavons and flavanols in plants (bioactive flavonoids in medicinal plants). The antioxidant activity of flavonoids depends on the structure and substitution pattern of hydroxyl group (Chang *et al*. 2002). The position and number of hydroxylation correlate reasonably to anti-oxidation of flavonoids. More hydroxyl group results in lower hydrophobicity, which is obstructive for flavonoids partition into biological membranes (Pourmorad *et al*. 2006; Rohman *et al*. 2010).

(c) Antioxidants

Antioxidants are substances that are already found in plants and they possess free radical chain reaction breaking properties (Zheng *et al*. 2001). Antioxidant are classified as enzymatic and non-enzymatic. Non-enzymatics are further classified as phenolic acids and flavonoids as shown in figure 1.3 below. Naturally occurring antioxidants (obtained from plants) such as ascorbic acid, carotenoids, and phenolic compounds are of great benefit and more effective than the synthetic (Rohman et al. 2010; Zheng and Wang 2001). Their use does not induce side effects, while synthetic antioxidants were found to have genotoxic effects (Ramasamy *et al*. 2010; Murray *et al.* 1993). Natural antioxidants are known to inhibit lipid peroxidation, to scavenge free radicals and active oxygen species (Li *et al*. 2013). Free radicals and active oxygen species cause oxidation which contributes to more than one hundred disorders in humans including cell damage, arthritis, atherosclerosis, ischemia, reperfusion injury of many tissues, central nervous system injury, gastritis, cancer and AIDS (Cheng *et al*. 2010; Lee *et al*. 2003). Therefore, antioxidants reduce the number of free radicals that form in the body, lower their energy levels and stop the oxidation (Heyding *et al*. 1976; Shafizade *et al*. 1978). An easy and rapid method to screen antioxidants in plants is free radical scavenging assay using 1, 1-diphenyl-2-picryl hydrazyl (DPPH) stable radical spectrophotometrically. In the presence of antioxidants, DPPH radical obtains one or more electron (s) and the absorbance decreases.

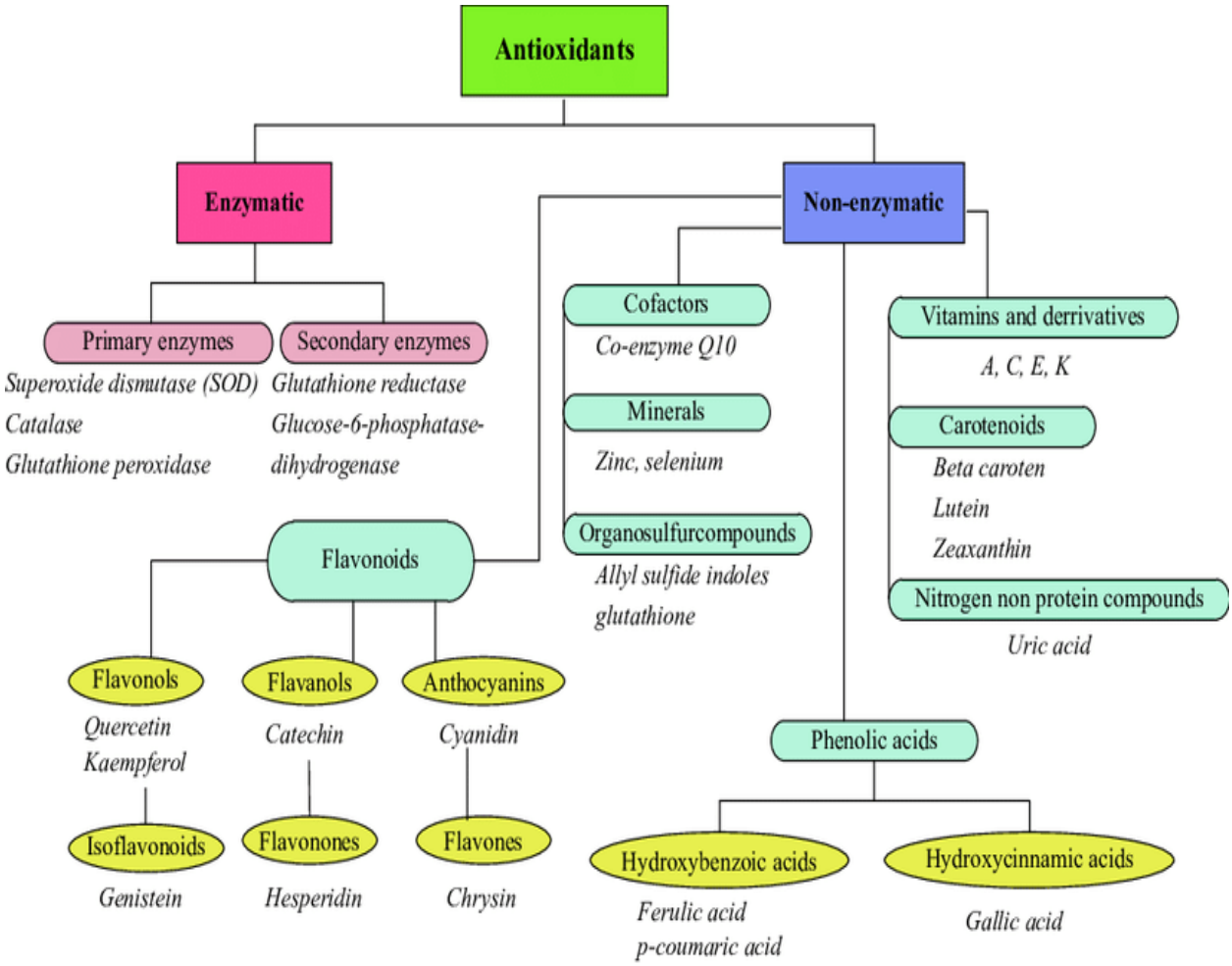

Figure 1.4: Chemical structures and classification of antioxidant (Iryna *et al.* 2018)

1.2. Literature review

1.2.1. Copper selenide nanoparticles

Few pioneering reports have described synthetic route for copper selenide nanostructures preparation, focusing on their structural characterisation and their photoluminescence properties (Dorf *et al.* 2011). It has been reported that copper selenide may be found in different stoichiometric forms such as CuSe, Cu_2Se, Cu_2Se_x, $CuSe_2$, α-Cu_2Se, $Cu_{2-x}Se$, Cu_3Se_2, Cu_5Se_4, and Cu_7Se_4 etc. Their thermal stability and band gaps vary with their stoichiometry or phases (Choi *et al.* 2010). Because of this stoichiometric variation, it is reported that copper selenide possesses a

direct band gap of 2.0-2.2 eV, as well as to an indirect band gap of 1.4 eV (Choi *et al*. 2010). Their several crystallographic forms (including monoclinic, cubic, tetragonal, hexagonal etc.) can be determined. Cubic berzelianite phase is mostly represented by Cu_2Se; the tetragonal umangite phase is found as Cu_3Se_2; hexagonal klockmannite phase is mostly found as CuSe whilst orthorhombic athabascaite phase is attributed to Cu_5Se_4 (Coughlan *et al*. 2017; Milman *et al*. 2002; Zhang *et al*. 2002). Copper selenide also exists in a non-stoichiometric composition which has two different crystalline phases namely; low temperature α phase (α-Cu_2Se monoclinic) and high temperature β phase (Cu_2Se cubic) (Schafer *et al*. 1996; Zhang *et al*. 2000; Wang *et al*. 1998). The stoichiometry-related properties of copper selenide include tuneable quantum efficiency, long term photo stability, narrow emission, and continuous absorption spectra. These are exploited in electrical, optical and biological applications such as solar cells (Kakshmikumar *et al*. 1994), sensors (Xu *et al*. 2009), super ionic conductors (Evy *et al*. 1997), thermoelectric converters (Bhuse *et al*. 2003), optical filter (Tojoyi *et al*. 1990), antibacterial and antifungal (Amelia *et al*. 2011; Haram *et al*. 1992; Gracia *et al*. 1999). Only few reports have been published on antibacterial and antifungal test for copper selenide compared to its next of kin (copper sulphide and copper oxide). It has been reported that the composition and the crystal structure of the synthesized copper selenide NPs are usually dependant on the preparation method used. However, the preparation methods and sizes or shapes control are less flexible than other selenide-containing material such as zinc selenide and the studies relating to their optical properties are limited (Wang *et al*. 1998).

Copper selenide (CuSe) quantum dots, copper selenide (Cu_3Se) nanoplates, copper selenide (CuSe) nanotubes, and copper selenide (Cu_3-xSe_2) nanotubes and their hierarchical nano dendrites have been produced by thermolysis of single source precursor (Zhang *et al*. 2002), ultrasonochemical techniques (Malik *et al*. 1999), template-directed reaction (Li *et al*. 2002), electrochemical crystallization process (Yu *et al*. 2009), and hydrothermal method (Wang *et al*. 1999), respectively. Gracia *et al*. (2010) have also reported the preparation of chemically deposited copper selenide ($Cu_{2-x}Se$ and Cu_3Se_2) thin films, using sodium selenosulfate as the selenium source. Recently, $Cu_{2-x}Se$ nanoparticles have been produced via a hot-injection method, which used relatively unstable and air sensitive CuCl at a relatively high temperature (Choi *et al*. 2010).

1.2.2. Copper sulphide nanoparticles

As an earth abundant, important p-type semiconductor, copper sulphide exhibits at least seven equilibrium phases which are: monoclinic low-chalcocite (Cu_2S) (Evans *et al*. 1979), hexagonal high-chalcocite (Cu_2S) (Sigman et al., 2003), monoclinic djurleite ($Cu_{1.96}S$) (Evans et al., 1979), hexagonal digenite ($Cu_{1.8}S$) (Harbottle *et al*. 1982), monoclinic roxbyte ($Cu_{1.78}S$), orthorhombic anilite ($Cu_{1.75}S$) (Skirma *et al*. 2012), and hexagonal covellite (CuS) (Mumme *et al*. 1998). Many unusual electronic, optical, and other physical and chemical properties that copper sulphide exhibits, result from the existence of several polymorphic forms of its compositions (Gracia *et al*. 2010; Evans *et al*. 1979; Sigman *et al*. 2003; Harbottle *et al*. 1982; Skirma *et al*. 2012; Mumme *et al*. 1998; Cordova *et al*. 2002; Lim *et al*. 2006). Various stoichiometric composition and crystallinity have been reported (Victoria *et al*. 1997; Ali *et al*. 2006; Hrubaru *et al*. 2015; Jiang *et al*. 2004). Therefore, various attempts have been made to synthesize copper sulphide with different shapes such as nanoparticles, nanoflakes, nanotubes, microspheres, flower-like structures, nanowires, nanoribbons etc. with different methods. These methods includes ultrasonic and microwave irradiation (Liao *et al*. 2001; Wang *et al*. 2004), mechanochemical (Balaz *et al*. 2003), chemical vapour reaction (Zou *et al*. 2008), hydrothermal (Zou *et al*. 2007), electrochemical techniques, photochemical reduction (Lisiekcki *et al*. 1993), hot injection (Jiang Tang *et al*. 2008), and thermal decomposition (Monteiro *et al*. 2001). These methods have successfully produced a wide varaety of shapes such as spherical chalcocite (Li *et al*. 2009), and djurleite (Chen *et al*. 2004; Lui *et al*. 2005), chalcocite roxbyte (Lim *et al*. 2006; Zhang *et al*., 2008), covellite nanodiscs (Ghezelbash *et al*. 2005; Du *et al*. 2007), anilite hallow nanocages (Dorfs *et al*. 2011), digenite irregular nanocrystals, nanoflakes, nanotubes, microspheres, flower-like structures, nanowires, and nanoribbons. Therefore, each stable phase has its own characteristic optical properties (Li *et al*. 2010). Among the mentioned preparative methods, hot-injection is the most effective method since narrow size distribution can be obtained through a rapid nucleation process soon after the injection of precursor molecules into a hot solvent. It has been reported in literature that the band gap of copper sulphide materials varies between 0.6 eV-2.35 eV depending on crystal structure and chemical composition (Sagade *et al*. 2008). Solanki *et al*. (2010) synthesized copper sulphide nanoparticles through water-to-surfactant molar ratio. The size, size distribution as well as the morphology were affected. Zeyu *et al*. (2014) synthesized copper sulphide by wet chemistry and their application in photothermal ablation of tumour cells was tested. The evaluation of these

copper sulphide nanoparticle mediated photothermal destruction was done using human cervical cancer HeLa cells with respect to laser dose and nanoparticle concentration. Their toxicity was evaluated by the 3-[4.5-dimethylthiazol-2-yl]-2.5-diphenyltetrazolium bromide (MTT) assay. Owing to their unique optical property, small size, low cost of production and low cytotoxicity, CuS nanoparticles are promising new nanomaterials for cancer photothermal oblation therapy (Xiao *et al*. 2014). Many more potential applications have been proven from viable optical and electrical properties of copper sulphide. Copper sulphide can be used in various fields such as in solar cells (Xiao *et al*. 2014), fluorescent devices (Nair *et al*. 1991), photothermal conversion of solar energy (Yamaguchi *et al*. 1996), microwave shielding coatings (Teteris *et al*. 2003), electro conductive electrodes (Savagodo *et al*. 1998), catalysts for coal liquefaction (Sang et al. 2002), solid lubricants (Alejandra *et al*. 2008), rechargeable batteries (Hu *et al*. 2002), selective radiation filters (Qin *et al*. 2005), photodetectors, as polarizers of infrared radiation (Grozdanov *et al*. 1994), active absorbent of radiowaves (Grozdanov *et al*. 1994), semiconductors, , low temperature gas sensors applications (Phathan *et al*. 2004), field emission, switching (Feng *et al*. 2007), sensing devices (Sagade *et al*. 2008), thermoreflecting coatings (Nair *et al*. 1991), eyeglass coatings, antireflecting coating (Iienikhena *et al*. 2008), thermoelectric cooling materials (Shen *et al*., 2009), superionic material (Abdullaeva *et al*. 2013), antibacterial and antifungal activities (Amelia *et al*. 2011).

1.2.3. Copper oxide nanoparticles

Metal oxides are found in nature and some are very useful in applications of our daily life both in science and technology. Among the oxides of transition metals, copper oxide nanoparticles are of special interest due to their wide range of applications which includes high efficiency as nanofluid in heat transfer and thermal conductivity (Chon *et al*. 2005; Das *et al*. 2003). They also have been reported to have the advantage of a lower surface potential barrier than that of metals, which affects electron field emission properties (Pathan *et al*. 2004). Novel properties can be improved further to shown excellent performance when CuO nanostructures are synthesized in comparison to bulk counterpart. Different nanostructures of copper oxide have been synthesized in the form of nanowire, nanorods, nano needle, nano-flower and nanoparticle (Swankar *et al*. 2010). Various methods have been proposed to produce copper oxide nanoparticles with different sizes and shapes such as thermal oxidation (Manmeet *et al*. 2011), sonochemical (Narongdet *et al*. 2011),

combustion (Yamukyan *et al*. 2008) and quick-precipitation (Pathan *et al*. 2004), one-step solid state reaction at room temperature, mechanical milling of commercial powders (Zhu *et al*. 2004). Hong *et al*. (2002) reported nanosized CuO synthesized by alcohothermal method for low temperature synthesis, the size of the particles was manipulated to remain between 3 nm – 9 nm by simply varying the reaction temperature. Narongdet *et al*. (2010) reported nanosized CuO nanoparticles of high purity that were synthesized by sonochemical method and proved that the crystallization and particle size was strongly dependent on the reaction time and calcination temperature. High physical and chemical stability of copper oxide nanoparticles renders them extremely useful in various applications such as catalyst (Yu *et al*. 2009), emitter (Lane *et al*. 2010), optoelectronics (Swankar *et al*. 2010), good gas sensing material (Greenwood *et al*. 1990), catalysis (Sang *et al*. 2002), and solar cells (Greenwood *et al*. 1990). Moreover, the extremely high surface areas and unusual crystal morphologies endow copper oxide nanoparticles with antimicrobial activity, and their dose dependently inhibit *Escherichial Coli Strains*, but not *Salmonella tryphimurium* (Kadhim *et al*. 2015; Miranda *et al*. 2013; Longano *et al*. 2012; Abass *et al*. 2017; Kadhim *et al*. 2016). This finding suggests a way to develop novel and specific antimicrobial agent (Stoimenov *et al*. 2002).

1.2.4. Medicinal plants

Southern Africa is one of the richest centers of plant diversity in the world. The flora is not only extremely rich and diverse (about 24 300 higher plant taxa) but is also largely endemic in character (Arnold *et al*. 1993). These plants have been used throughout history for their medical properties. Traditional medicines play an important role in the management of chronically painful and debilitating joint conditions, particularly in the rural Africa. Medicinal plants contain active constituents in any of their parts like roots, stem, leaves, bark, fruit, and seeds

In Africa folk medicine, at least 24 species of *Combretum* have a range of uses for problems ranging from heart and worm remedies to wound dressings, treatment of the mentally ill, and scorpion stings (Sala *et al*., 2002). Most African people use boiled root decoction to treat constipation, headaches, stomachs, fever, dysentery and swellings, and as anthelmintic for hookworm. The root decoction has been used to induce abortion and treat constipation, and leprosy (Eloff *et al*. 2005). The leaves are chewed, soaked in water and the juice drunk for chest

complaints. It can also be used as an inhalant in a hot steam bath. The roots and leaves together are believed to be an antidote for snake bites. The most frequently utilized plant part is the underground part (root/rhizona/bulb) (42%). The largest number of remedies are for treating gastrointestinal disorders and parasitic infections (22%). The administration routes are orally (51.4%), externally (38.6%) nasal (71.9%) and ear (2.1%) (Eloff *et al*. 2005).

Combretaceae and *Acacia mearnsii* are rich in wide variety of free radical scavenging molecules, such as phenolic compounds, (e.g. phenolic acids, flavonoids, quinones, coumarins, lignins, stilbenes, tannin's), nitrogen containing compounds (alkaloids and amines), vitamins, terpenoids (including carotenoids) and some other endogenous metabolites, which are rich in antioxidant activity that may lead to anti-inflammatory, anti-atherosclerotic, anti-tumour, antimutagenic, anti-carcinogenic, antibacterial or antiviral activities to some extent. Owen *et al*. (2000) have reported antioxidant potential of 24 African *Combrettum* species, (Mosoko *et al*. 2005). Eloff *et al* (2005) discovered that all leaf extracts from 27 South African *Combrateceae* exhibit antibacterial activity against *S. aures, E. coli, E. faecalis* and *P. aeruginosa*. Baba-Moussa *et al*. (1999) reported on the antifungal activity of 7 Western Africa *Combretaceae* species used in traditional medicine. Masoko *et al*. (2007) investigated 24 South African *Combretaceae* species against 5 fungal animal pathogens (*Candida. albicans, Cryptococcus neoformans, Asperrgillus fumigates, Microsporum canis* and *Sporothrix schenkii*). McGaw *et al*. (2001) reported on the anti-inflammatory and antischistosomal activity or effects of *Combretum* species. Hydro alcoholic extracts of medical plant, *Combretum molle* is traditionally used in the treatment of various skin disorder and was screened for antimicrobial activity against different strains of bacteria and fungi, known to cause different types of skin infections (Asfaw *et al*. 1998). Lui *et al*. 2007 reported on the relationship between antioxidant activity of *Acacia mearnsii* and anti-tumor activity. In 2010 Hung *et al*. also reported a relationship between antioxidant activity of *Acacia mearnsii* and viability of human neuroblastoma SH-SY5Y cells while Ikorashi *et al*. (2018) reported the anti-hypertension effect of *Acacia mearnsii.*

1.3. Problem statement

The continuous development of anti-biotical resistant strain of microbial pathogens is a growing problem, is therefore extremely important to discover and develop new antimicrobial agents such

as those containing nanoparticles. The nanoparticles exhibit various unique properties which depend on their synthesis. Hence there is a growing need to design the nanoparticles in such way that they fit specific application such as antimicrobial activity. Nonetheless there are still widespread challenges on the toxicity of metal chalcogenide nanoparticles. Organic molecules such as those extracted from plants can be attached to nanoparticles and make them biocompatible while reducing their toxicity. The active compounds from plants may inhibit bacteria through different mechanisms than conventional antibiotics and therefore be of clinical value in the treatment of resistant microbes.

1.4. Aim and Objectives

1.4.1. Aim of the study

To synthesize copper chalcogenide nanoparticles and extraction of active compounds from medicinal plants then compare their antimicrobial activity.

1.4.2. Objectives

- To synthesize copper oxide, copper selenide and copper sulphide nanoparticles through parameter optimization (capping agent, time, temperature and precursor concentration).
- To characterize copper oxide, copper selenide and copper sulphide nanoparticles using UV/Vis, PL spectrometry, TEM, and XRD.
- To test the antimicrobial activity of synthesized copper chalcogenide nanoparticles against Gram-negative bacteria *Escherichia coli* and *Pseudomonas aeruginosa,* Gram-positive bacteria *Staphylococcus aureus* and *Enterococcus faecalis,* and fungi *Candida albicans.*
- To extract active compounds from *Combrettum Molle* and *Acacia Mearnsii* medicinal plants and study their antimicrobial activity against Gram-negative bacteria *Escherichia coli, Pseudomonas aeruginosa* and Gram-positive bacteria *Staphylococcus aureus* and *Enterococcus faecalis,* and fungi *Candida albicans.*
- To combine the plant extracts with the synthesized nanoparticles for antimicrobial activity against Gram-negative bacteria *Escherichia coli, Pseudomonas aeruginosa* and Gram-positive bacteria *Staphylococcus aureus* and *Enterococcus faecalis* and fungi *Candida albicans.*

CHAPTER 2

RESEARCH METHODOLOGY

2.1. Chemical reagents and materials

Oleylamine (OLA), trioctylphosphine (TOP), copper (I) chloride, selenium powder, sulphur powder, urea solid, methanol (99.5), acetone (99.8), toluene, ethanol, chloroform, Acetone (99.8%), chloroform, 1.1-diphenyl-2-picryl hydrazyl (DPPH) (37%), quercetin (95.5%), Folin-Ciocalteu's phenol reagent, sodium carbonate, gallic powder (97.5%), aluminium chloride ($AlCl_3$) (97%), ascorbic acid (99.5%), vanillin, ethyl acetate, sulphuric acid from Sigma Aldrich. Muller-Hinton broth (MHB), Muller-Hinton Agar (MHA), Malt-Extraction broth (MEB), Malt-Extraction Agar (MEA) Neomycin, Amphotericin, Resazurin, were analytical grade, and were purchased in Neogen. *Escherichia coli, Pseudomonas aeruginosa*, *Candida albicans*, *Staphylococcus aureus* and *Enterococcus faecalis*. *Combrettummolle* and *Acacia mearnsii* were purchased from Anatech. Plant leaves were collected in January 2016 at Vaal University of Technology in Vanderbijlpark in the province of Gauteng, South Africa.

2.2. Experimental Procedure

2.2.1 Synthesis of copper selenide, copper sulphide and copper oxide nanoparticles

Oleylamine (OLA) (5 ml) was placed in a three-neck flask; equipped with a reflux condenser (waterless condenser), thermometer under a nitrogen atmosphere. The content was heated to 120 °C under nitrogen environment with a magnetic stirrer on it. About 330 mg (0.0033 mol) of copper chloride was dispersed into 3 ml of OLA or TOP and injected into OLA that is in the three-neck flask via a syringe. The content was heated up to 220 °C, at which a solution of about 26.06 mg (0.0033 mol) of selenium (sulphur or urea) in 3 ml of OLA or TOP was added via syringe. The content was heated at 220 °C for about 30 minutes, followed by cooling to 80 °C, then cleaning twice with ethanol and once with acetone via centrifugation at 5000 rev/min for 10 min. The precipitate was left to dry for 24 hours at room temperature. The sample was dispersed into toluene,

sonicated for 30 minutes then characterised using Ultraviolet Visible spectroscopy (UV-Vis), Photoluminescence (PL) and Transmission electron microscopy (TEM). The solid sample was further characterized with XRD.

2.2.2. Preparation of plant extracts

The leaves of (*Combretum molle* and *Acacia mearnsii*) were collected, washed with water, air dried and crushed to a fine powder with a laboratory blender. The plant powder (2.0 g) was transferred to four different beakers for each plant. 200 ml of solvents with different polarities (chloroform, methanol, acetone and water) was added to each beaker, respectively, and stored at room temperature in a dark place. After 24 hours, infusions were filtered through Whatman No. 1 filter paper and the residue was re-extracted with equal volume of solvents to ensure maximum extraction of organic compounds. After 24 hours the process was repeated. The combined supernatants were evaporated to dryness under fume hood. The obtained extracts were kept in sample vials and stored in a refrigerator for the characterization of phenols, flavonoids, antioxidant, synthesis of nanoparticles and for antimicrobial study.

2.2.3. Phytochemical analysis of plants extracts

The crude methanolic extract of the two plants was re-dissolved in methanol. Few drops of each extract (*Combrettum molle* and *Acacia meanrsii)* were spotted on the line near the bottom of Thin Layer Chromatography (TLC) plates. The TLC plate was then placed on a shallow pool of different mobile solvent systems (ethyl acetate, methanol, and water) (Eloff *et al*. 2002) in a developing chamber such that only the bottom of the plate is in the liquid and the chamber was closed. The plate was removed from the developing chamber, air dried and sprayed with the vanillin-sulphuric acid reagent (0.1 g vanillin, 28 ml methanol, 1 ml sulphuric acid) for the detection of higher alcohols, phenols steroids and essential oils. The plate was air dried again then heated in oven at 105 ºC for 5 - 10 minutes. The process was repeated again but this time instead of using vanillin spray, DPPH was used. The plate was sprayed with DPPH spray (0.1 g of DPPH in 100 ml of methanol), heated at 105 ºC until the colors of chromatograms were optimally developed.

2.2.4. Determination of total phenolic contents in the plant extracts

The concentration of phenols in plant extracts was determined using Folin Ciocalteu reagent (Maslennikov *et al*. 2013). Methanolic solution of each plant extract in the concentration of 1 mg/ml was used in the analysis. The reaction mixture was prepared by mixing 1 ml of (0.1 mg/ml) phenolic solution of extract, 1.5 ml of Folin reagent and 1.5 ml of sodium carbonate (0.05 mg/ml). The sample was shaken and thereafter incubated for 1 hour at room temperature. The absorbance was determined using double beam Perkin Elmer UV/Vis absorption spectroscopy at λ_{max} = 300 nm. Phenols and flavonoids are known to have an absorption maximum in the range 230-340 nm hence the absorption spectroscopy was set at λ_{max} = 300 nm. The samples were prepared in triplicate for each analysis and the mean value of absorbance was obtained. The calibration curve was prepared by preparing gallic acid solutions in methanol at concentrations 0, 10, 20, 30, 50, 80, and 100 mg/L in methanol. The concentration of phenols was read from the calibration curve and expressed in terms of gallic acid equivalent (mg of GA/g of extract).

2.2.5. Determination of flavonoids concentration in the plant extracts

Aluminum chloride colorimetric method was used for determining the concentration of flavonoids in plant extracts (Chang *et al*. 2002). The concentration (0.1 mg/ml) of plant extract solution was used for each plant in the analysis. The 3 ml of the (of 1 mg/ml) sample was mixed with 3 ml of aluminum chloride (0.25 into 10 ml). The sample was shaken and thereafter incubated for 1 hour. The absorbance of the reaction mixture was measured using double beam Perkin Elmer UV/Vis absorption spectroscopy at λ_{max} = 300 nm. The samples were prepared in triplicate for each analysis and the mean value of absorbance was obtained. The calibration curve was prepared by preparing quercetin solutions at concentrations 0 to 100 mg/L in methanol. The concentration of flavonoids was read from the calibration line and expressed by quercetin equivalent (mg of QU/g of extract).

2.2.6. Determination of antioxidants concentration in the plant extracts

The ability of the plant extract to scavenge 1, 1-diphenyl-2-picryl hydrazyl (DPPH) free radicals was assessed by the standard method (Cook *et al*. 1996) adopted with the suitable modification (Koleva *et al*. 2002). The stock solution of extracts was prepared for each solvent to achieve the concentration of 100 ppm. The working solution was prepared from the stock solution to achieve 100 ppm in a 50 ml flask. Dilutions were made to obtain the desired concentrations. Diluted

concentrations (3 ml) were mixed with 3 ml of DPPH in concentration of 50 ppm. The samples were incubated for 30 minutes together with the standards in a dark place. The absorbance was recorded at 517 nm. The control sample contained all the reagents except the extract. Percentage inhibition was calculated using equation (11) whilst IC_{50} values were estimated from the % inhibition versus concentration plot, using a non-linear regression algorithm. The data were presented as mean values +/- standard deviation (n = 3),

% inhibition = (A of control - A of sample / A of control) *100 (11)

2.2.7. Solubility study

The solubility of the synthesized copper chalcogenides nanoparticles was investigated to understand the surface properties before the antibacterial study and to identify the suitable solvent for both nanoparticles and plant extracts. About 0.01 g (copper selenide, copper sulphide, copper oxide nanoparticles, *Combretum molle* extracts and *Acarcia mearnsii* extracts) were dissolved in 2 ml of acetone, water, chloroform, ethanol and dichloroethane at room temperature and sonicated for 1- hour time. The concentration of each content was then measured using UV/Vis to determine the solubility of nanoparticles and plant extracts and the results are depicted in Figure 3.56.

2.2.8. Combination of copper chalcogenide nanoparticles with medicinal plant extracts

The synthesized copper chalcogenide nanoparticles were further characterized with FTIR to identify the present functional groups. After characterization, the synthesized copper chalcogenides were washed further three times with acetone via centrifugation at 5000 rev/min for 10 min. The precipitate was left to dry for 24 hours at room temperature. Thereafter, the nanoparticles were systematically combined with ethanolic extracts of both *Combretum molle* and *Acacia Mearnsii* by adding amount of 30 mg of each copper chalcogenide (CuSe, CuS and CuO) into six separate test tube. An amount of 30 mg of ethanolic extracts of *Combretum molle* was added to one set of three test tubes containing 30 mg of copper chalcogenides, then another 30 mg of ethanolic extracts of *Acarcia mearnsii* was added to the second three set of test tube also containing 30 mg of copper chalcogenides. About 3 ml of 0.17% ethanol solution was added to each test tube and the solution was sonicated overnight. The content was characterized by FTIR spectroscopy to identify the interaction between nanoparticles and plant extracts.

2.2.9. Antimicrobial study

The antimicrobial study of the synthesized nanoparticles and plant extracts was carried out by testing them against Gram-positive bacteria strains (*Staphylococcus aureus* and *Enterococcus faecalis*), Gram-negative bacteria strains (*Escherichia coli* and *Pseudomonas aeruginosa*) and fungal strains (*Candida albicans*). The disk diffusion method was first used to screen the antimicrobial activity thereafter Minimal Inhibitory Concentration (MIC) method was used and *Neomycin* was used as a negative control for anti-bacterial studies and *Amphotericin* for anti-fungal studies.

(a) Preparation and test for Agar disk-diffusion method

Stock cultures were maintained at 4 °C on slopes of nutrient agar. Active cultures (*Escherichia coli, Pseudomonas aeruginosa, Candida albicans, Staphylococcus aureus* and *Enterococcus faecalis*) for the experiment were prepared by transferring a loop full of cells from the stock cultures to a flask containing a Muller-Hinton broth (MHB), Muller-Hinton Agar (MHA) and incubated for 24 hours at 37 °C.

Disk diffusion plates for bacterial test were prepared by weighing 10 g of Malt-Extraction Agar (MEA) into 200 ml flask and 200 ml of distilled water was added. The solute was dissolved using a microwave, thereafter autoclaved for 1 hour then cooled to room temperature. The plates were prepared by transferring about 15 ml of a molten media into a sterile disk plates under sterilised fume hood. Disk diffusion plates for fungal test were prepared the same way but 7.6 g of Muller-Hinton Agar (MHA) was used instead of Malt-Extraction Agar. The disk plates were left for 10 minutes to solidify. Inoculum suspension was swabbed uniformly and allowed to dry for 5 minutes. A well of 6 mm was created on a disk and 50 µL (0.06 mg/L) of the sample was added. The sample was allowed to diffuse for 5 minutes then incubated at 37 °C for 24 hours. In general, antimicrobial agent diffuses into agar during the incubation period and inhibits germination and growth of the test microorganism and the diameter of their inhibition zones are measured.

(b) MIC test method

Minimum inhibitory concentration (MIC) of the plant extracts, copper chalcogenides nanoparticles (copper selenide, copper sulphide and copper oxide) and nanoparticles combined with plant extracts was determined using the micro dilution bioassay as described by (Eloff, 1998). Overnight

cultures (incubated at 37 °C) of *Escherichia coli, Pseudomonas aeruginosa, C albicans, Staphylococcus aureus* and *Enterococcus faecalis, Klebsiella pneumoniae* and bacterial strains were each diluted with sterile Mueller-Hinton broth (MHB) to give final inoculum of approximately $1x10^6$ CFU/ml (colony forming units). 60 mg of plant extract, copper chalcogenides nanoparticles and the combination of plant extracts together with plants were each dissolved in 3 ml of 0.17% ethanol solution to make a concentration of 20.0 mg/ml. One hundred (100) microliters of each solution was serially diluted two-fold with sterile Mueller-Hinton broth in a 96-well microliter plate for each of the four bacterial strains. A two-fold dilution of neomycin (20 mg/ml) was used as positive control and water was used as negative control. One hundred microliters of each bacterial culture was added to each well. Bacterial growth was indicated by adding 50 µl of 0.02% Resazurin. The plates were covered and incubated at 37 ºC for 24 hrs. Since the colorless tetrazolium salt is biologically reduced to a red product due to the presence of active organisms, the MIC values were determined as the concentration in the last wells with no color change observed. Bacterial growth in the wells was indicated by a reddish-pink color. The assay was repeated twice with two replicates per assay.

2.2.10. Characterisation techniques

The optical properties of the synthesized material were determined by dissolving the synthesized nanoparticles in a toluene and placing the content in a quartz cuvette (1 cm path length). The absorbance measurements were recorded using a double beam Perkin Elmer lambda 25 UV/Vis spectroscopy with a wavelength range of 0-900 nm. The emissions were measured using a single beam Jasco spectrofluorimeter FP-8600 with XE lamp at 150W operated at 200-1010 nm. The morphology of the particles was determined by drop casting the particles that were dissolved in toluene to a copper grids then images were taken using Transmission electron microscopy Technai G^2 TEM Spirit operated at 200 kV. The X-Ray diffraction patterns were determined using Bruker D2 Phase analyser, XRD Beam knife 3 mm (5 mm is all the way up), diffracted beam anti-scatter slit 6.6 mm. The chemical structure of nanoparticles and plants were determined using Fourier transform infrared analysis were recorded in a FT-IR/FT-NIR Perkin Elmer 400 spectrometer, universal ATR with the diamond detector with a wavelength range 650 to 4000 cm^{-1}.

CHAPTER 3

RESULTS AND DISCUSSION

3.1. Overview on the Synthesis of copper chalcogenide nanoparticles

Copper chalcogenides inclusive of copper selenide, copper sulphide, and copper oxide were explored for their synthesis using trioctylphosphine and oleylamine as capping agents and other optimized conditions such as precursor concentration ratio, temperature and reaction times. Copper (I) chloride salt was used as a source of copper whereas sulphur and selenide powders as sources of the sulphide and selenide ions, respectively, and urea as a source of oxygen. The three chalcogenides behave differently from one another even though they all from the chalcogen group. Their differences are due to their electronegativity, their ionisation energy or ionisation potential (IP) and their electron affinity which decrease with the increase of atomic weight in the group (from oxygen to selenium). These trends are useful in predicting the reactivity of the three towards other elements especially transition metals. Therefore, this makes oxygen to be more reactive and more metallic than the two because the metallic properties also increases as the atomic number increases. The size of the three chalcogenides also affect their reactivity and stability with oxygen being very small hence very stable and highly reactive compared to sulphur and selenium. Nonetheless, sulphur behaves more like selenium in reaction than oxygen because the radius of sulphur is about 60% larger than that of oxygen hence similar trends are observed in copper selenide and copper sulphide nanoparticles whereas copper oxides nanoparticles showed a trend different from the previous.

During the synthesis of nanoparticles, the capping molecule is usually employed to prevent particles from agglomeration and aggregation and to provide passivation and electronic stabilisation. It is therefore important to choose a good capping molecule that does not bond strongly to the precursors as this would prevent particles from growing. The capping molecule should not have weak bonds with the precursors either as the particles would grow bigger. It is

necessary to understand the rate at which capping molecule attaches and detaches to the surface as this influences the growth rate and the final size of particles. The capping molecules that were employed in this study (trioctylphosphine and oleylamine) have similar features such as being able to dissolve nanoparticles and binding to the surface. . The capping molecules are both oily and liquids at room temperatures, they both provide good interaction and they can be used at higher temperatures as they both have high boiling points (TOP = 291 ºC; OLA = 364 ºC). Their densities are not far off from each other (TOP = 0.831g/ml; OLA = 0.813 g/ml) and they can both act as solvents and stabilizers. Nonetheless, the two capping molecules also different in their chemical features and reactivity or interaction. Trioctylphosphine is an alkyl with a long chain ($C_{24}H_{51}P$) that uses its phosphine group (PH_3^+) for interaction whereas oleylamine is a long-chain primary alkyl amine that uses its amine group (NH_2^-) for interaction.

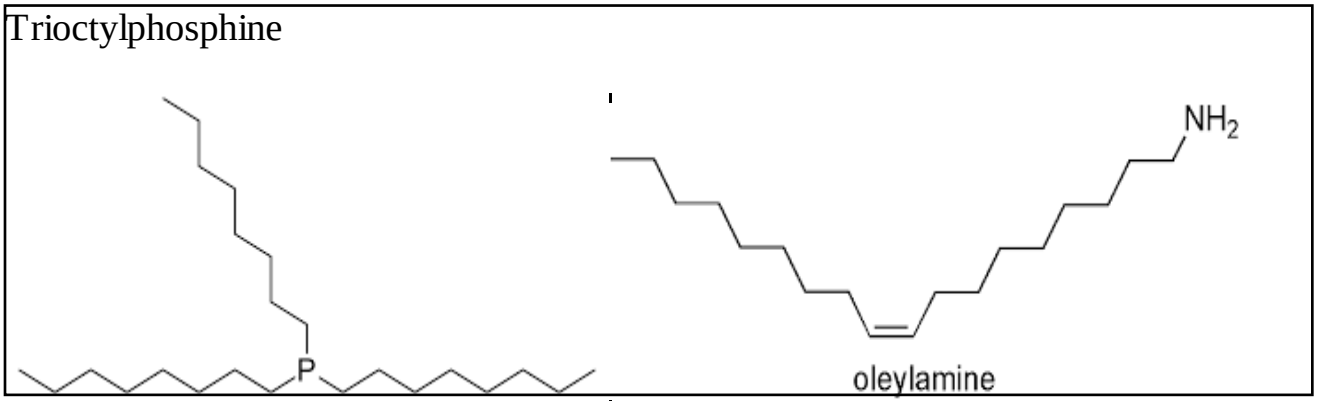

Figure 3.0: Chemical structure of trioctylphosphine and oleylamine

The increased proton affinity of phosphines is due to the stabilization of phenyl phosphonium ion by Л donation from phenyl group to the empty orbitals of phosphorus in the PH_3^+ group, in contrast, the amines are rather stabilized by conjugation of nitrogen lone pair with the aromatic ring (Onwudiwe *et al.* 2015). Generally, amine group has higher affinity for protons than phosphine due to the lone pair of electrons it possesses which it easily donates to H^+ compared to phosphine. The high proton affinity of oleylamine makes it to interact faster than trioctylphosphine. As the first condition to be explored, the comparison between the capping agents was done to probe the effect of the interaction between phosphine and the amine influences the particles in their properties. In literature, 3 ml of these capping molecules were used in the

synthesis of nanoparticles when hot-injection method was employed therefore, in this study, 3 ml of each capping molecule was used for the synthesis of copper selenide, copper sulphide and copper oxide nanoparticles.

The second condition explored was the precursor concentration ratio which was varied in the mole ratios 1:1, 1:2 and 2:1 using oleylamine as both solvent and capping molecule. The third condition explored was the reaction time which was set at 15, 30, 45 and 60 minutes in OLA and the last condition was the reaction temperature which was set 160 ºC, 190 ºC, 220 ºC and 240 ºC which was also investigated in OLA. Due to challenges experienced with the magnetic hotplate stirrers sourced from labotec, which are limited to heating up to 250 ºC, the maximum temperature of 240 ºC was used. This resulted in the last interval becoming 20 ºC instead of 30 ºC. After the synthesis of nanoparticles, the optical properties of the nanocrystals were studied using analytical techniques such as absorption and emission spectroscopy and their values were recorded using an extrapolation method. The FWHM was calculated using the emission spectra. The morphologies of nanoparticles were investigated by electron microscope discussed and the size of the particles was measured using image J software. The trends observed from the condition variations were also explored.

3.2. Synthesis of copper chalcogenide nanoparticles using trioctylphosphine and oleylamine

3.2.1. The effect of capping agent on the synthesis of copper selenide nanoparticles

(a) Optical properties of copper selenide nanoparticles

Nanoparticles are characterized by blue shift of the absorption edge with respect to its bulk material and this is usually considered as an indication of the decrease in size of the material (Gracia *et al.* 1999; Nelwamondo *et al*. 2012). When the particle size decreases, the band gap increases indicating that higher energy is required to excite an electron from the valance band to the conduction band and hence their absorbance shifts to the lower wavelength and thus referred to as blue shift and vice-versa (red shift). Therefore, to examine the absorbance of synthesized copper selenide nanoparticles, room temperature UV/Vis absorption and fluorescence emission

measurements were done as shown in Fig. 3.1. The absorption band edges and emission maxima for the copper selenide nanoparticles capped by TOP and OLA are listed in Table 3.1.

Table 3.1: Optical parameters of copper selenide nanoparticles synthesized using TOP and OLA as capping agents

Capping agent	Band edge (nm: eV)	Emission peak (nm)	FWHM (nm)
TOP	315(3.94)	342	37
OLA	560(2.21)	415	51

Both OLA and TOP-capped copper selenide nanoparticles had a large blue shift absorption compared to their bulk band gap (1180 nm). The absorption band edge of TOP-capped nanoparticles was observed around 315 nm which revealed a larger blue shift compared to OLA-capped nanoparticles which has an absorption band edge around 560 nm. The band edge values suggest that TOP-capped particles were smaller in comparison to those capped with OLA. This could be due to TOP being a stronger coordinating agent than OLA. The absorption curves of the two materials showed different line shapes predicting different optical properties and different crystalline phases. The emission spectra of the synthesized copper selenide nanoparticles are shown in Fig. 3.2. The emission peaks of TOP and OLA-capped nanoparticles were observed around 342 and 415 nm respectively. Both TOP and OLA spectra produced narrow emission peaks with a full width at height maximum (FWHM) of 37 nm and 51 nm respectively, suggesting monodispersed materials. This suggests that OLA-capped particles were less monodispersed than those from TOP-capped material. The emission peak of TOP-capped material is red shifted to its absorption peak whereas a blue shift is observed for OLA-capped material. The blue shift could be due to the longer-wavelength Localized Surface Plasmon Resonance absorption of the OLA-capped material which is observed in near IR region resulting to an anti-Stokes shift. Rokovich *et al.* (2008) deduced that the anti-Stokes shift photoluminescence (ASPL) occurs when the material emit light at shorter wavelength than which the material was illuminated because of thermal interactions with the excited atoms. Rokovich further elucidated that ASPL is often observed in semiconductor nanocrystals when the energy gap between the excitation energy and excited

electronic level is comparable or larger than the maximum energy in the material hence more energy is released than what was initially absorbed. Xiong *et al*. 2017 also reported on PbS quantum dots which produced an anti-Stokes shift photoluminescence spectrum and observed a gradual shift towards shorter wavelength when the excitation intensity was increased. This phenomenon was also observed when the excitation of TOP and OLA-capped material was increased (400 - 450 nm) and (300 - 350 nm), respectively. Their intensities were drastically reduced.

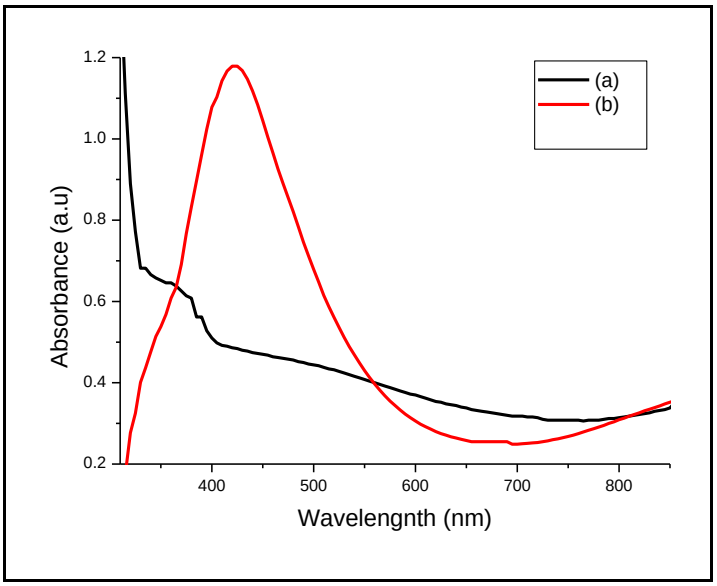

Figure 3.1: Absorption spectra of copper selenide nanoparticles synthesized using TOP (a) and OLA (b) as capping agents.

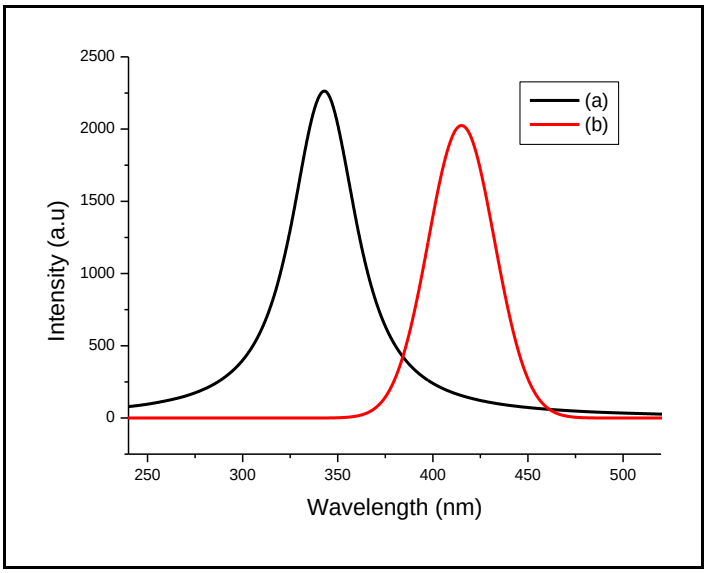

Figure 3.2: Emission spectra of copper selenide nanoparticles synthesized using (a) TOP and (b) OLA as capping agents.

(b) Morphology of the synthesized copper selenide nanoparticles

The TEM images of synthesized copper selenide nanoparticles are shown on Figure 3.3. Due to high agglomeration and mixed morphology, the particle sizes were not measured hence their corresponding size distribution graphs are not shown. The TEM images revealed that OLA- capped nanomaterials have mixed morphologies including hexagonal, spheres and truncated triangles-like structures. They gave broad size range forming sheet like structures, whilst TOP-capped nanomaterials gave smaller nanoparticles that are highly agglomerated with undefined shapes. The particle size difference between TOP-and OLA-capped nanomaterials explained the large blue shift that was observed between the absorption curves of the two materials. The agglomeration observed in TOP-capped nanomaterials might be due to high surface energy which resulted in increased forces of attraction between particles. The use of TOP as capping agent provided more steric hindrance compared to OLA and thus having smaller particles compared to the nanoplates produced by OLA. During the synthesis of OLA capped nanoparticles, the nuclei that were produced at the beginning of the reaction combined to form bigger particles through Ostwald ripening mechanism hence nanosheets were produced. TOP gave particles with size distribution ranging from 14 to 76 nm which indicates good population in comparison to OLA-capped nanoparticles in which much broader size range of 14 to 101 nm was observed. The broad size range observed in OLA-capped particles is inconsistent with its corresponding FWHM which

predicted a less monodispersed population than TOP-capped particles. Due to high agglomeration, TOP-capped material produced particles with undefined shapes unlike OLA capped material.

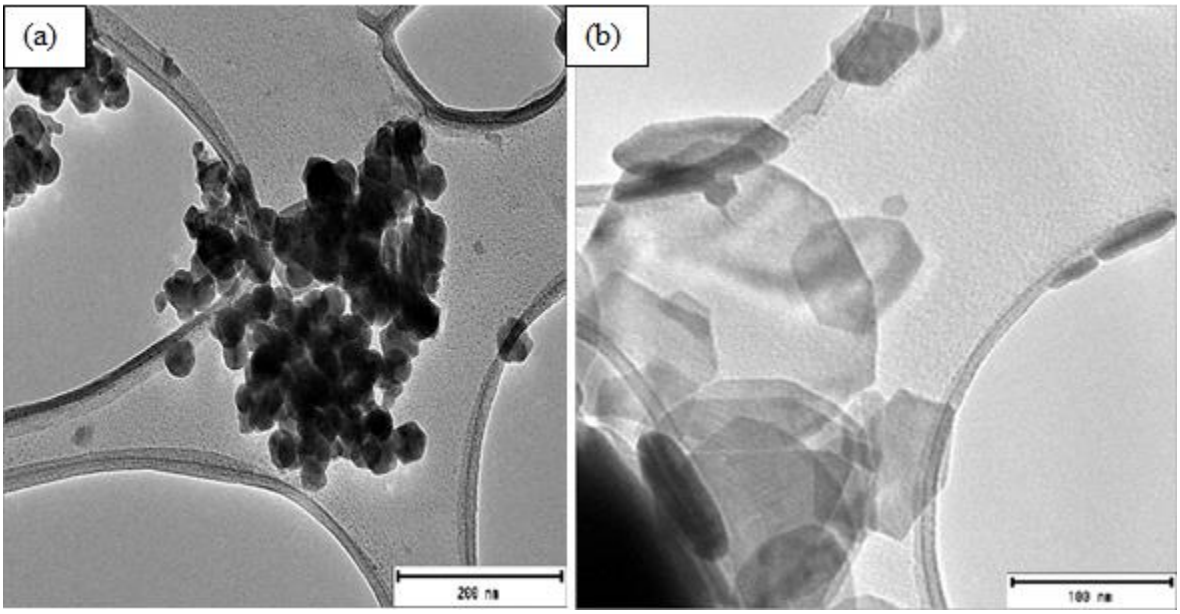

Figure 3.3: TEM images of TOP (a) and OLA (b) capped copper selenide nanoparticles

The XRD patterns (Figure 3.3) revealed some highly crystalline materials as depicted by the sharp peaks for both TOP and OLA capping agents. Both TOP and OLA capped materials produced cubic $Cu_{7.16}Se_4$ phase which is indexed to PDF card no. 01-071-4325. However, an additional phase of tetragonal Cu_3Se_2 with PDF card no.04-003-6622 was associated to Umangite phase in TOP capped particles. The crystal planes of the main peaks for both TOP and OLA-capped material ($Cu_{7.16}Se_4$) appeared at the same 2Theta values 27º, 45º, 53º, 65º, 72º, 83º and 89º corresponding to (111), (220), (311), (400), (331), (422) and (511), respectively. The additional peaks for the second phase (Cu_3Se_2) in TOP-capped particles are found at 25º, 31º, 40º, 48º, 50º, 51º and 56º for crystal planes (100)*, (210)*, (220)*, (301)*, (311)*, (202)* and (321)*, respectively.

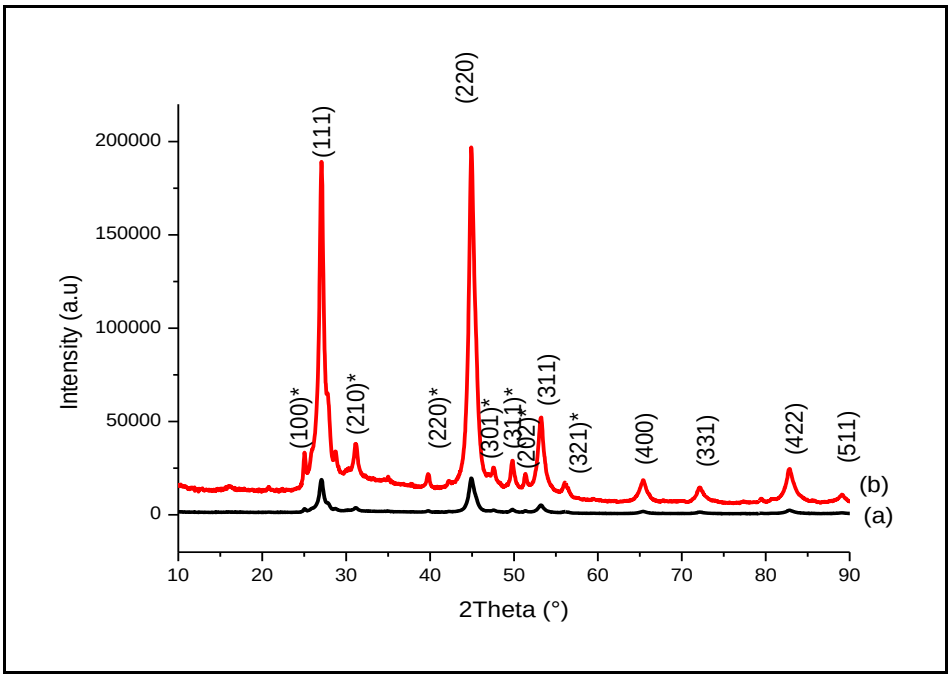

Figure 3.4: XRD patterns of OLA (a) and TOP (b)-capped copper selenide nanoparticles.

3.2.2. The effect of capping agent on the synthesis of copper sulphide nanoparticles

(a) Optical properties of copper sulphide nanoparticles

The absorption and emission spectroscopy of synthesized copper sulphide nanoparticles using different capping molecules are depicted in Figure 3.5 and 3.6 respectively. The extracted optical properties are listed in Table 3.2. The absorption band edge of TOP capped material was observed at 318 nm and indicates a large blue shift from that of OLA which was observed at 580 nm. The blue shift suggest that TOP capped material should have smaller particle size than OLA capped particles. The absorption band edges of both materials are blue shifted from their bulk band gap (1022 nm). This is an indication of a particle size reduction implying that relatively smaller size particles have been successfully synthesized.

Table 3.2: Optical parameters of copper sulphide nanoparticles synthesized using TOP and OLA as capping agents

Capping molecule	Band edge (nm: eV)	Emission peak (nm)	FWHM (nm)
TOP	318(3.90)	339	45
OLA	580(2.14)	599	85

Similar absorption curves are observed for the two materials capped with TOP and OLA, predicting similar optical properties unlike copper selenide nanomaterials when similar conditions were used. The emission peak of the OLA-capped material was found at 599 nm and red shifted from that of TOP-capped material which was oserved at 339 nm and this further confirms that OLA-capped material have bigger particle size compared to TOP-capped material. A narrow emission peak with FWHM of 45 nm predicting a monodispersed particle distribution for TOP-capped material was observed while its counterpart gave a broader emission peak with a corresponding FWHM of 85 nm suggesting a polydispersed distribution.

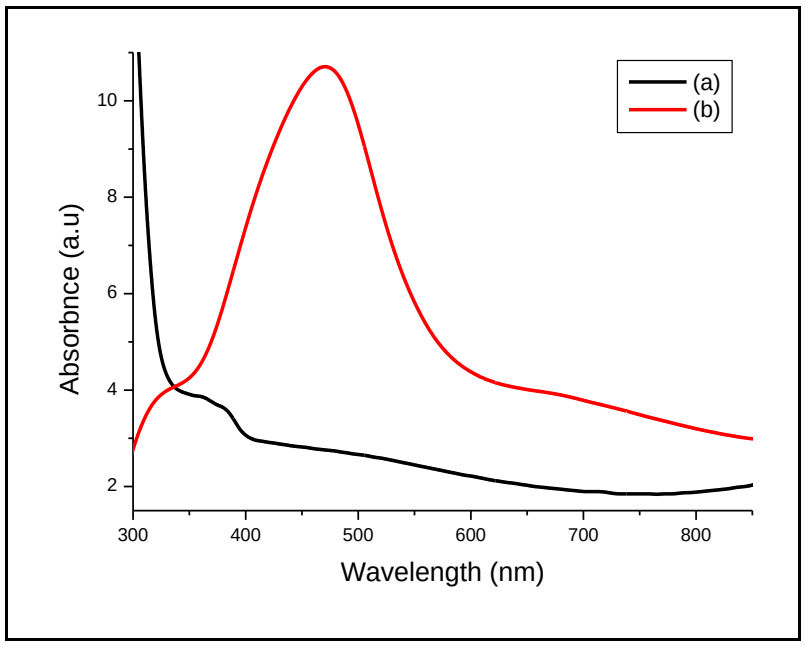

Figure 3.5: Absorption spectra of copper sulphide nanoparticles synthesized using TOP (a) and OLA (b) as capping agents.

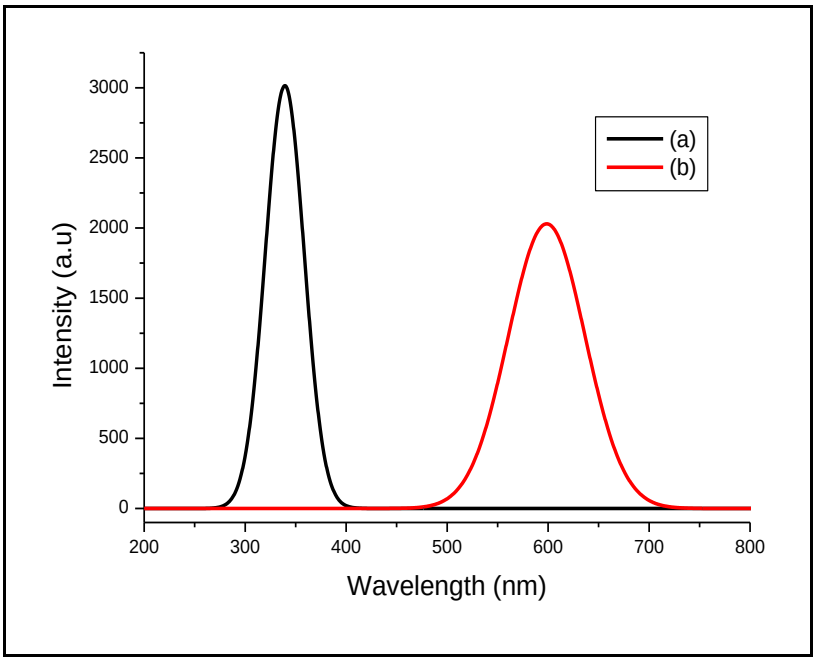

Figure 3.6: Emission spectra of copper sulphide nanoparticles synthesized using TOP (a) and OLA (b) as capping agents.

(b) Morphology of the synthesized copper sulphide nanoparticles

TEM images of the synthesized copper sulphide nanoparticles with different capping molecules are shown in Figure 3.7, and their corresponding size histograms are not shown due to mixed morphology of particles. TOP capped material produced smaller particles with size range from 11 nm to 74 nm whereas those capped with OLA produced a wide particle sizes with sizes ranging from 20 nm to 200 nm. The wide particle size distribution of OLA-capped material aligns with its optical characteristics which showed a broad emission peak and a larger FWHM of 85 nm predicting a polydispersed distribution. Both materials produced mixed morphologies. TOP-capped nanomaterials produced cubes, hexagonals and triangles like structures, while OLA-capped material produced the three above mentioned structures together with rods, truncated triangles and more undefined structures. The wider variety of particle shapes for particles produced by OLA capped material is also justified by its broader emission peak. Wide range of different shapes was also observed on copper selenide particles capped with OLA. This wide variety of shapes that OLA-capped material produced could be due to the preferential binding facet of OLA. An agglomeration was observed on OLA-capped material while TOP-capped material showed a well distribution of particles. The agglomeration observed in OLA as a capping agent can be

attributed to its longer chain bering NH_2 group with less binding ability towards copper chalcogenide materials. OLA-capped material produced both small and big particles. This suggests that with parameter optimization, a variety of structures can be produced with this capping molecule.

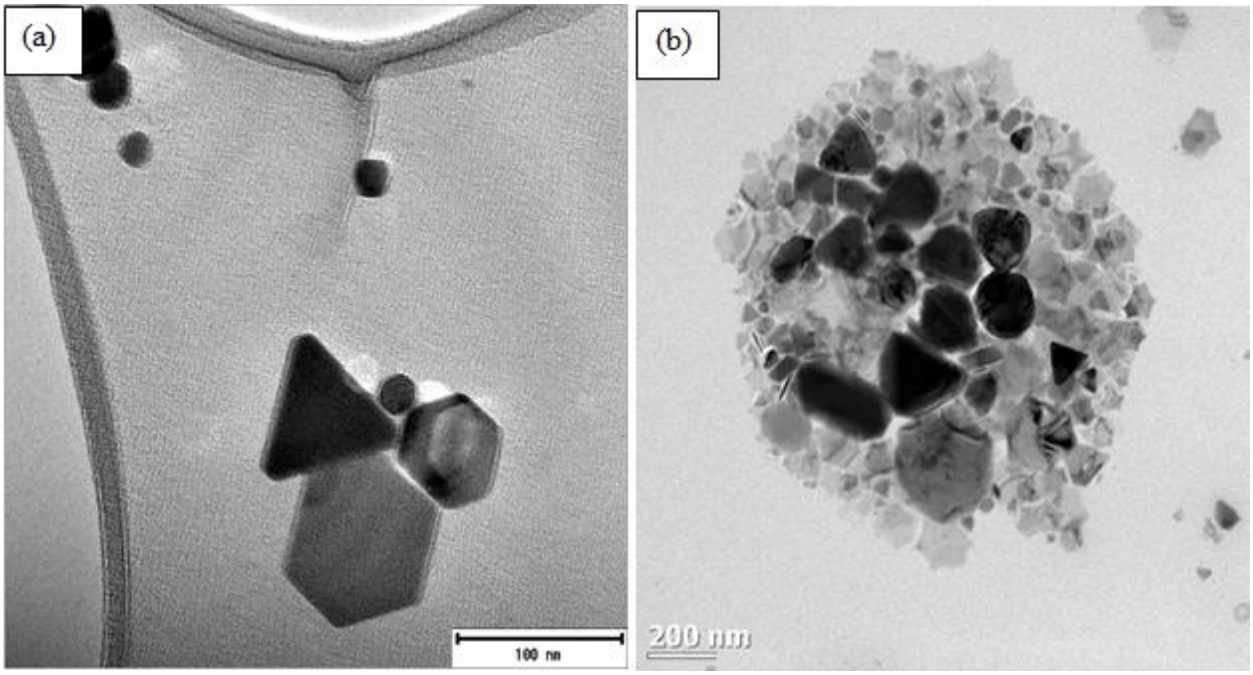

Figure 3.7: TEM images of TOP (a) and OLA (b) capped copper sulphide nanoparticles

The crystalline structure and chemical composition of the prepared materials were studied by XRD. The difraction patterns of the material capped with OLA and TOP are depicted in Figure 3.8. The diffraction patterns confirmed that copper sulphide nanoparticles were produced in both methods. Both TOP and OLA capped materials produced properties that were indexed to Cubic $Cu_{1.75}S$ phase which is indexed to PDF card no.04-006-0521. TOP capped material showed a second phase which was indexed to Roxbyite $Cu_{58}S_{32}$ (Anorthic) phase with PDF card no.00-064-0278. Both patterns showed major peaks at 2θ values 28º, 32º, 47º, 55º, 68º, 74º, and 86º corresponding to crystal planes (111), (200), (220), (311), (400), (331) and (422) of $Cu_{1.75}S$ phase. The peaks of the minor phase of TOP-capped material were observed at 2θ values 21º, 25º, 27º, 30º, 37º, 49º and 50º corresponding to crystalline planes [130]*, [114], [400], [224], [0117], [119]* and [208]. The TOP-capped material showed some impurities at 2θ values 34º, 36º, 62º, 65º and 71º which are denoted by +. These impurities could be due to unreacted reactants. The mixture of

phases for TOP-capped material was also observed in copper selenide material as well. Impurities of digenite Cu_9S_5 (Rhombohedral) phase indexed to PDF card no.00-047-1748 were also observed in OLA-capped material with crystalline planes that are obseved at 2θ values 26º and 30º corresponding to the indices [323] and [224], respectively denoted by the symbol *. The sharpeness of the diffractogram peaks in OLA capped material confirmed the bigger sizes of particles and good crystallity of copper sulphide nanoparticles than those of TOP capped material.

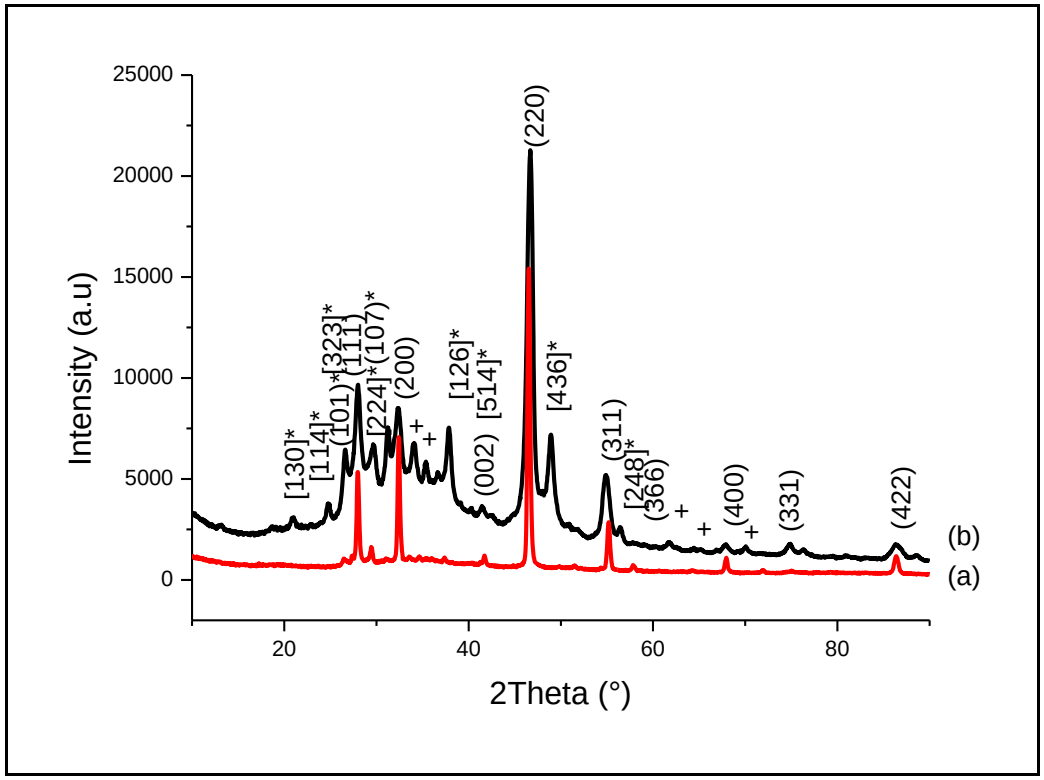

Figure 3.8: XRD patterns of OLA (a) and TOP (b) capped copper sulphide nanoparticles.

3.2.3. The effect of capping agent on the synthesis of copper oxide nanoparticles

(a) Optical properties of copper oxide nanoparticles

The absorption spectra of copper oxide nanoparticles capped with OLA and TOP are shown on Figure 3.9 and extracted optical parametrs are listed on Table 3.3.

Table 3.3: Optical parameters of copper oxide nanoparticles synthesized using TOP and OLA as capping agents

Capping molecule	Band edge (nm; eV)	Emission peak (nm)	FWHM (nm)
TOP	528(2.34)	502	72
OLA	492(2.49)	436	82

The absorption band edges of OLA and TOP-capped nanoparticles were observed at 492 nm and 528 nm, respectively. The band edges revealed that both materials are blue shifted from their bulk material with an absorption band gap of 1033 nm. The absorption band edge of OLA-capped material is blue shifted from that of TOP-capped material suggesting smaller particles for OLA-capped material. Both material produced identical absorption curve suggesting similar optical properties. This was not observed on copper selenide or copper sulphide nanocrystals. Similar optical properties of copper oxides nanoparticles might result from its high stability in thermodynamic reactions. Figure 3.10 depicts the emission spectra of the synthesized materials. The maximum emission intensity of TOP-capped material was found at 502 nm and was red shifted from that of OLA-capped material located at 436 nm. This is in agreement with the absorption spectra, predicting bigger particles for TOP capped particles. The emission peaks of both materials are blue shifted from their absorption bands. This phenomenon (ASPL) was also observed in copper selenide nanoparticles that are preveously discussed. TOP capped material produced a broader emisson peak compared to OLA capped material with FWHM of 82 nm while OLA produced an emission peak with FWHM of 72 nm. The broadness of this emission peak can be attributed to a wider size distribution or polydispersed material. The narrower emission peak of the OLA-capped material suggests a well dsitributed size population.

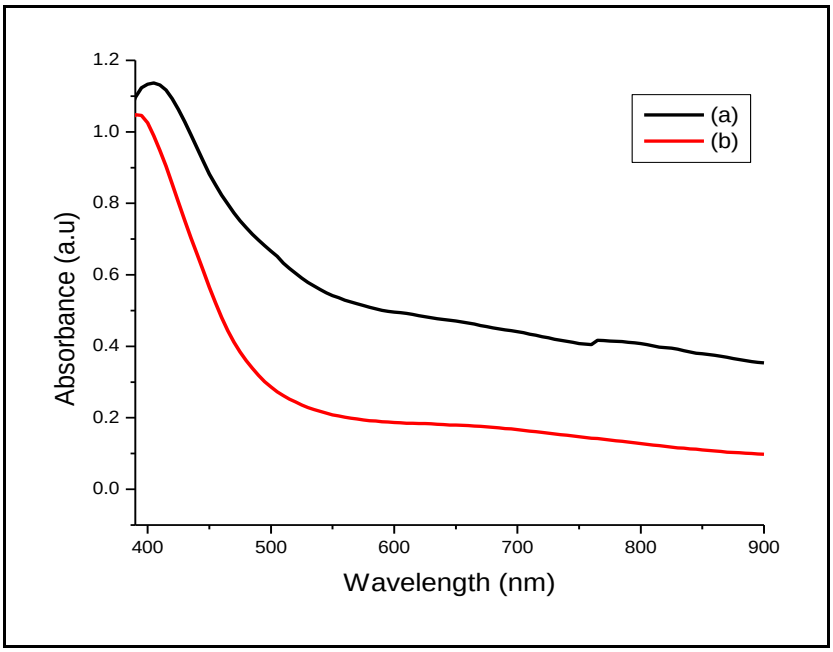

Figure 3.9: Absorption spectra of copper oxide nanoparticles synthesized using TOP (a) and OLA (b) as capping agents.

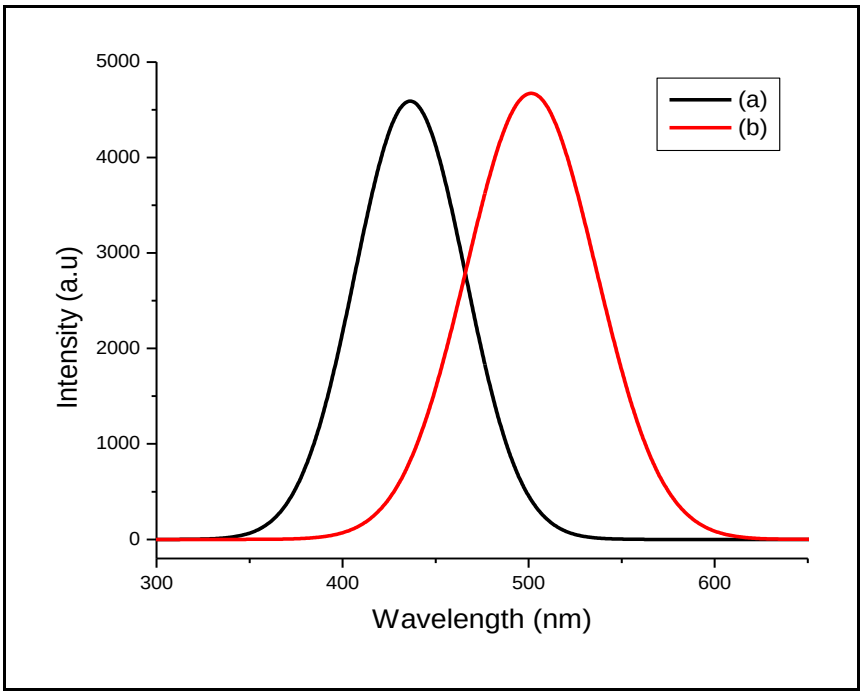

Figure 3.10: Emission spectra of copper oxide nanoparticles synthesized using TOP (a) and OLA (b) as capping agents.

(b) Morphology of the synthesized copper oxide nanoparticles

To study the morphology of the symthesized copper oxide nanoprticles, TEM analysis was conducted. TEM images of the yielded copper oxide nanoparticles capped with OLA and TOP are depicted on Figure 3.11. TEM images revealed that OLA-capped material are nearly spherical in shape with size average of 3 nm while TOP-capped material produced flackes like structures with average size of 25 nm. The smaller size of OLA-capped material is consitent with the corresponding optical properties which suggested smaller particles in comparison to TOP-capped nanoparticles. A bit of agglomeration of smaller particles is observed in TOP-capped material and this is consistent with the broadness of its corresponding emission peak. On the other hand OLA-capped material produced particles that are monodispersed and nicely persivised, and this is also in line to what was predicted by the optical properties of the correspondance. This is attributed to the ability of OLA as a good surfactant, solvent and reducing agent. The mixed morphology that was observed on copper selenide and copper sulphide OLA-capped nanocrystals was not observed on OLA-capped copper oxide nanoparticles rather small spheres like structures were observed. This could be due to the small size and high stability of oxides which resulted in sharp nucleation leading to uniform particles obtained.

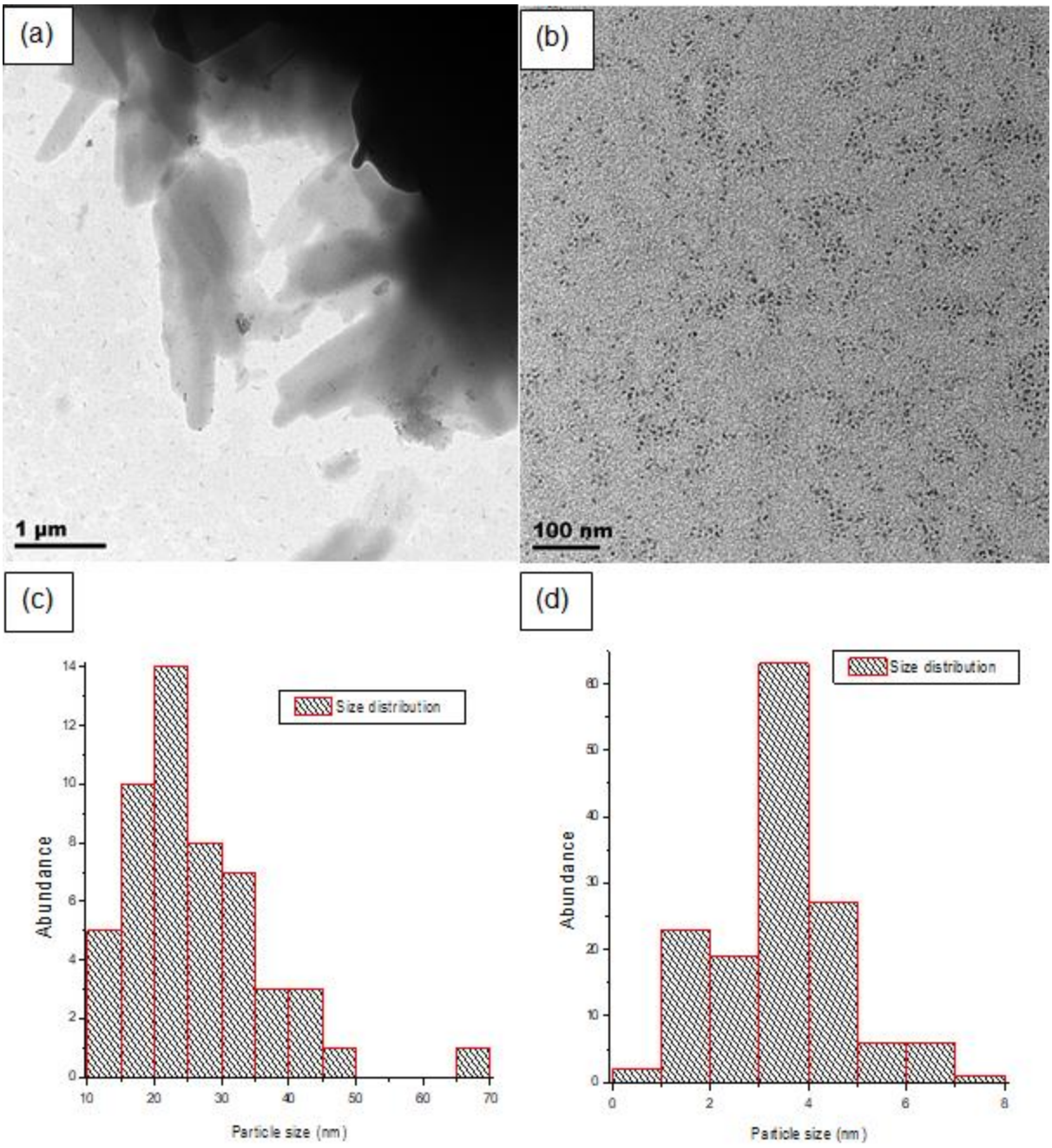

Figure 3.11: TEM images of TOP (a) and OLA (b) capped copper oxide nanoparticles with their corresponding size histograms (c) & (d) nanoparticles, respectively.

The XRD patterns of OLA and TOP-capped nanocrystals are displayed Fig. 3.12. The diffraction patterns confirmed the synthesis of copper oxide nanoparticles in both materials. The characteristic peaks of TOP-capped material are mostly found in Cubic phase Cu_2O which was indexed to PDF

card No. 77-0199. The XRD patterns of TOP-capped materials showed major peaks at 2θ values 36°, 44°, 64°, and 78° corresponding to crystal planes (111), (200), (220) and (222). OLA-capped material showed major peaks at 2θ values 36°, 42°, 47°, 54°, 56°, 64°, and 78° which can be indexed to Monoclinic phase CuO PDF card No. 48-1548 corresponding to planes (002), (002), (112), (112), and (004). The sharpness of the peaks confirms that highly crystalline particles were prepared in both OLA and TOP-capped materials. Copper oxide nanoparticles that were capped with OLA produced a single phase whereas a mixture of phases was observed in copper selenide and copper sulphide nanocrystals under similar synthetic conditions. This is attributed to high thermodynamic stability of copper oxides nanoparticles which resulted in stronger bonds leading to single phases produced.

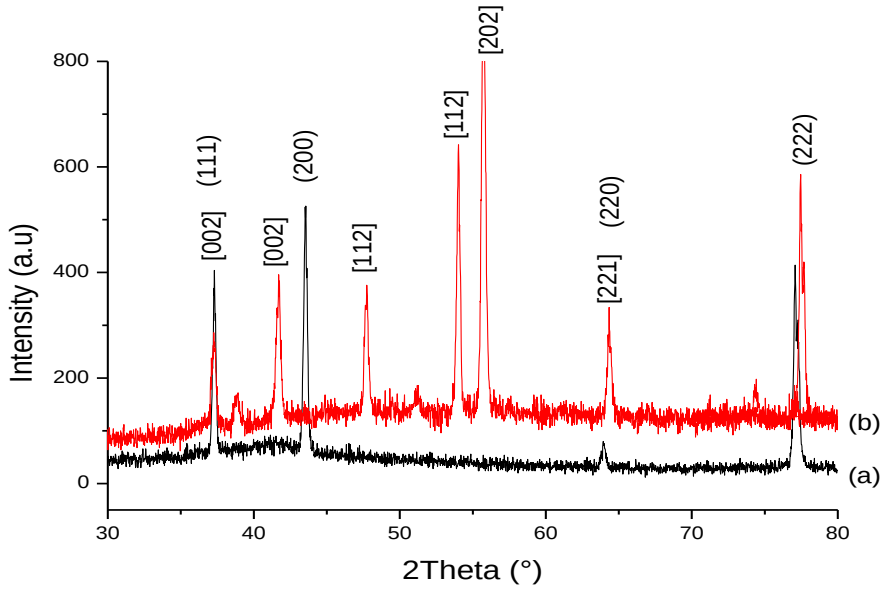

Figure 3.12: XRD patterns of TOP (a) and OLA (b) capped copper oxide nanoparticles.

Many living microorganisms such as antibacteria and fungi copy and resemble the antimicrobial agents and therefore create a resistant strain towards these antimicrobial agents. The morphologies of the antimicrobial agents such as nanoparticles play a crucial role in inhibition of the living microorganisms. Each shape of of nanoparticles targets a certain type of living organisms. Therefore, a wide variety of morphologies of nanoparticles is of interest because they will enable

different types of bacterial and fungi to be inhibited and these microbials will take time to copy and resemble these nanoparticles, thus increasing their effectiveness. So the wide variety of morphologies of the OLA-capped nanoparticles would be advantageous to inhibit the growth of different types of living microorganisms. Therefore, OLA was used to optimise other parameters that were used to synthesize nanoparticles that were applied for antimicrobial study. The properties show that the phosphine based capping molecule have lesser controlled interaction of particle growth compared to the amine based oleylamine.

3.3. Synthesis of copper chalcogenide nanoparticles using different precursor concentration ratios in OLA

The effect of precursor concentration on the synthesis of OLA-capped copper chalcogenides nanoparticles was investigated by varying copper and urea or selenium or sulphur concentration ratios of 1:2, 2:1, and 1:1 at 220 °C for 30 min. To understand the optical properties of the synthesized nanoparticles, their absorption and emission curves were studied with UV/Vis and photoluminescence spectroscopy and their morphology was studied with TEM and XRD.

3.3.1. The effect of precursor concentration ratio on the synthesis of copper selenide nanoparticles

(a) Optical properties of copper selenide nanoparticles

Figure 3.13 shows absorption spectra of copper selenide nanoparticles synthesized with different precursor concentration ratios. The extracted optical parameters of these materials are listed in Table 3.4.

The absorbance band edges of the materials synthesized from 1:2, 2:1, and 1:1 concentration ratios of copper to selenium are estimated at 687 nm, 539 nm and 513 nm respectively. The absorption spectra revealed that the material synthesized at 1:1 concentration ratio is blue shifted from those synthesized at 1:2 and 2:1 concentration ratios. This predicts that 1:1 concentration ratio should favor smaller particles than the other two materials.

Table 3.4: Optical parameters of copper selenide nanoparticles synthesized using (1:2), (2:1) and (1:1) precursor concentration

Precursor concentration ratio	Band edge (nm: eV)	Emission peak (nm)	FWHM (nm)
1:2	678(1.8)	581	67
2:1	539(2.3)	462	86
1:1	513(2.4)	434	47

When one of the precursor concentrations was increased, the band edges of the corresponding materials also increased to a higher wavelength. This is an indication of particle size increment as the precursor concentration ratio was increased. This is attributed to high concentration of precursor present in the system creating high force of attraction between copper and selenide molecules resulting agglomeration of particles hence large particles are observed (Safekordi *et al.* 2011) elucidated. The material synthesized at 1:1 concentration ratio gave a different absorption curve, compared to the other two materials synthesized at 1:2 and 2:1 ratio which gave an unusual absorption bands with a structure that resembled Covellite phase as reported by Zhang *et al.* (2008), Wu *et al*. (2008) and Roy *et al*. (2007). The material synthesized at 1:1 ratio produced a narrow absorption band whereas the two materials synthesized at 1:2 and 2:1 ratio produced a broad absorption peak. This suggests that the material synthesized at 1:1 ratio should have different optical characteristics compared to other two materials. The emission spectra corresponding to the three materials are depicted on Figure 3.14. The maximum emission peaks of the material synthesized at 1:2, 2:1 and 1:1 ratios were observed at 581, 462, and 434 nm, respectively. The emission peaks of these materials are blue shifted from their absorption peaks resulting in anti-stokes shift. The phenomenon of the anti-stokes shift was observed when the effect of capping molecule was investigated and discussed. The emission peak of the material synthesized at 1:1 concentration ratio was blue shifted from the other two materials, followed by that prepared at 2:1 concentration ratio. The material synthesized at 1:1 and 1:2 concentration ratio produced a narrow emission peaks with FWHM of 67 nm and 47 nm, respectively. These narrow emission peaks are indicative of monodispersed nanoparticles. Polydispersed particles could be predicted from synthesis using 2:1 concentration ratio due to a broad emission peak with FWHM of 86 nm.

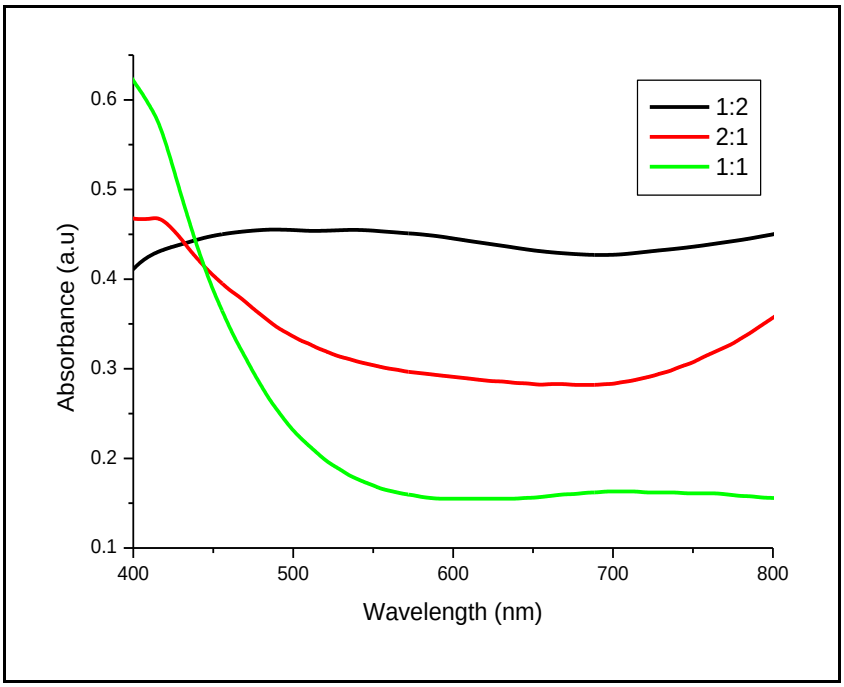

Figure 3.13: Absorption spectra of copper selenide nanoparticles synthesized using (1:2), (2:1) and (1:1) precursor concentration ratios in OLA for 30 min at 220 ºC.

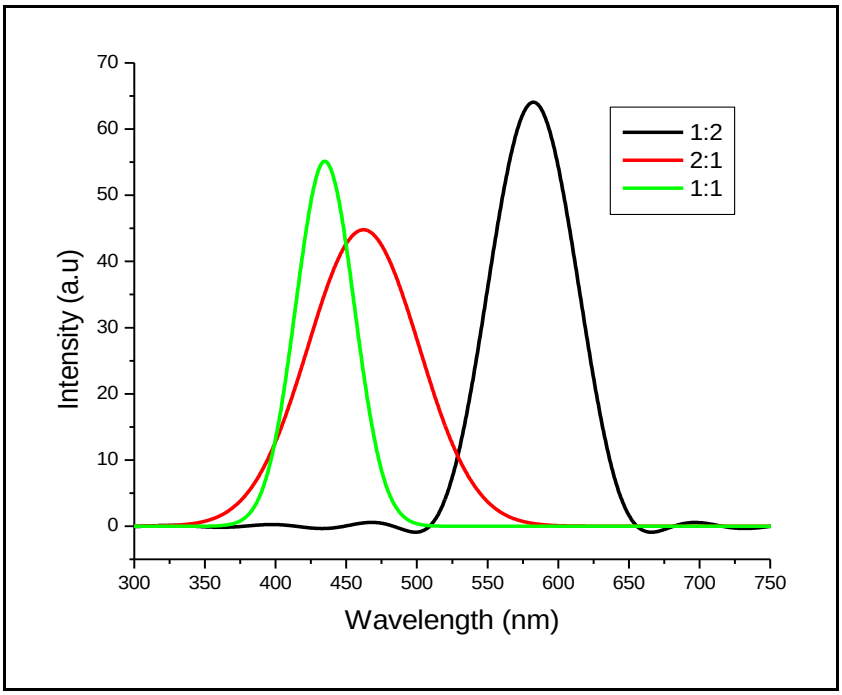

Figure 3.14: Emission spectra of copper selenide nanoparticles synthesized using (1:2), (2:1) and (1:1) precursor concentration ratios in OLA for 30 min at 220 ºC.

(b) Morphology of the synthesized copper selenide nanoparticles

Figure 3.15 shows TEM images and the corresponding size distribution graphs for copper selenide nanomaterials synthesized using different precursor concentration ratios. The size histograms of materials prepared at 1:2 and 2:1 are not shown because the two materials produced mixed morphologies. The material prepared at 1:1 concentration ratio produced smaller particles with average size of 17 nm compared to the other materials prepared at 1:2 and 2:1 concentration ratio that produced particles with average size of 792 and 72 nm, respectively. The material prepared at 1:1 concentration ratio produced small spherical structures, while the material synthesized at 1:2 concentration ratio showed hexagonal, cubes and spherical aggregates of particles. The material synthesized at 2:1 concentration ratio revealed to contain both smaller and bigger particles which include truncated triangles, cubes and sphere like structures.

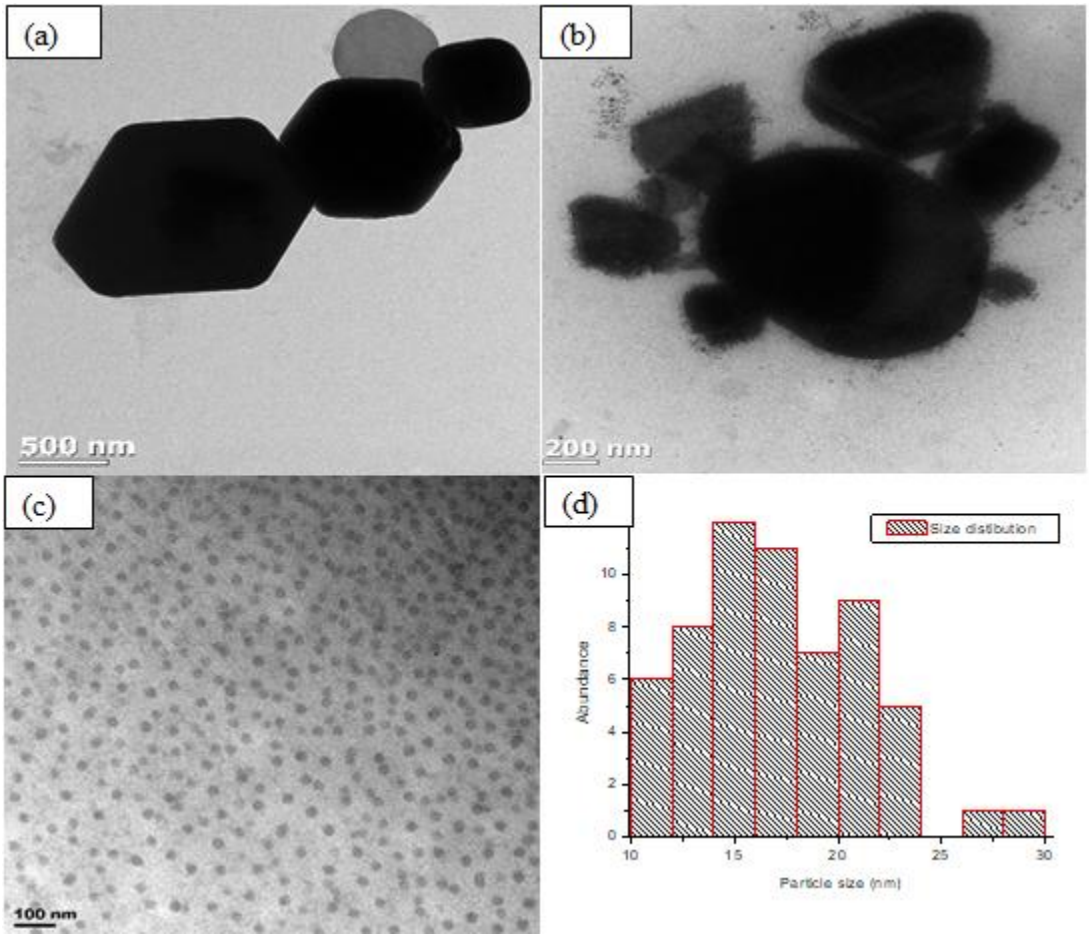

Figure 3.15: TEM images and size histogram of the synthesized copper selenide nanoparticles in OLA for 30 minutes at 220 ºC using concentration ratios 1:2 (a), 2:1 (b) and 1:1 (c & d)

Different particle sizes found in material prepared at 2:1 are in perfect agreement with its broader emission peak that predicted a polydispersed particles, particles produced by 1:1 concentration ratio also corroborates the narrow emission peak of its correspondence. Only four particles were observed in 1:2 concentration ratio The TEM images confirmed an increased particle size when one precursor concentration is increased. Since 1:1 concentration ratio gave best optical and structural properties, this sample was further used for crystallinity characterization using XRD. The XRD pattern of this material is depicted on Figure 3.16. The diffraction peaks confirmed that copper selenide nanoparticles were successfully synthesized with major peaks that are located at 2θ values 27°, 28°, 30°, 31°, 41°, 42°, 45°, 50°, 54°, 56°, 67°, 70°, 74°, 82°, 83°, and 88° corresponding to crystal planes (101), (102), (103), (006), (106), (008), (107), (108), (200), (203), (207), (208), (210), (216), (1014) and (218). This can be indexed to hexagonal Cu0.87Se (Klockmannite) PDF card no. 04-004-2214. The crystalline planes of the minor phase were observed at 2θ values 23°, 34°, 36°, 39°, 47°, 53°, 60°, 65° and 78° indexed to (110)*, (120)*, (200)*, (002)*, (221)*, (122)*, (231)* and (312)*. The minor phase was indexed to Orthorhombic CuSe2 phase PDF card no. 04-007-2178. The impurities of unreacted selenium were observed with indexed to (210) ^ indexed to JCPDS card no. 01-086-2246. The sharpness of the diffraction peaks of this material suggests high crystallinity of particles.

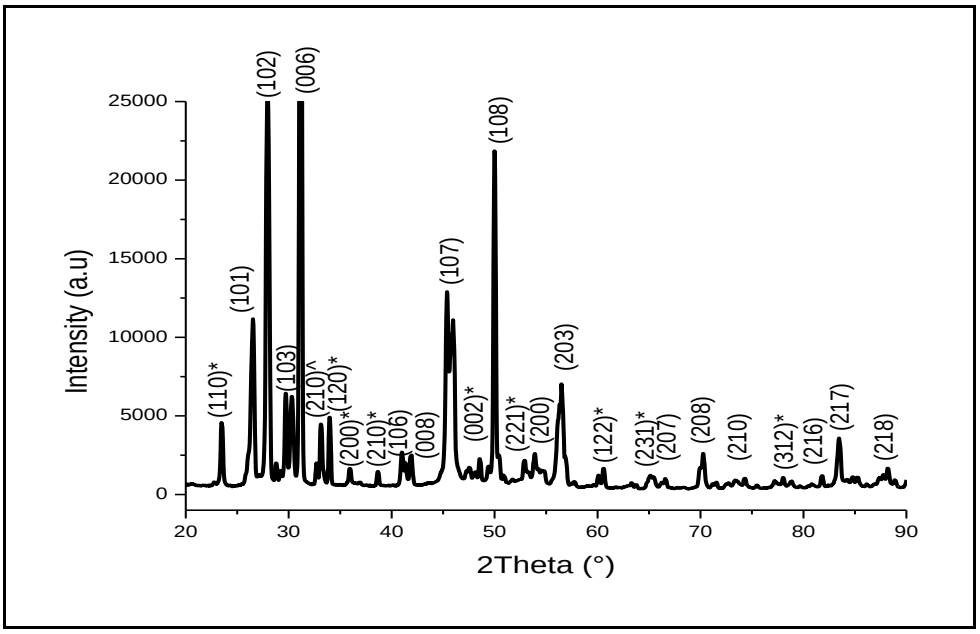

Figure 3.16: XRD pattern of copper selenide nanoparticles synthesized using (1:1) precursor concentration ratio in OLA for 30 min at 220 ºC.

3.3.2. The effect of precursor concentration ratio on the synthesis of copper sulphide nanoparticles

(a) Optical properties of copper sulphide nanoparticles

Figure 3.17 depicts the absorption spectra of copper sulphide nanomaterials synthesized using different precursor concentration ratios. The extracted optical parameters of the synthesized copper sulphide nanomaterials are listed on Table 3.5 below.

Table 3.5: Optical parameters of copper sulphide nanoparticles synthesized using (1:2), (2:1) and (1:1) at different precursor concentration

Precursor Concentration ratios	Band edge (nm: eV)	Emission peak (nm)	FWHM (nm)
1:2	798(1.55)	460	95
2:1	780(1.59)	433	39
1:1	722(1.72)	434	40

The absorption spectra of the material synthesized at 1:2, 2:1, and 1:1 concentration ratio of copper to sulphur showed band edges at 798, 780, and 722 nm, respectively. The band edges are blue shifted from their bulk counterpart (1022 nm). A degree of tailing is observed for materials synthesized at 1:2 and 2:1 and this could be indicative of agglomeration of particles. The absorption curve of the material synthesized at 1:1 concentration ratio is blue shifted from those of other two materials (1:2, 2:1). This suggests smaller particle size when the ratio of 1:1 is used. The smaller particles may be due to supersaturation that leads to a bigger change in Gibbs free energy which results in the critical size of stable nucleus and thereby many nuclei were formed. Consequently, since more number of nuclei were formed, smaller size of the final product were produced (Dajan *et al*. 2014). The emission spectra of the three materials are dipicted on Figure 3.18. The maximum intensities of the three materials are located at 460, 433, and 434 nm, respectively. This also suggests smaller particles for the material synthesized at 1:1 concentration ratio. The anti-Stokes shift photoluminescence was observed for the three materials. The same trends and findings were observed in the synthesis of copper selenide and copper oxides nanomaterials when the effect of capping molecule was investigated in this study. The materials

synthesized from 2:1 and 1:1 concentration ratios produced narrow emission peaks with FWHM of 39 nm and 40 nm, respectively. The reduced broadness of the emission peak can be attributed to a monodispersed distribution of particles. The materials synthesized at 1:2 produced a broader emission peak with a FWHM of 95 nm and this predicts a polydispersed distribution or different morphologies of particles.

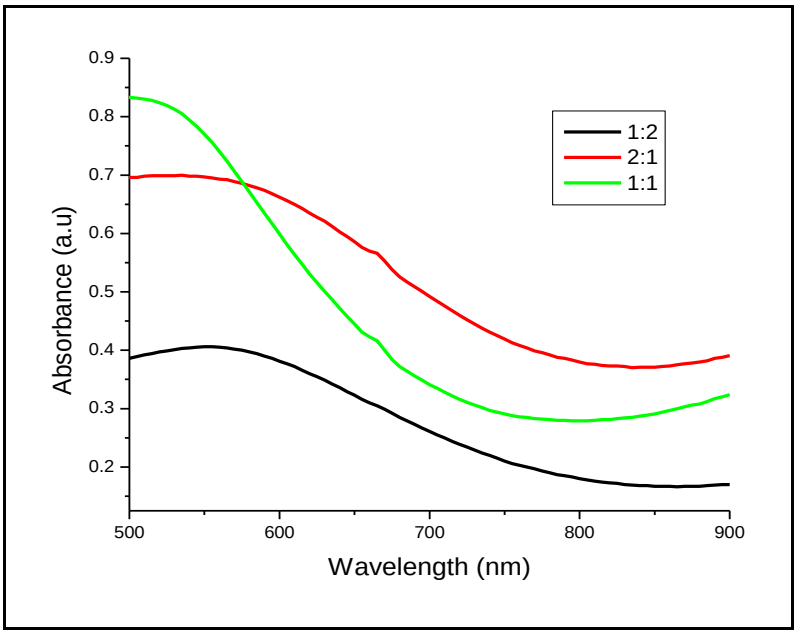

Figure 3.17: Absorption spectra of copper sulphide nanoparticles synthesized using (1:2), (2:1) and (1:1) precursor concentration ratios in OLA for 30 min at 220 ºC.

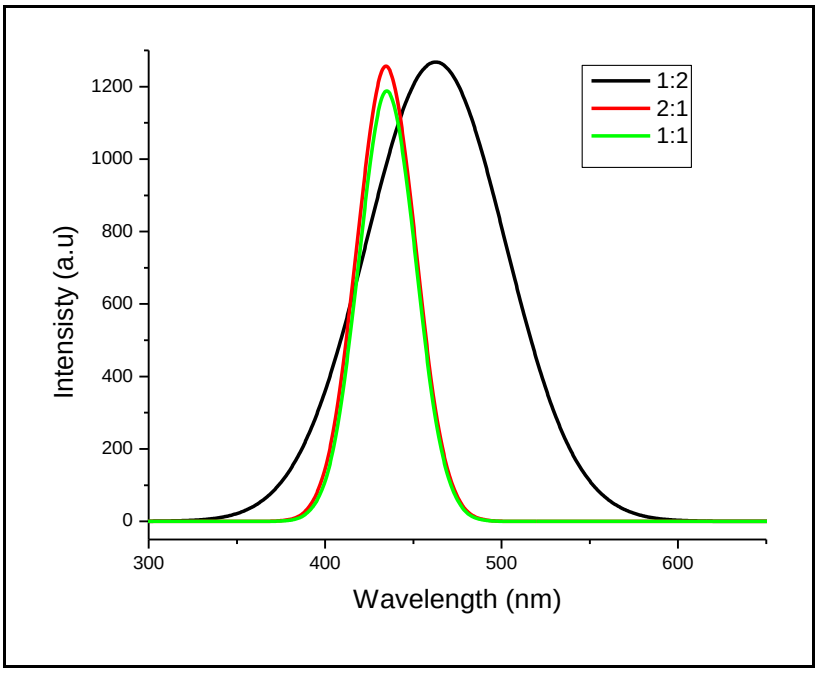

Figure 3.18: Emission spectra of copper sulphide nanoparticles synthesized using (1:2), (2:1) and (1:1) precursor concentration ratios in OLA for 30 min at 220 ºC.

(b) Morphology of the synthesized copper sulphide nanoparticles

The TEM images of the synthesized copper sulphide nanoparticles are depicted on Figure 3.19. TEM images revealed that the materials synthesized at 1:2 and 2:1 concentrtion ratios are composed of mixed morphologies which are hexagonals, truncated triangles and sphere like structures that are very big in size. The material synthesized at 1:1 produced very small semi-sphere like structure that are well passivised. The size distribution graphs of the materials synthesized at 1;1 and 2:1 corroborate their coresponding narrow emission peaks which predicted a monodispersed distribution. The materials synthesized at 1:2 concentrtion ratio produced both small and big particles, hence a broader emission peak was observed. The increased particle size on the material synthesized at concentrtion ratios of 1:2 and 2:1could be attributed to an increased concentration of a precursor in a fixed temperature. The decreased particle size of 1:1 material can be attributed to decreased amount of surfactant available for the stabilization of the precursors resulting to supersaturation. Therefore more nuclei were formed and subsequently, smaller particles were produced. Demortiere *et al*. (2011) reported similar findings when size-dependant properties of magnetic iron oxide nanocrystals were investigated. This phenomenon was observed in copper selenide nanomaterials that were synthesized under the conditions.

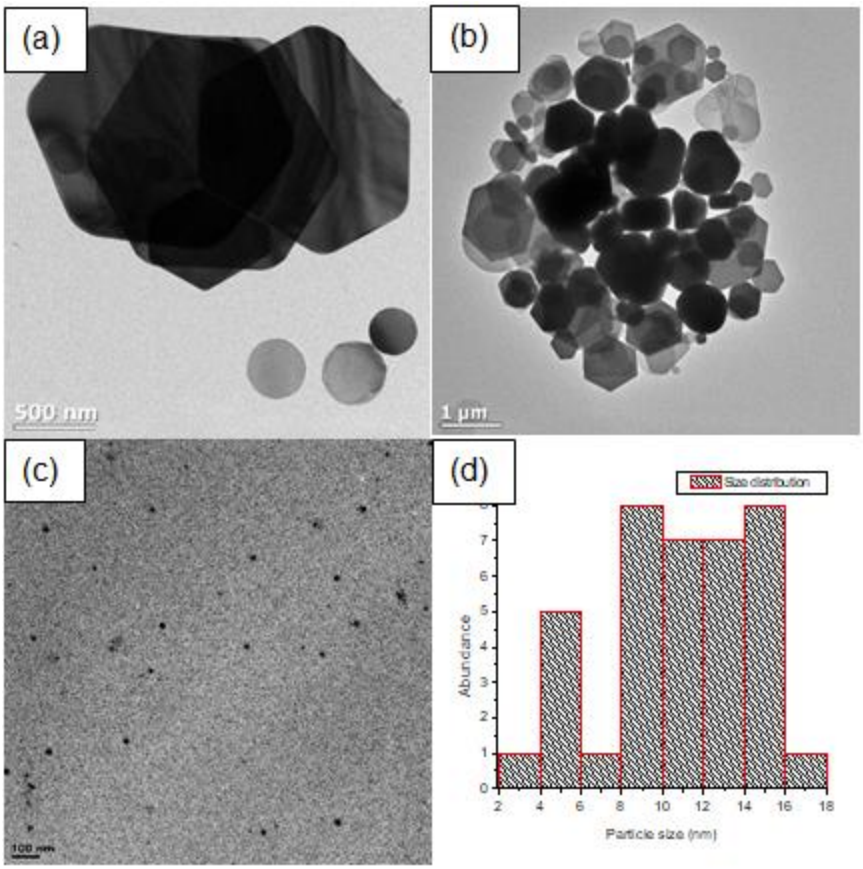

Figure 3.19: TEM images and size histogram of the synthesized copper sulphide nanoparticles in OLA for 30 min at 220 ºC using concentration ratios 1:2 (a); 2:1 (b) and 1:1 (c & d).

Since the material synthesized at 1:1 concentration ratio possessed better optical and structural properties, this material was further investigated by XRD as shown in Figure 3.20. The diffractogram patterns cofirmed that copper sulphide nanoparticles were successfully synthesized with mainly rhombohedral Cu_9S_5 (Digenite) phase which is indexed to PDF card no. 00-047-1748. The crystalline planes for 2θ values were found approximately at 26°, 28°, 29°, 32°, 36°, 37°, 42°, 46°, 51°, 55°, 57° 64°, 67°, 72°, 74° and 85° which were assigned to (101), (0015), (107), (1010), (1013), (1014), (0117), (0120) (0123), (1115), (0030), (0033), (2020), (1127),(211) and (1040) crystal planes, respectively. Copper sulphide nanoparticles also produced few impurities of covellite CuS phase PDF card no. 04-001-1461 with crystalline planes that are located at 2θ values 48°and 59° corresponding to crystal planes (110)* and (202)* respectively. The increase in diffractogram intensities predicts better quality of copper sulphide nanoparticles.

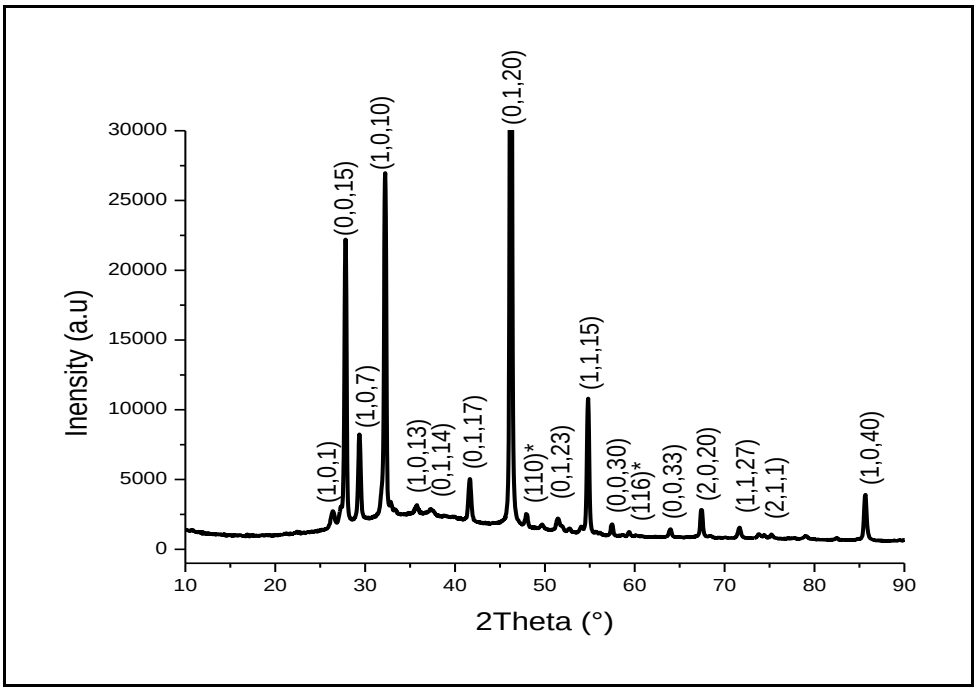

Figure 3.20: XRD pattern of copper sulphide nanoparticles synthesized using (1:1) precursor concentration in OLA for 30 min at 220 ºC.

3.3.3. The effect of precursor concentration ratio on the synthesis of copper oxide nanoparticles

(a) Optical properties of copper oxide nanoparticles

Figure 3.21 depicts the absorption spectra of the synthesized copper oxide nanomaterials and their extracted optical parameters are listed on Table 3.6.

Table 3.6: Optical parameters of copper oxide nanoparticles synthesized using (1:2), (2:1) and (1:1) precursor concentration ratios

Precursor concentration (ratio)	Band edge (nm: eV)	Emission peak (nm)	FWHM (nm)
1:2	854(1.45)	581	96
2:1	828(1.50)	436	94
1:1	830(1.49)	462	54

The copper oxide nanomaterials synthesized at 1:2, 2:1 and 1:1 precursor concentration ratio had their band edges at 854, 828, and 830 nm, respectively. These band edges are blue shifted with respect to their bulk counterpart band gap of 1033 nm. The band edge of the material synthesized at 2:1 concentration ratio is blue shifted from those of samples prepared at 1:2 and 1:1concentration ratios. This is an indication of smaller particles that are produced by the material synthesized at 2:1. The increase in band edges with the decrease of metal precursor concentration indicates size increment of particles. In all the three materials, their absorption curves are identical with a broad absorption band and a degree of tailing which could be attributed to agglomeration or closely packed particles. The broad absorption band could be attributed to the self-assembly of the nanoparticles as Oluwafemi *et al*. (2009) and Vanaja *et al*. (2013) deduced. The identical absorption curves suggest similar optical properties for the three materials. The maximum emission spectra of the three materials are depicted in Figure 3.22 below. The emission intensities of the material synthesized at 1:2, 2:1 and 1:1 concentration ratios were observed at 581, 436, and 460 nm, respectively. The emission peaks of the three materials followed the same trend as their absorption spectra. The emission peak of the material synthesized at 1:2 concentration ratio are red-shifted from the other two materials followed by the material synthesized at 1:1 concentration ratio. The wavelength of the emission peaks increased with the decrease in metal precursor concentration, suggesting bigger particle sizes for the material synthesized at 1:2. A large anti-stokes shift photoluminescence was observed in all three materials. The material synthesized at 2:1 produced a narrow emission peak with a FWHM of 54 nm, predicting monodispersed particles. The material synthesized at 1:2 and 1:1 produced broader emission peak maxima with FWHM of 96 nm and 94 nm, respectively. This could be attributed to a slightly polydispersed particle distribution.

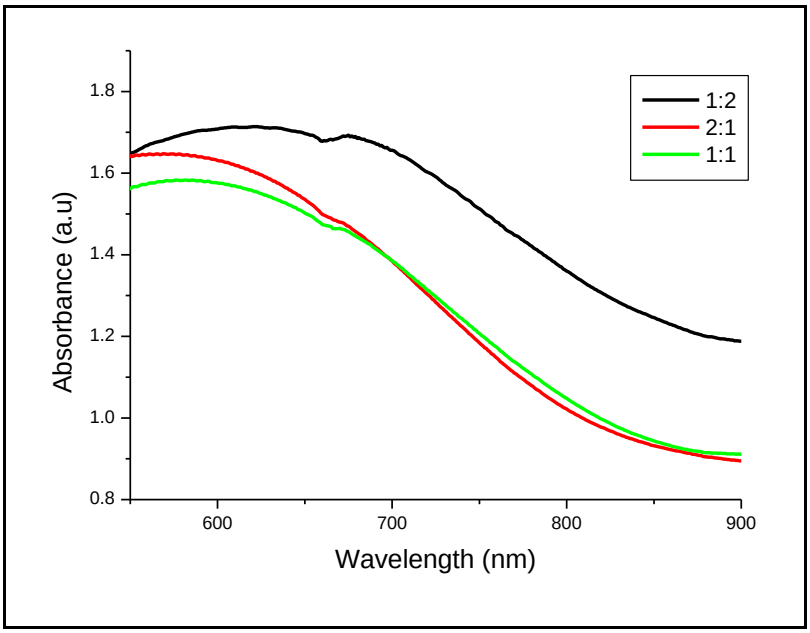

Figure 3.21: Absorption spectra of copper oxide nanoparticles synthesized using (1:2), (2:1) and (1:1) precursor concentration ratios in OLA for 30 min at 220 ºC.

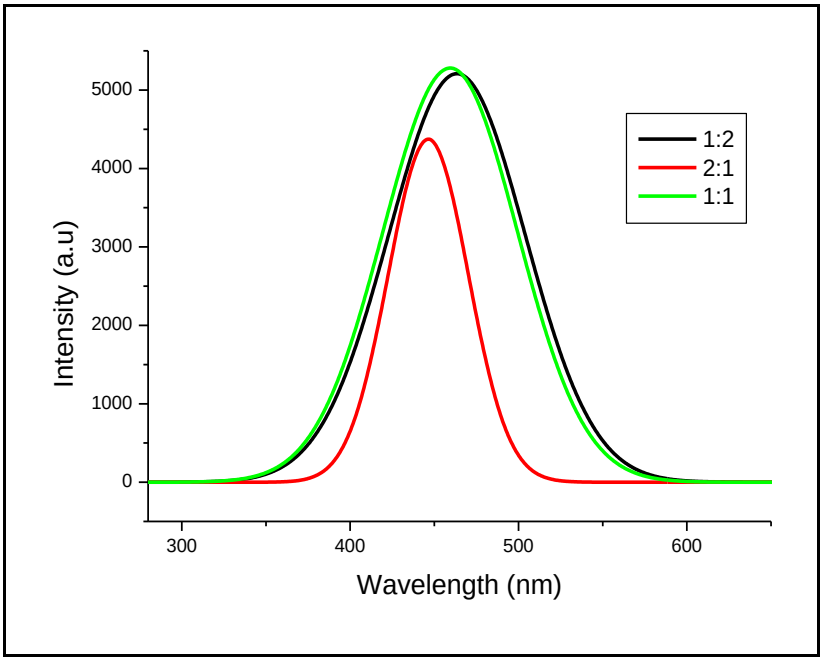

Figure 3.22: Emission spectra of copper oxide nanoparticles synthesized using (1:2), (2:1) and (1:1) precursor concentration ratios in OLA for 30 min at 220 ºC.

(b) Morphology of the synthesized copper oxide nanoparticles

TEM images of copper oxide nanomaterials synthesized with different precursor concentration ratios are shown on Figure 3.23 with their corresponding size distribution. As predicted by optical properties, the material synthesized at 2:1 concentration ratio produced the smallest particle with an average size of 2.10 nm. This was followed by the material synthesized at 1:1 concentration ratio which produced particles with an average size of 3.33 nm. The material synthesized at 1:2 concentration ratio produced bigger particles compared to the other two materials (2:1 and 1:1) with an average size of 5.73 nm. The particles of all three materials are closely packed hence a degree of tailing is observed for their absorption curve and this could be attributed to their small sizes which produce high surface energy and thereby increase the forces of attraction between particles. The material synthesized at 2:1 ratio produced a narrow size distribution of particles as predicted by its corresponding emission peak with a FWHM of 54 nm. All the three particles produced sphere like structures that are monodispersed even though FWHM of the material synthesized at 1:2 and 1:1 precursor concentration ratio suggested otherwise.

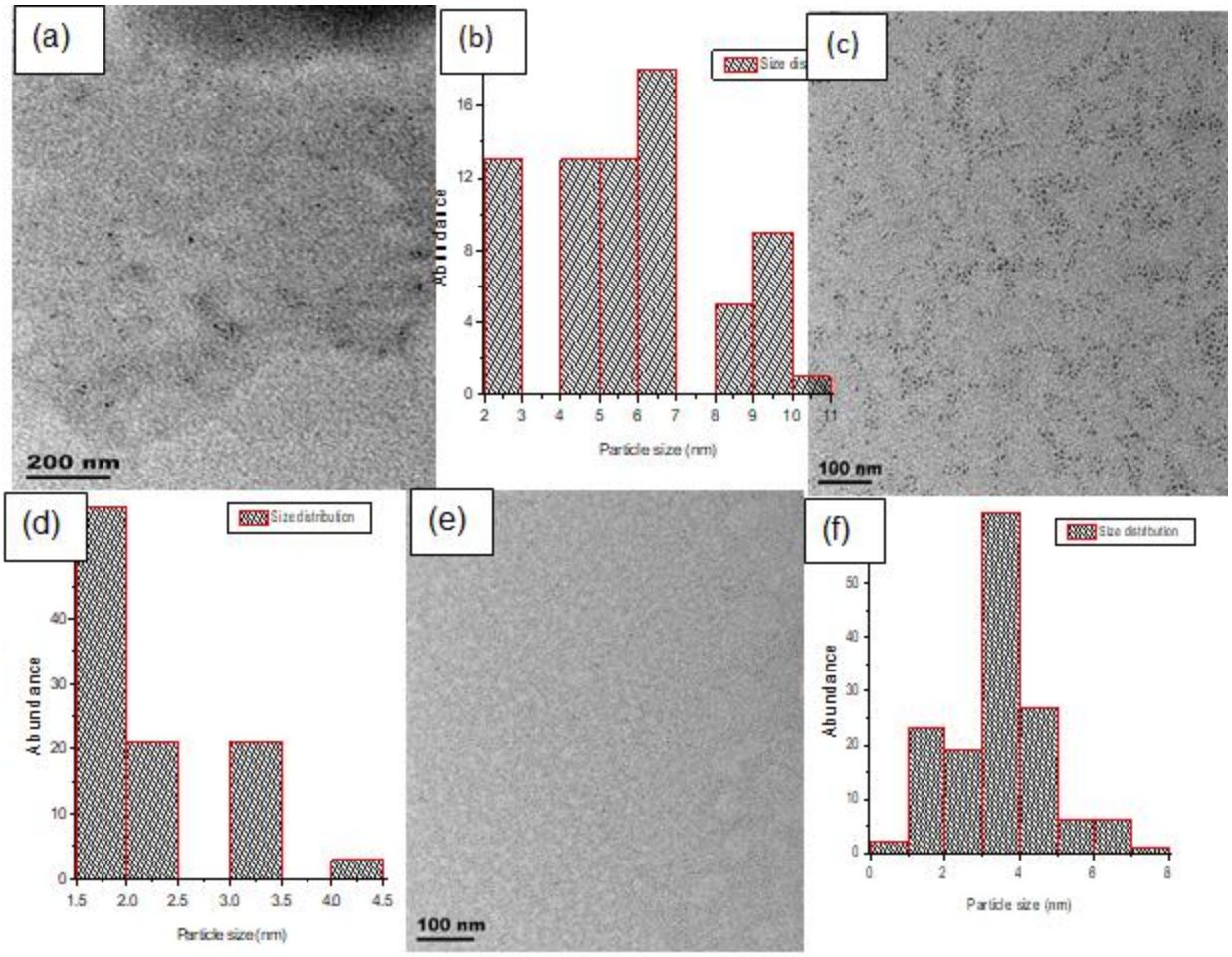

Figure 3.23: TEM images and size histograms of the synthesized copper oxide nanoparticles in OLA for 30 min at 220 ºC using concentration ratios 1:2 (a & b); 2;1 (c & d) and 1:1 (e & f), respectively.

Figure 3.24 shows XRD results of copper oxide nanomaterials synthesized at 1:2, 2:1 and 1:1 precursor concentration ratios. The properties of the materials synthesized at 1:2 ratio precursor concentration were found at Cubic Cu_2O phase indexed to PDF card no. 77-0199. Corresponding to crystal planes (111), (200), (220), and (222) are 2θ values 37°, 44°, 64°, and 78° respectively. The material synthesized at 2:1 concentration ratio exhibited properties of monoclinic CuO phase with diffractions located at 2θ values 33°, 36°, 40°, 46°, 48°, 51°, 53°, 57°, 61°, 66°, 67°, and 78° corresponding to crystal planes (110), (002), (111), (112), (202), (112), (020), (113), (022), (113), and (222). These are indexed to PDF card no. 45-0937. The material synthesized at 1:1 concentration ratio showed a mixture of the two phases found in Cubic Cu_2O

phase and Monoclinic CuO phase. CuO which is the major phase produced diffractions at 2θ values 37°, 39°, 42°, 47°, 54°, and 56° that are indexed to (002), (111), (200), (202), (020), and (021) which are indexed to PDF no. 48-1548. The minor phase Cu_2O produced diffractions at 2θ values 64° and 78° corresponding to crystal planes (220) and (222) which are indexed to JCPDS no. 77-0199. These results indicate that the precursor concentration ratio showed an effect on the size, the shape of particles as well as the phase composition of material of the synthesized nanoparticles.

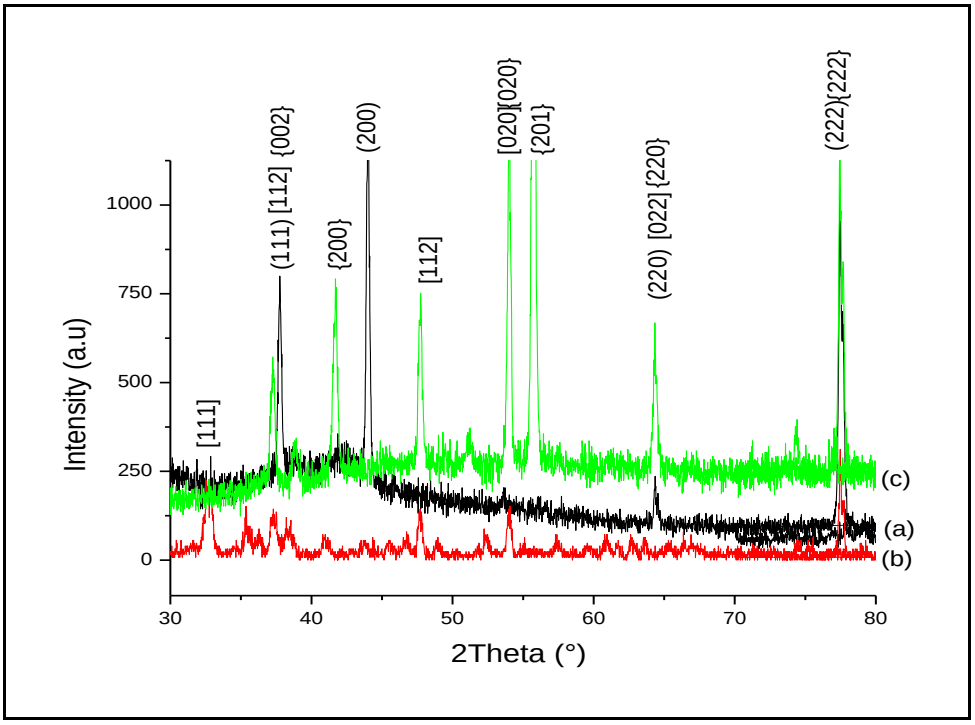

Figure 3.24: XRD patterns of copper oxide nanoparticles synthesized using 1:2 (a); 2:1 (b); 1:1 (c) precursor concentration ratios in OLA for 30 min at 220 ºC.

Copper oxide revealed a different phenomenon compared to copper selenide and copper sulphide when the effect of precursor concentration ratio was investigated. Optimum precursor concentration ratio of copper selenide and copper sulphide were found to be 1:1 ratio whereas copper oxide nanocrystals revealed its optimum precursor concentration ratio in 2:1 based on the particle size they produced which would be more suitable for antimicrobial study. Nonetheless, since the performance of the three copper chalcogenides nanocrystals were to be compared at the end of the study, same parameter conditions were employed for their synthesis and therefore, the precursor concentration ratio 1:1 was used for the investigation of other parameters.

3.4. The effect of time on the synthesis of copper chalcogenides nanoparticles

The reaction times for the synthesis of oleylamine-capped copper selenide, copper sulphide and copper oxide nanoparticles were investigated. Time was varied to 15, 30, 45 and 60 minutes while other parameters such as temperature (220 °C), and the concentration of the precursors (1:1 ratio) were kept constant. Copper chalcogenides nanoparticles synthesized under these conditions were characterized by various techniques including UV/Vis, PL spectrophotometry, TEM and XRD.

3.4.1. The effect of time on the synthesis of copper selenide nanoparticles

(a) Optical properties of copper selenide nanoparticles

The UV/Vis absorption spectra of copper selenide nanoparticles synthesized at 15, 30, 45, and 60 minutes are shown in Figure 3.25. Table 3.7 shows the extracted optical parameters.

Table 3.7: Optical parameters of copper selenide nanoparticles synthesized for 15, 30, 45, and 60 min

Time (min)	Band edge (nm: eV)	Emission peak (nm)	FWHM (nm)
15	766(1.62)	505	61
30	506(2.45)	365	55
45	587(2.11)	417	102
60	674(1.84)	457	53

The absorption band edges of these materials prepared at 15, 30, 45 and 60 minutes were observed at 766, 506, 587 and 674 nm, respectively. All band edges were blue shifted from that of the bulk material band gap (1180 nm). When the reaction time was increased from 15 minutes to 30, 45 then 60 minutes the band edges also increased to a higher wavelength. The band edge of the material synthesized at 30 minutes indicated a blue shift compared to other three materials prepared at 15, 45 and 60 minutes. This suggests that 30 minutes synthesis gave smaller particle size than all the other times investigated. The absorption curve of the material is also different from the rest of the three materials, suggesting that the optical properties of this material would differ from the rest of the three materials. The band edge of the material synthesized for 15 minutes is red shifted from those of other materials that were synthesized for longer period time. This higher wavelength

predicts bigger diameter of particles for the shortest time of 15 minutes. When the reaction time was increased from 15 minutes to 30, 45 and 60 minutes, the band edges increased to higher wavelength predicting an increase in particle size. This agrees with what was reported by Kalenga *et al*. (2012) who observed particle size increment with reaction time through Ostwald ripening. The emission spectra of the four different materials are depicted in Figure 3.26. The four materials produced their maximum intensity at 505, 365, 417, and 457 nm, respectively. The emission peaks of these materials corroborate their UV/Vis spectra by following the same trend as their absorption curve. A broad peak for the material synthesized at 45 minutes is observed with a FWHM of 102 nm and this suggests that the material is polydispersed. The emission peak of the 15 min material is also broad and red shifted from other three materials and produced high intensity. This suggests that this material should have the biggest particle size as suggested by its absorption curve. The material that was synthesized for 30 and 60 minutes gave narrower emission peaks with FWHM of 55 nm and 53 nm respectively compared to other two materials. This suggests that 30 and 60 minutes synthesis gave nanoparticles that are monodispersed. Particles prepared at 15 minutes gave an emission peak with a full width at height maximum of 61 nm predicting less monodispersed particles.

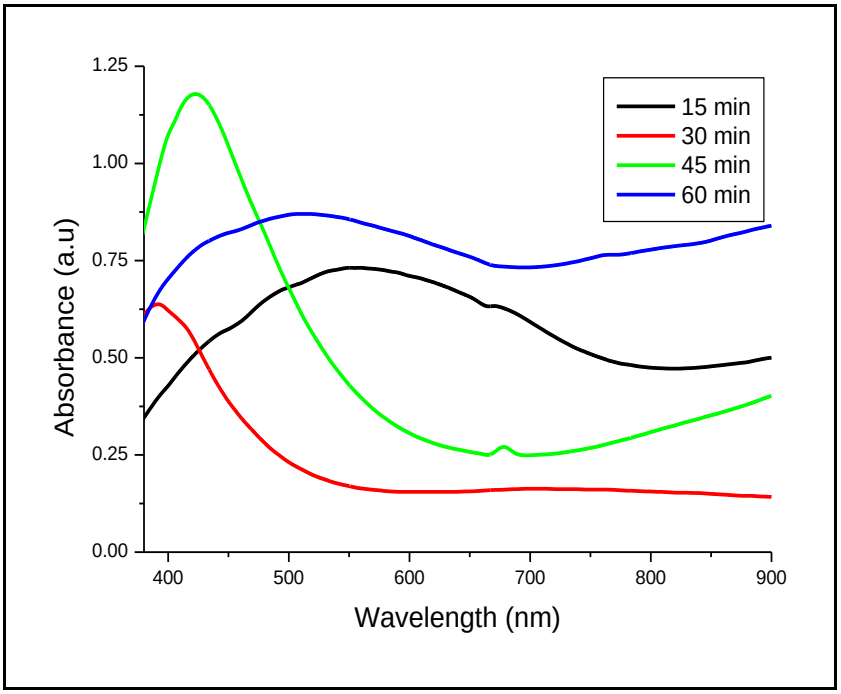

Figure 3.25: Absorption spectra of copper selenide nanoparticles synthesized for 15, 30, 45 and 60 min in OLA at 220 °C using 1:1 mole ratio of CuSe.

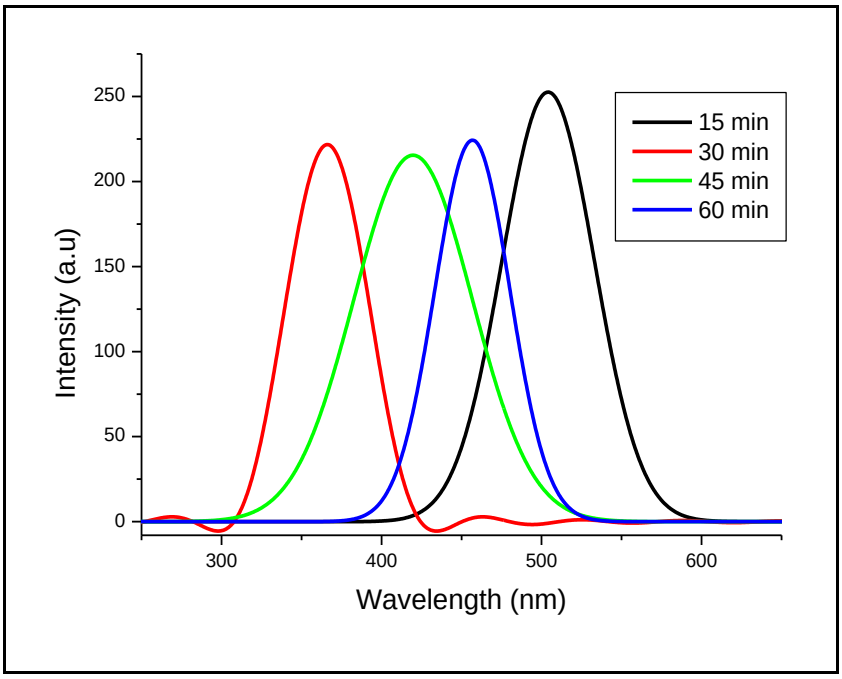

Figure 3.26: Emission spectra of copper selenide nanoparticles synthesized for 15, 30, 45, and 60 min in OLA at 220 °C using 1:1 mole ratio of CuSe.

(b) Morphology of the synthesized copper selenide nanoparticles

TEM images of copper selenide nanoparticles synthesized at different times are shown in Figure 3.27. The shortest time (15 minutes) synthesis produced particles that are highly agglomerated with no defined shapes and this corroborates its corresponding emission peak that produced high intensity. TEM image of the particles synthesized at 15 minutes suggest that this reaction time was too short for a complete nucleation. Particles that were produced at 30 minutes are sphere like structures with size ranging from 1 to 27 nm. The materials synthesized at 45 and 60 minutes produced particles with size ranging from 3 to 180 nm and 10 to 1200 nm respectively that are mixed morphology. When the time of the reaction was increased to 45 minutes, the spherical like particles that were observed at 30 min transformed into hexagonal structure, truncated triangles, prisms, and cubes structures indicating a continuous growth of particles. This size and morphology evolution could be due to Ostwald ripening process.

Different particle sizes and particle shapes that are produced by material synthesized at 45 minutes are in good agreement with its FWHM that suggested a polydispersed material. When the reaction time was increased further to 60 minutes, the evolution of particle shapes stopped but the particles

continued to grow bigger. TEM images revealed that indeed 30 minutes material has the smallest particles compared to all other three materials. The particle sizes corroborate the absorption and emission spectra of the four materials which suggested a particle size increase with the increase of reaction time from 30 minutes to 60 minutes. A monodispersed population that was observed in nanoparticles that were produced at 30 minutes is consistent with its narrower emission peak. The materials synthesized at 30 and 45 minutes gave better optical and structural properties. Their absorption line curves were blue shifted from the material synthesized at 60 minutes confirming their smaller particles size in comparison to the material synthesized at 60 minutes since smaller particles are of interest in antimicrobial study. Therefore, these two materials were further characterized to understand their crystallinity and phase composition.

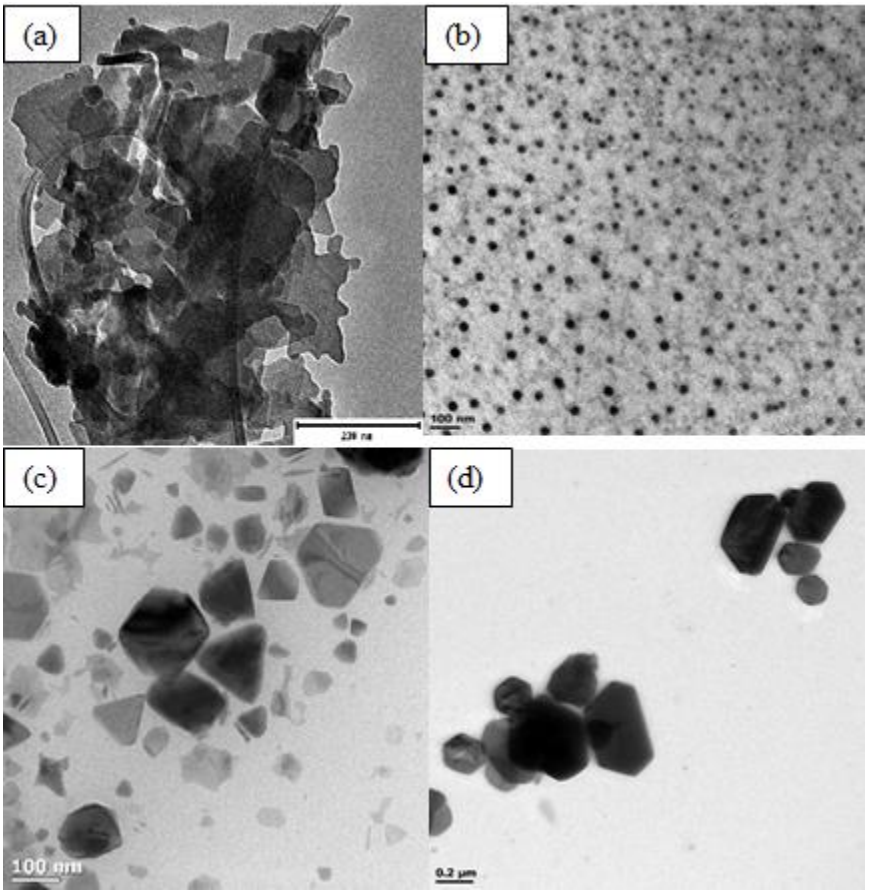

Figure 3.27: TEM images of copper selenide nanoparticles synthesized for 15 min (a); 30 min (b); 45 min (c) and 60 min (d) in OLA at 220 °C using 1:1 mole ratio of CuSe.

The XRD patterns of copper selenide nanocrystals synthesized for 30 and 45 minutes are displayed in Figure 3.28. The XRD diffraction pattern confirmed that copper sulphide nanoparticles were produced in both reaction times. Both reactions produced mixture of phases. The major phase was found at hexagonal $Cu_{0.87}Se$ (Klockmannite) which is indexed to PDF card no.04-007-2214 and the minor phase was found at Orthorhombic $CuSe_2$ indexed to PDF card no.04-004-2178. The crystalline planes of the major phase are located at 2θ values 26°, 28°, 30°, 31°, 42°, 46°, 50°, 56°, 64°, 67°, 70°, 71°, 73°, 76°, 78°, 82°, 83°, 85 ° and 89° corresponding to miller indices (100), (102), (006), (020), (008), (107), (108), (203), (208), (207), (1012), (110), (211), (2010), (216), (1014), (300) and (2012). The minor phase was found at 2θ values 23°, 34°, 38°, 39°, 54°, 58°, 61°, 81° and 88° corresponding to crystalline planes (110)*, (111)*, 200*, (210)*, (131)*, (022)*, (205)*, (113)* and (421)* of Orthorhombic CuSe2. Impurities of unreacted selenium were observed and indexed to planes (110)` and (201)` with PDF card no. 01-086-2246. An unidentified impurity was also observed at 79° and denoted by +. The phase composition of the two materials proved that the reaction time does not have much effect on the stoichiometry of the synthesized nanoparticles but a huge effect on the size of the particles.

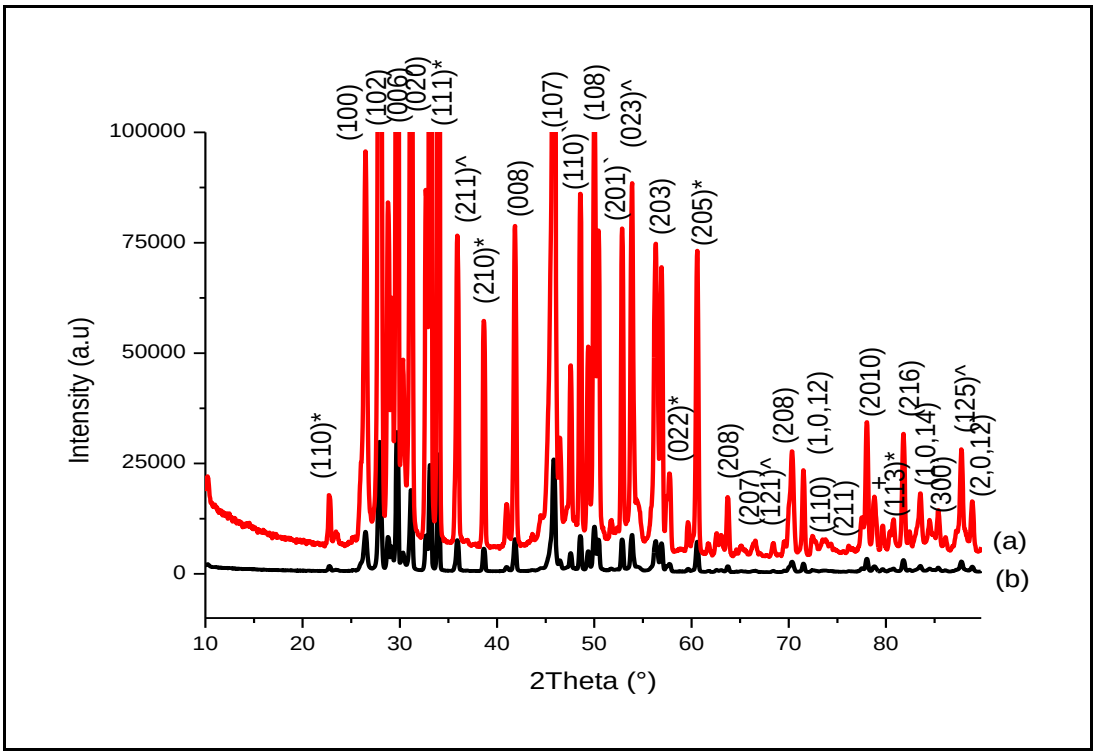

Figure 3.28: XRD patterns of copper selenide nanoparticles synthesized for (a) 30 min, (b) 45 min in OLA at 220 °C using 1:1 mole ratio of CuSe.

3.4.2. The effect of time on the synthesis of copper sulphide nanoparticles

(a) Optical properties of copper sulphide nanoparticles

The optical properties of copper sulphide nanoparticles synthesized at different reaction times were studied by Ultraviolet Visible and Photoluminescence spectroscopy. The absorption spectra of these materials are depicted on Figure 3.29 and the extracted optical parameters are assembled on Table 3.8 below.

The estimated band edges of the materials synthesized for 15, 30, 45, and 60 min are observed at 678 nm, 538 nm, 585 nm and 598 nm, respectively. The band edges of all four samples are blue shifted from their bulk counterpart.

Table 3.8. Optical parameters of copper sulphide nanoparticles synthesized for 15, 30, 45, and 60 min

Time (min)	Band edge (nm: eV)	Emission peak (nm)	FWHM (nm)
15	678(1.80)	482	68
30	538(2.30)	468	72
45	585(2.12)	471	91
60	598(2.07)	482	95

The material synthesized for 15 minutes was red shifted from the other three materials synthesized for longer time. This red shift predicts bigger particle size compared to other three materials. When the reaction time increased from 15, 30, 45 to 60 minutes, the band edges also increased to a higher wavelength and this is an indication of an increase in particle size. The increase in particle sizes with the increase of reaction time can be attributed to the Ostwald ripening of the nuclei. This trend was also observed in copper selenide nanocrystals when the effect of reaction time was investigated. The four samples produced two different types of absorption curves predicting different optical properties. The materials prepared at times of 30 and 60 minutes resembled a chalcocite phase characteristic while 15 minutes and 45 minutes resembled a Covellite phase characteristics as predicted by Ravi *et al*. (2009), Moloto *et al*. (2012) and Cheon *et al*. (2006) in their investigations. The emission spectra of the four materials are presented in Figure 3.30. The maximum emission intensities of the four materials are located at 482, 468, 471 and 482 nm, respectively. The emission spectra followed the same trend as their absorption spectra and this behavior was also observed on copper selenide nanoparticles that have been reported on the previous section of this study. Nanoparticles synthesized at 15 and 30 minutes gave narrower emission peaks with FWHM of 68 and 72 nm, respectively. This suggests a narrow size distribution compared to the other two materials. The nanomaterials synthesized at 45 and 60 minutes gave broader emission peaks with a calculated FWHM of 91 and 95 nm, respectively which suggest a broader size distribution.

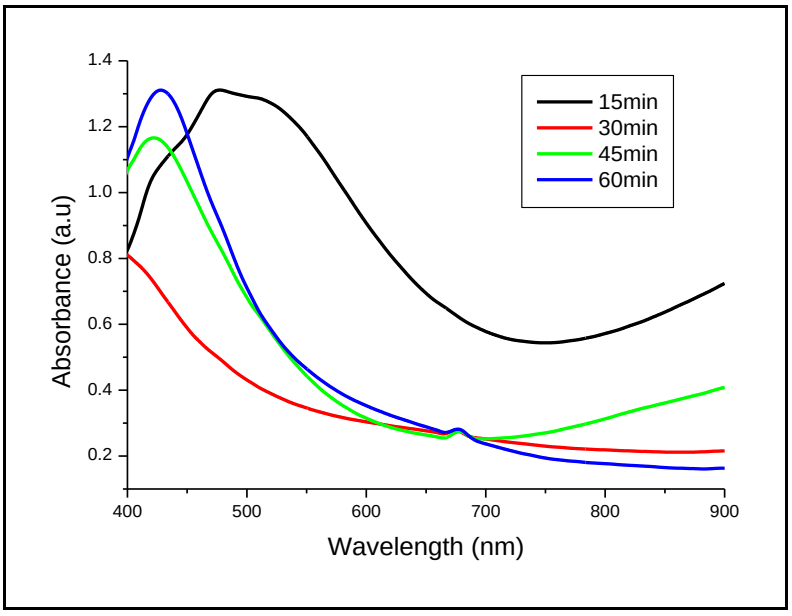

Figure 3.29: Absorption spectra of copper sulphide nanoparticles synthesized for 15 min, 30 min, 45 min, and 60 min in OLA at 220°C using 1:1 mole ratio of CuS.

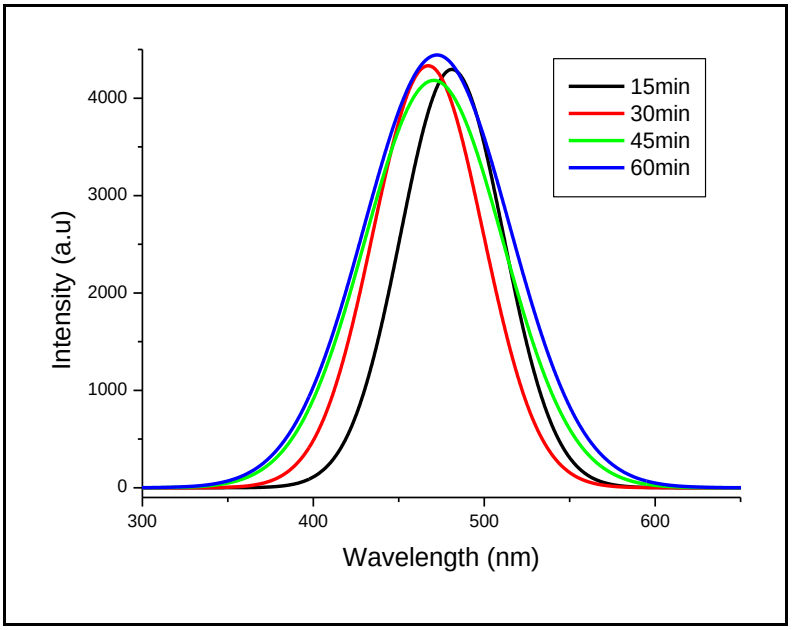

Figure 3.30: Emission spectra of copper sulphide nanoparticles synthesized for 15, 30, 45, and 60 min in OLA at 220 °C using 1:1 mole ratio of CuS.

(b) Morphology of the synthesized copper sulphide nanoparticles

The morphology of the synthesized copper sulphide nanoparticles was studied by TEM and their images are presented on Figure 3.31 together with their size distribution graphs. The size distribution graphs of the materials synthesized for 15 minutes and 60 minutes are not displayed due to mixed morphologies of particles they produced. 15, 30, 45 and 60 minutes reaction times produced particles in size range (2-108 nm), (1-18 nm), (2-38 nm) and (5-58 nm), respectively. At the beginning of the reaction stage (15 minutes), bigger particles that are mixed morphology were obtained. The mixed mophorlogies included truncated triangles, cubes like structures and spheres that are overlapping resulting in high agglomeration.

When the reaction time was increased to 30, 45 and 60 minutes, a trend of size increase with reaction time was observed. This trend corroborates what was predicted by UV/Vis absorption spectroscopy. The material syntheiszed at 30 minutes produced the smallest particle size than other three materials with shapes that are almost spherical. The material synthesized at 45 minutes also produced small particles but with some smaller clusters indicating that these particles were starting to dissolve in one another and forming big particles as Sibokoza *et al*. (2017) and Sibiya *et al.* (2014) deduced. This was confirmed by the material synthesized for 60 minutes which revealed that the particles were becoming bigger with time through Ostwald repineng process and the evolution of shapes was also observed. The material that was synthesized for 60 minutes also revealed a mixed morphology shapes with hexagonals dominant. This revealed that with longer reaction time there is evolution of particle shapes, the shapes of the particles become more defined and well passivised. This was observed in the synthesis of copper selenide nanoparticles as well. No agglomertion was observed in nanomaterials that were synthesized for longer reaction time and this confirmed a well distribution of particles that was suggested by their optical properties. High agglomeration was observed in material that was synthesized for 15 minutes. The material synthesized for 30 and 45 minutes produced better optical and structural properties in terms of UV/Vis and TEM than other two materials and therefore, were further studied for their crystallinity and phase composition using XRD.

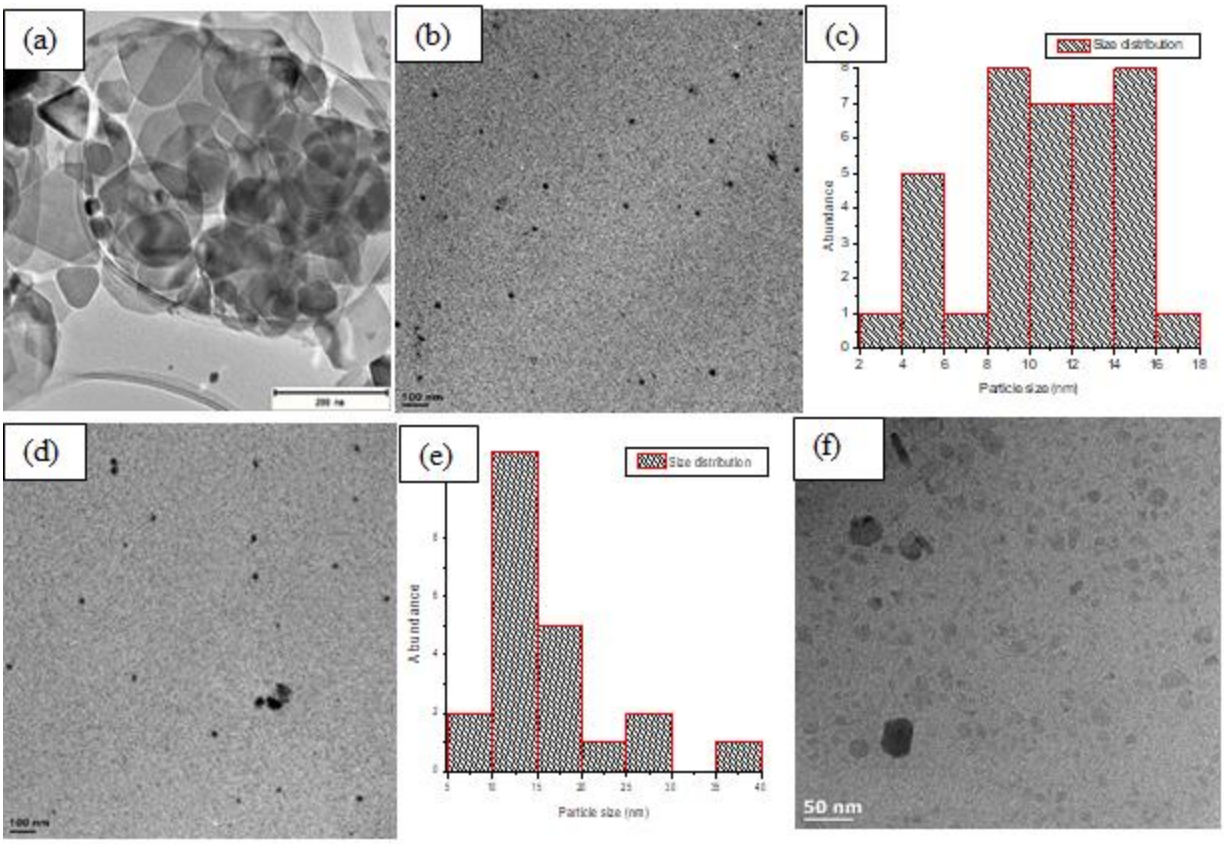

Figure 3.31: TEM images and size histograms of copper sulphide nanoparticles synthesized for 15 min (a); 30 min (b) & (c); 45 min (d) & (e) and 60 min (f) in OLA at 220 °C using 1:1 mole ratio of CuS.

Figure 3.32 displayed the XRD patterns of the material synthesized for 30 and 45 minutes. The diffraction peaks confirmed that copper sulphide were succesfully synthesized in both reaction times. The XRD pattern clearly support that the material synthesized for 30 min and 45 minutes were mainly found in Rhombohedral Cu_9S_5 phase with minnor impurities of Covellite phase. The diffraction patterns of the major phase which was indexed to Rhombohedral Cu_9S_5 (Digenite) phase PDF card no. 00-047-1748 were observed at 2θ values 26°, 28°, 29°, 32°, 36°, 37°, 41°, 46°, 50°, 51°, 55°, 57°, 64°, 67° , 72° 74°, 76° and 86° corresponding to planes (101), (0015), (107), (1010), (1013), (0114), (0117), (0120), (119), (1112), (1115), (0030), (0033), (2020), (1127), (211) and (217), respectively. The impurities of the Covellite CuS phase were indexed to PDF card no. 04-001-1461 with diffractions that were observed at 2θ values 48° and 59° corresponding to crystalline planes (112)* and (116)*, respectively. The enhanced intensity of diffraction peaks of

the material synthesized for 45 minutes predicts high crystallinity of bigger particles compared to those of 30 minutes and that is in good agreement with TEM particle sizes. The minor phase of these material is in good agreement with its absorption curve of the material synthesized for 45 minutes which suggested a Covellite phase. The mixture of phases was also observed in copper selenide nanoparticles when the effect of time was investigated. The effect of time did not affect the phase composition of the synthesized nanoparticles just like in copper selenide nanoparticles.

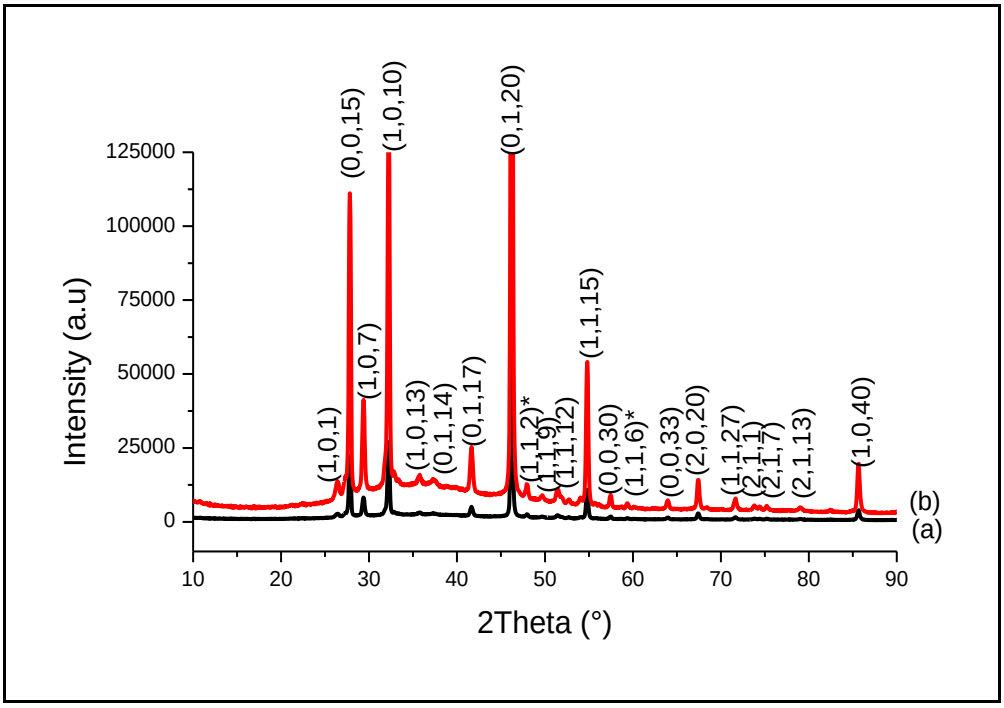

Figure 3.32: XRD patterns of copper sulphide nanoparticles synthesized for 30 min (a) and 45 min (b) in OLA at 220 °C using 1:1 mole ratio of CuS.

3.4.3. The effect of time on the synthesis of copper oxide nanoparticles

(a) Optical properties of copper oxide nanoparticles

On Figure 3.33 a plot of absorption spectra of copper oxide nanoparticles synthesized for 15, 30, 45, and 60 min is shown. Their extracted optical parameters are assembled in Table 3.9 below. The absorption band edges of the materials synthesized at 15, 30, 45, and 60 minutes are observed at 454 nm, 457 nm, 460 nm and 574 nm, respectively. These absorption bands of all four materials are blue shifted from their bulk counterparts. This blue shift results from quantum confinement effects (Smith *et al.* 2010).

Table 3.9: Optical parameters of copper oxide nanoparticles synthesized at 15, 30, 45, and 60 min

Time (min)	Absorption band edge (nm: eV)	Emission peak (nm)	FWHM (nm)
15	454(2.73)	445	90
30	457(2.71)	502	69
45	460(2.70)	503	81
60	574(2.16)	622	116

UV-Vis spectra revealed that the absorption bands tend to increase with the increase in reaction time. This agrees well with what has been reported in literature that prolonged time yields larger particle size due to Ostwald ripening process (Moloto *et al*. 2011). The absorption bands predict that 15 minutes material should have smallest particles while 60 minutes should have the biggest particles when four materials are compared. Figure 3.34 shows the photoluminescence spectra of the prepared copper oxide nanoparticles. The spectra are red shifted from their absorption spectra with intensity peaks that are located at 445, 502, 503, and 622 nm corresponding from 15, 30, 45, and 60 minutes reaction intervals respectively. The emission spectra followed the same trend as their absorption peaks, suggesting that 15 minutes material should have the smallest particles. A narrow emission peak for 30 minutes material is observed than the other three materials with a FWHM of 69 nm. The reduced broadness of this emission peak can be attributed to a narrow size distribution of this material. The FWHM of these materials also increased with reaction time. 60 minutes material produced a very broad emission peak with a FWHM of 116 nm suggesting a polydispersed material.

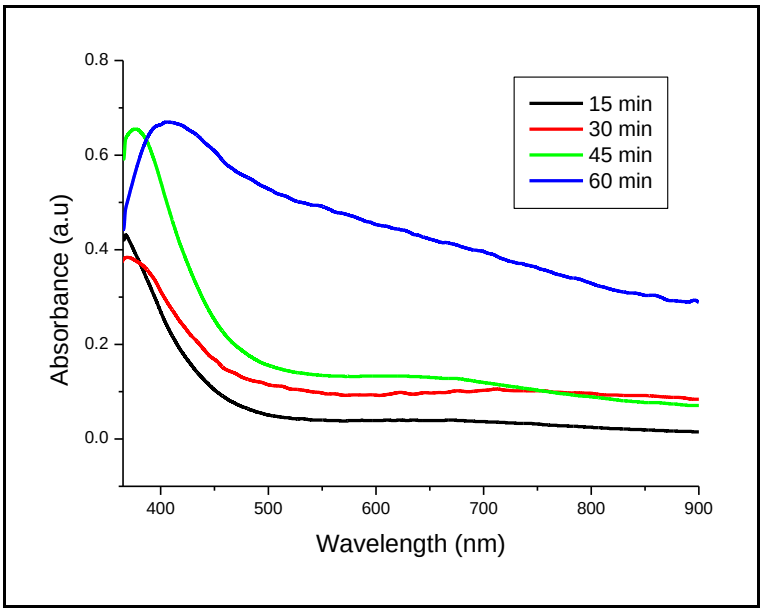

Figure 3.33: Absorption spectra of copper oxide nanoparticles synthesized for 15 min, 30 min, 45 min, and 60 min at 220 °C in OLA using 1:1 mole ratio of CuO.

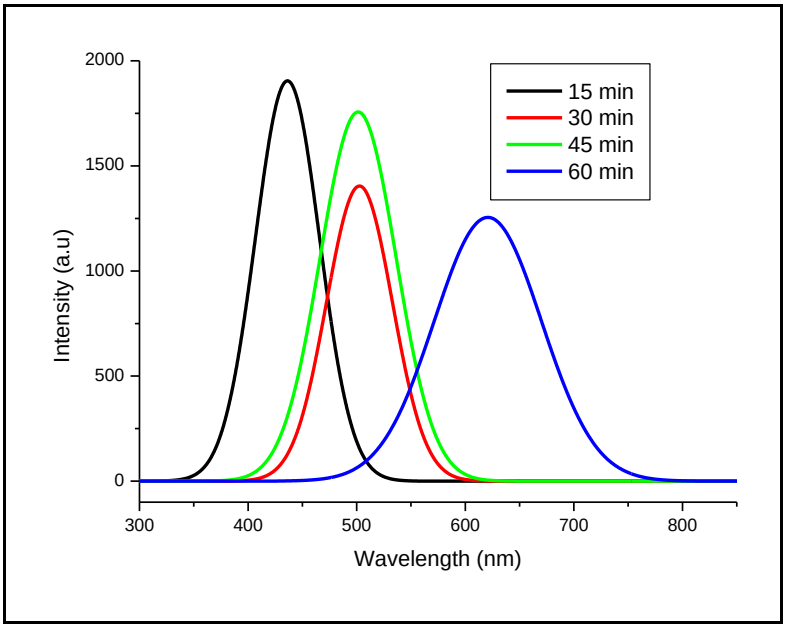

Figure 3.34: Emission spectra of copper oxide nanoparticles synthesized for 15 min, 30 min, 45 min, and 60 min at 220 °C in OLA using 1:1 mole ratio of CuO.

(b) Morphology of the synthesized copper oxide nanoparticles

Figure 3.35 shows the representative TEM images of the obtained copper oxide nanoparticles and their corresponding size distribution graphs. Copper oxide nanoparticles synthesized for 15, 30, 45 and 60 minutes yielded particles of size ranging from 0.8 - 3.2 nm, 0.1 - 8.0 nm, 1 - 12 nm and 5 -60 nm, respectively. It is evident that 15 minutes reaction produced the smallest particles than those synthesized for longer reaction time. The particle size of the four materials increased with the reaction time and this is consistant with literature reports that suggst larger particle size when the nucleation time is prolonged (Moloto *et al*. 2011). The literature further explains this effect by Ostwald ripening process whereby particles group together with smaller ones tending to deposit onto big ones to form larger prticles (Ostwald. 1901; Voorhees. 1985). The synthesis at 15 and 30 minutes produced uniform sphere like shapes that are well dispersed without any aggregation observed.

The materials prepared at 45 minutes possessed larger particles which can be attributed to the grouping of smaller particles via Ostwald rippening. The particles grew as the synthesis time increased to 60 minutes and the sphere like structures were distorted to semi-sphere like structures. These results indicate that the effect of time did not only influence the particles size but also the morphlogy of particles and this is in consistant with what was reported by Ramasamy *et al*. (2010). Copper selenide and copper sulphide demonstrated a different behavior when reaction time was investigated. In the synthesis of copper selenide and copper sulphide, 15 minutes gave the largest particles, The trend that is observed in copper oxides was only observed in copper selenide and copper sulphide when the reaction time was increased from 15 minutes to longer reaction times. This further confirmed the higher reactivity of oxides than sulphides and selenides.

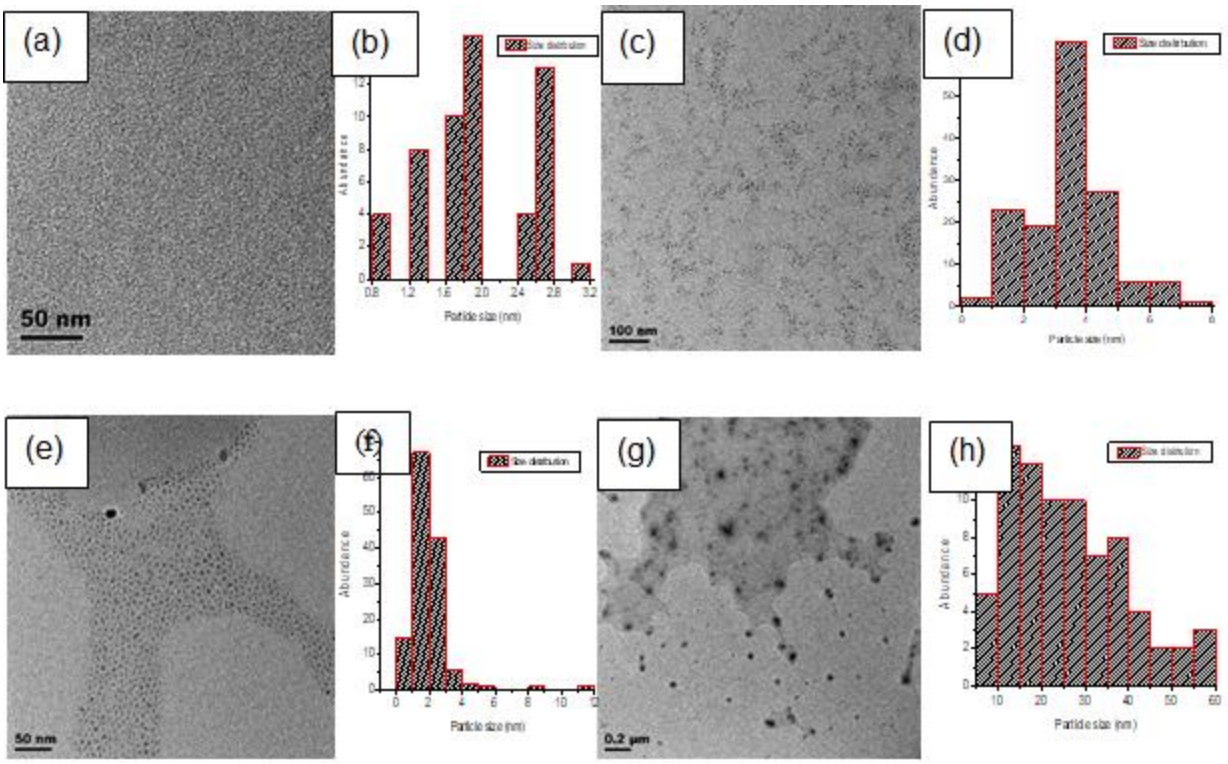

Figure 3.35: TEM images and size histograms of copper oxide nanoparticles synthesized for 15 min (a) & (b); 30 min (c) & (d); 45 min (e) & (f) and 60 min (g) & (h) in OLA at 220 °C using 1:1 mole ratio of CuO.

The synthesized copper oxide nanoparticles was confirmed by XRD analysis and their diffraction patters are displayed on Figure 3.36. XRD results showed that three of the materials (15, 30 and 60 minutes) were mostly formed in Cubic Cu_2O phase. The synthesis at 45 minutes produced only one charecteristic peak which could not be asigned to any phase and therefore it can be speculated that it is also found in cubic Cu_2O phase. The synthesis at 15, 30 and 60 minutes produced major peaks at 2θ values of 37°, 44°, 64°, and 78° which were assigned to (111), (200), (211), and (220) of Cu_2O crystals, respectively. The one characteristic peak that is produced by material prepared at 45 minutes was observed at 2θ value of 78° and therefore is speculated to be indexed to (220) crystalline planes of Cubic Cu_2O phase. The three diffraction patterns can be indexed to PDF card no.05-0667. The mixture of phases that was observed in copper selenide and copper sulphide nanoparticles were not observed in copper oxide nanoparticles. One phase was observed for all reaction times that were used. The effect of reaction time also showed no effect on the phase composition of copper oxide nanoparticles.

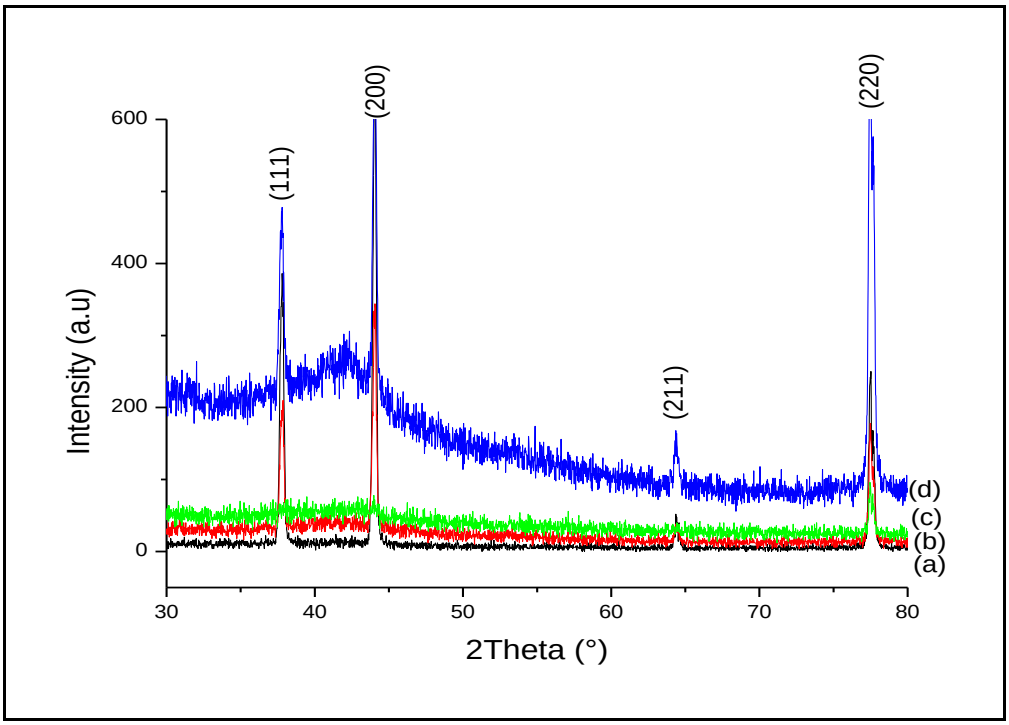

Figure 3.36: XRD patterns of copper oxide nanoparticles synthesized for 15 min (a), 30 min (b), 45 min (c) and 60 min (d) in OLA at 220 °C using 1:1 mole ratio of CuO.

For this study, the optimum reaction time for copper selenide and copper sulphide nanoparticles was found to be 30 minutes whereas copper oxide nanoparticles yielded optimum results at 15 minutes. However, since the three copper chalcogenides were being compared using same conditions, 30 minutes was deduced to be the reaction time to be used when the effect of temperature was investigated.

3.5. The effect of temperature on the synthesis of copper chalcogenides nanoparticles

In this study, the effect of temperature on the synthesis of oleylamine-capped copper selenide, copper sulphide and copper oxide nanoparticles was studied by systematically setting the temperature of the reaction at 160 °C, 190 °C, 220 °C and 240 °C for 30 minutes using 1:1 ratio of precursor concentration in OLA.

3.5.1. The effect of temperature on the synthesis of copper selenide nanoparticles

(a) Optical properties of copper selenide nanoparticles

The absorption spectra of the sytnthesized copper selenide nanoprticles at 160, 190, 220 and 240 °C are depicted on Figure 3.37 and their optical parameters are assembled on Table 3.10 below.

Table 3.10: Optical parameters of copper selenide nanoparticles synthesized at 160, 190, 220 and 240 ºC

Temperature (°C)	Band edge (nm: eV)	Emission peak (nm)	FWHM (nm)
160	514(2.41)	457	53
190	503(2.47)	456	47
220	480(2.58)	441	46
240	663(1.87)	528	57

The band edge of nanoparticles prepared at 160 °C was found at 514 nm. When the temperature of the synthesis was increased to 190 °C the band edge decreased to 503 nm indicating a decrease in particle size. A further decrease in band edge to 480 nm was observed when the temperature was increased further to 220 °C. This blue shift suggests that the particles synthesized at 220 °C should be smaller than those prepared at lower temperatures. It is assumed that due to smaller but sufficient heat of the reaction which leads to lower entropy, smaller particles were favored. When the reaction temperature was further increased to 240 °C the absorption curve red shifted to a higher wavelength. The band edge was found at 663 nm suggesting bigger particles for nanoparticles prepared at 240 °C. All the synthesized nanocrystals showed aborption band edges that are blue shifted compared to their bulk counterpart. Ravi *et al*. (2009) reported a similar trend whereby the reaction temperature was increased from lower temperature to higher temperatures, and the absorption band edges shifted to lower wavelength and suddenly to higher wavelength when the temperature was increased very high. The authors explained that lower temperatures result in moderate superaturation. Therefore, particles grow larger than those prepared at higher temperatures and there after particles grow with the calcination temperature. The material synthesized at 240 °C produced a different absorption curve compared to other materials

suggesting two absorptions for the material. This could be due to Surface Plasmonic Resonance properties that copper chalcogenides nanoparticles exhibit. This suggests different optical properties as Moloto et al. (2011) observed. The emission spectra of the synthesized materials are depicted in Figure 3.38. The maximum emission intensity of materials synthesized at 160 °C, 190 °C, 220 °C, and 240 °C were observed at 457, 456, 441, and 528 nm, respectively. These emission wavelengths suggest that the particle size should decrease as the temperature increased up to 220 °C, then increased as the temperature increased to 240 °C. Narrow emission peaks were observed for all of these materials with FWHM of 53, 47,46, and 57 nm. This indicates that the resultant copper selenide materials have relatively lower size distribution. The material synthesized at 240 °C produced a different emission peak predicting two emission for the material. This could be due to SPR suggested by its absorption line curve. The intensity of this absorption band is greater than intensities of othar materials, indicating either the evolution of particle shapes or wide size distribution of particles.

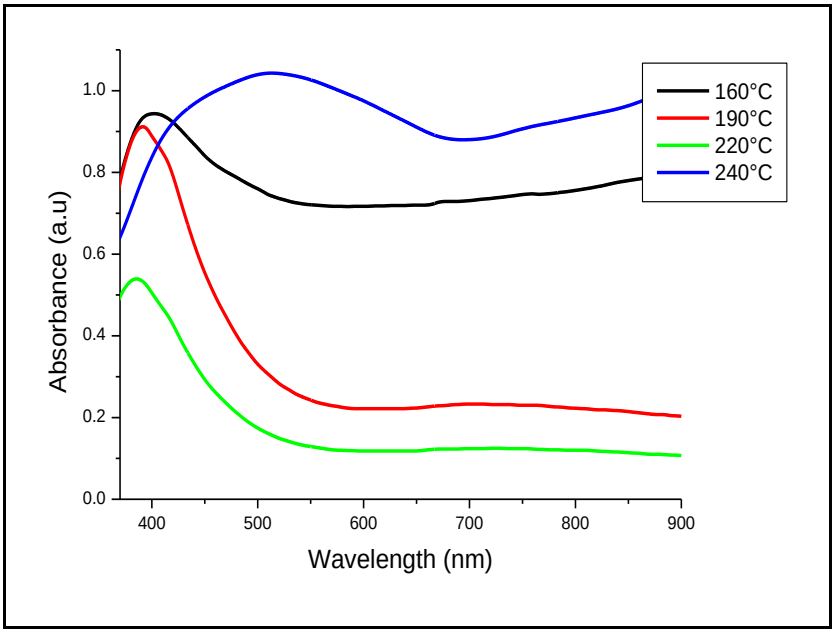

Figure 3.37: Absorption spectra of copper selenide nanoparticles synthesized at 160 ºC, 190 ºC, 220 ºC and 240 ºC for 30 min in OLA using 1:1 mole ratio of CuSe.

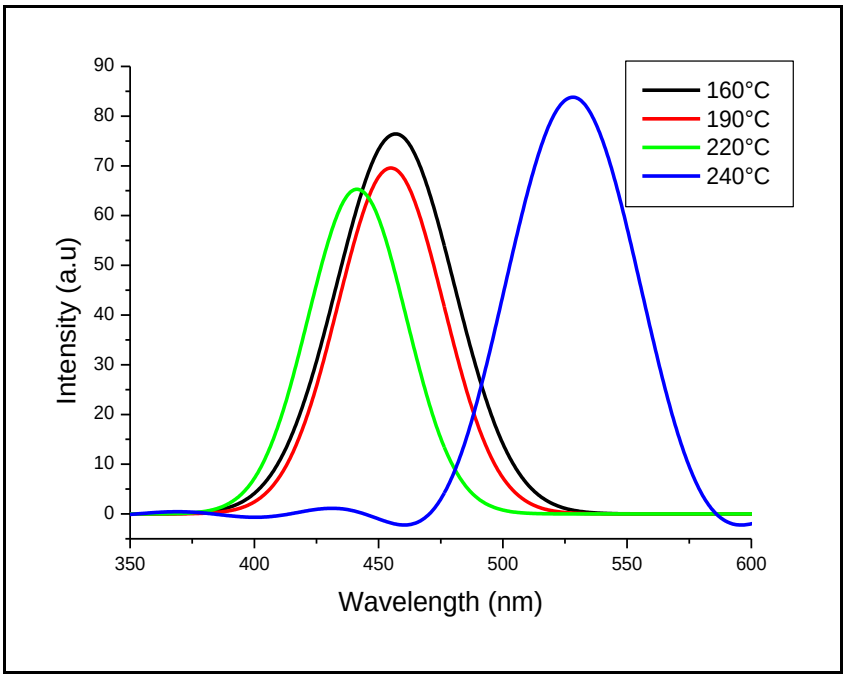

Figure 3.38: Emission spectra of copper selenide nanoparticles synthesized at 160 ºC, 190 ºC, 220 ºC and 240 ºC for 30 min in OLA using 1:1 mole ratio of CuSe.

(b) Morphology of the synthesized copper selenide nanoparticles

TEM images of copper selenide nanoparticles synthesized at 160, 190, 220, and 240 °C and their coresponding size histograms are depicted in Figure 3.39. The material that was sythesized at 160 °C produced particles with an average size range of 31 nm with semi-spherical shapes. It was observed that when the temperature of the reaction was increased from 160 °C to 190 °C, the size of the particles decreased to an average size of 13 nm. The shape became a little pronounced and appeared almost spherical. When the temperature was increased further from 190 °C to 220 °C, a continued nucleation with smaller particles having an average size of 12 nm occurred because high temperature (220 °C) favoures a fast hydrolysis reaction and results in the high supersaturation. A large ΔGv which in turn results to the formation of a large number of small nuclei (Li *et al*. 2013). When the temperature was increased further more from 220 °C to 240 °C, this led to an increase in solubility and thus reduced the supersaturtion of the solution a consequece larger particle with sizes average of 23 nm were obtained (Sugimoto *et al*. 2001). At this temperature (240 °C) the morphology of the particles changed from spherical shapes to mixed morphology. This revealed that the material is composed of hexagonals, tubes, and trancated triangles which were not observed on the other three materials that were synthesized at temperatures below 240 °C.

Particles synthesized at 240 °C gave the largest particles compared to other three materials that were synthesized at lower temperatures. The evolution of particle shapes that was predicted by emission peak was also observed. This material showed to have a wide size range of particles which is between 2 nm to 90 nm and this corroborate its broader emission peak with a FWHM of 57 nm. Amongst the four temperatures that were selected for the synthesis of copper selenide nanoparticles, 190 °C and 220 °C materials produced better optical properties and smaller particles. Therefore, the above temperatures samples were furthure charecterized with XRD to study their crystal structure and phase composition.

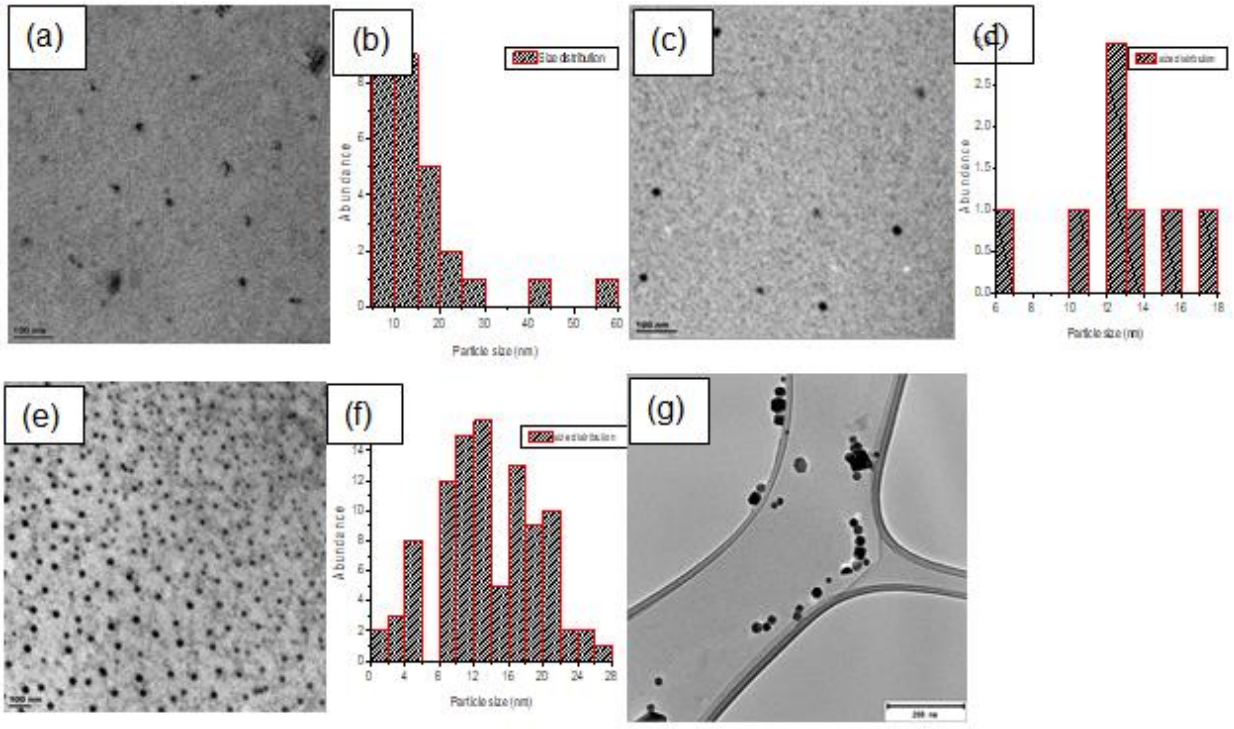

Figure 3.39: TEM images and histograms of copper selenide nanoparticles synthesized at 160 °C (a) & (b); 190 °C (c) & (d); 220 °C (e) & (f) and 240 °C (g) for 30 min in OLA using 1:1 mole ratio of CuSe.

Figure 3.40 shows the XRD patterns of copper selenide nanomaterials synthesized at 190 °C and 220 °C. The results confirmed that both temperatures have successfuly obtained copper selenide nanoparticles. Both synthesized copper selenide nanoparticles showed a mixture of phases which are found in a dominant Hexagonal $Cu_{0.87}Se$ (Klockmannite) crystal structure which is indexed to

PDF card no. 04-007-2214 with crystal planes that are observed at 2θ values 27°, 29°, 30°, 31°, 41°, 45°, 49°, 56°, 63°, 65°, 67°, 70°, 74° and 88° corresponding to (100), (110), (102), (103), (006), (106), (107), (108), (203), (206), (1011), (207), (208), (210) and (0014), respectively. The less dominant orthorhombic CuSe2 phase was indexed to JCPDS card no. 04-004-2178 with diffractions that are located at 2θ values 23°, 33°, 34°, 39°, 42°, 49°, 53°, 54° and 60° corresponding to crystal planes (111)*, (120)*, (211)*, (121)*, (200)*, (211)*, (131)* and (122)* respectively. An impurity of unreacted Se was observed at crystal plane 36° corresponding to (211) which was indexed to PDF card no. 01-086-0521. The sharpness of the diffraction peaks of the material synthesized at 190 °C is ascribed to larger particles and good crystallinity. This corroborates the optical properties and particle sizes obtained by TEM. These results indicate that the factor of temperature does not only affect the size and the morphology of the particles but the crystallinity as well.

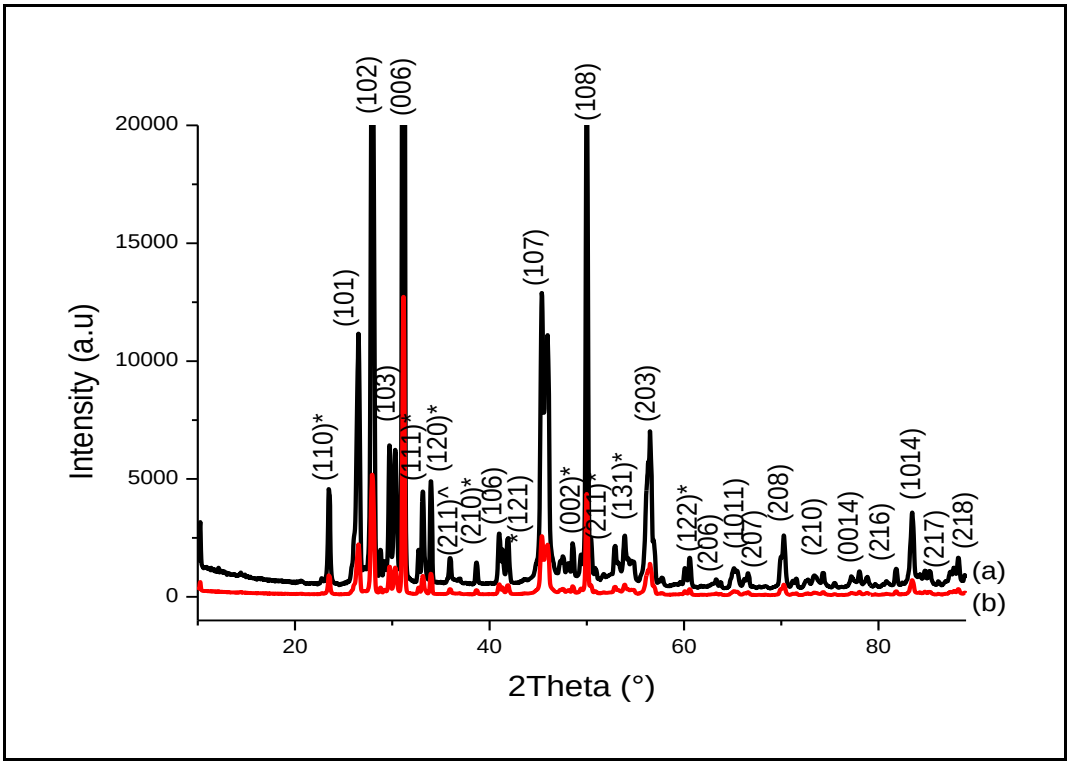

Figure 3.40: XRD patterns of copper selenide nanoparticles synthesized at 190 °C (a) and 220 °C (b) for 30min in OLA using 1:1 mole ratio of CuSe.

3.5.2. The effect of temperature on the synthesis of copper sulphide nanoparticles

(a) Optical properties of copper sulphide nanoparticles

The optical properties of the synthesized copper sulphide nanoparticles were investigated by absorption and emission spectroscopy and their spectra are depicted in Figure 3.41 and Figure 3.42 respectively. The extracted optical parameters are listed on Table 3.11 below.

Table 3.11: Optical parameters of copper sulphide nanoparticles synthesized at 160, 190, 220 and 240 ºC

Temperature (°C)	Band edge (nm: eV)	Emission peak (nm)	FWHM (nm)
160	658(1.88)	440	86
190	568(2.18)	443	50
220	555(2.23)	455	45
240	763(1.63)	587	50

The absorption spectra revealed that the four materials synthesized at 160, 190, 220 and 240 °C have band edges that are located at 658, 568, 555, and 763 nm, respectively. This indicates that all four materials have band edges that blue shift from their bulk counterparts. The band edges of these materials suggest that the size of the particles is decreasing with an increase in temperature reaction up until 220 °C, then from 220 °C to 240 °C the size starts to increase. The same trend was observed on the synthesis of copper selenide nanoparticles under these conditions. Three of these materials (160 °C, 190 °C, and 240 °C) gave similar absorption structure which is an indicative of a Covellite phase (Zou *et al*. 2007; Lisiekcki *et al*. 1993 and Jiang Tang *et al*. 2008). 220 °C material gave a different absorption structure that suggests that the optical properties of this material should differ from the rest of the three materials. The absorption band edge of the material synthesized at 220 °C suggest smaller particles than three other materials. This might be due to sufficient heat that resulted to super-saturation, and thereby high degree of nucleation hence smaller particles were obtained (Wang *et al*. 2002). 240 °C material showed to have smaller particles than 160 °C and 190 °C but larger particles than 220 °C. This might be due to higher temperatures that increased solubility which leads to smaller supersaturaion of the solution

resulting to larger particles being produced (Ravi *et al*. 2009). The emission peaks that are located at 440, 443, 455 and 587 nm were observed for 160 °C, 190 °C, 220 °C and 240 °C, respectively. 190 °C, 220 °C and 240 °C materials produced narrower emission peaks with FWHM of 50, 45, and 50 nm, respectively predicting a monodispersed distribution. 160°C material shown to have a broader emission peak than the other three materials with a FWHM of 86 nm, indicating a polydispersed distribution.

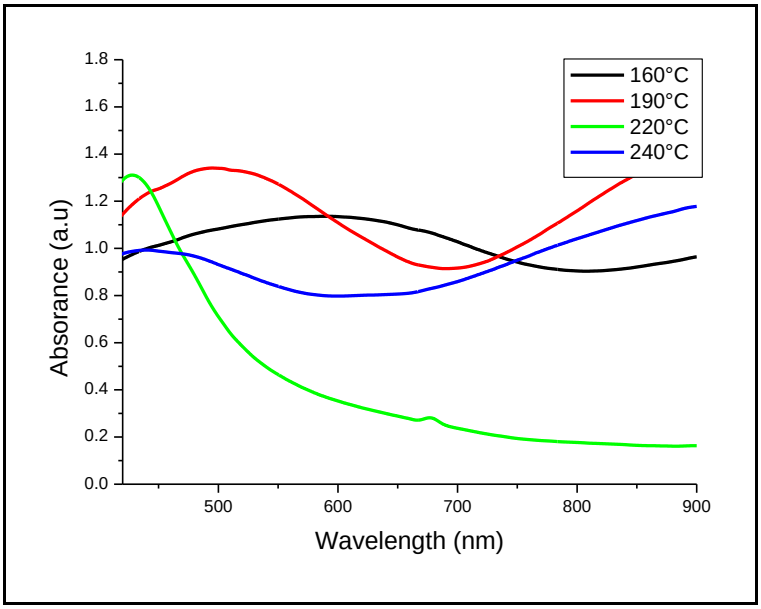

Figure 3.41: Absorption spectra of copper sulphide nanoparticles synthesized at 160 ºC, 190 ºC, 220 ºC and 240 ºC for 30 min in OLA using 1:1 mole ratio of CuS.

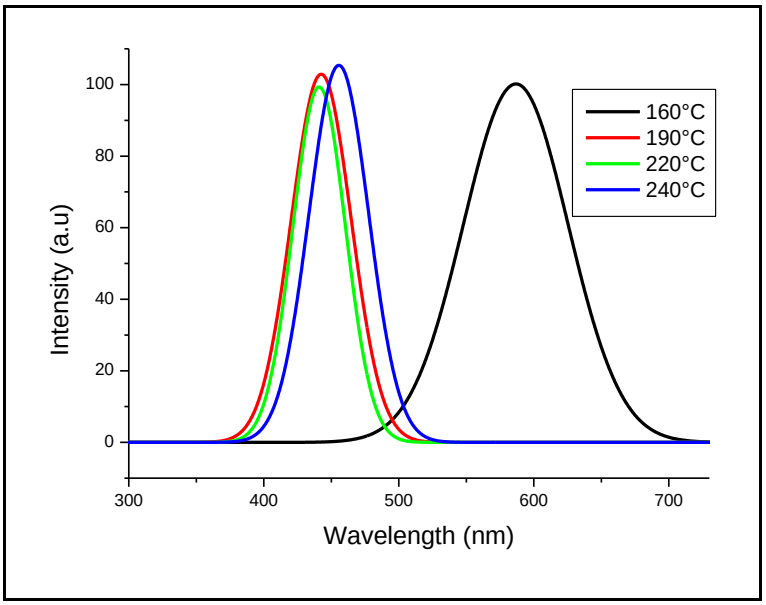

Figure 3.42: Emission spectra of copper sulphide nanoparticles synthesized at 160 ºC, 190 ºC, 220 ºC and 240 ºC for 30 min in OLA using 1:1 mole ratio of CuS.

(b) Morphology of the synthesized copper sulphide nanoparticles

TEM images of the synthesized copper sulphide nanoparticles are depicted on Figure 3.43. The materials synthesized at 160 °C, 190 °C, 220 °C and 240 °C produced particles with average size of 29 nm, 24 nmn, 11 nm and 15 nm, respectively. TEM images revealed that there is a significant variation in particle size among the four samples and the particle size is decreasing with an increase in temperature until the temperature of 220 °C was reached then started to increase when the temperature was increased to 240 °C. 160 °C and 190 °C materials produced larger particles than the ones that are prepared at higher temperatures. These large particles have defined shapes which revealed that particles have mixed morphology that includes rods, spheres and truncated triangles that are dominating. The presence of rod-like structures might be an indication of an insuficient heat during the reaction which lead to a low supersaturation of the solution. As a consequence, large size particles were obtained that are agglomerated. TEM image of 220 °C material confirmed that indeed the material has the smallest particles size than the other three materials with no agglomoration. This corroborates what was suggested by optical properties of these materials which predicted a decrease in particle size from 160 °C to 220 °C then an increase to 240 °C. The reduced particle size for 220 °C material is due to high temperature that favoured a fast hydrolysis reaction and resulted in high super-saturation and thereby a large ΔG_v. This in turn, leads to the

formation of a large number of small nuclei which is a consiquence of small particle size. After the temperature was increased from 220 °C to 240 °C the size of the particles started to grow to a bigger size as well due to calcination temperature. The size distribution of all these materials is narrow and this is in agreement with what was predicted by emission peaks. Since 220 °C gave the smallest particles that are well passivised and well distributed. This temperature is taken as an optimum temperature under these reaction conditions therefore it was used on the investigtion of other parameters. Amongst the four temperatures that were used for synthesis, 220 °C and 240 °C nanomaterials gave better optical and structural properties. Therefore, the above temperatures samples were further characterized by XRD to study their phase composition and their crystallinity.

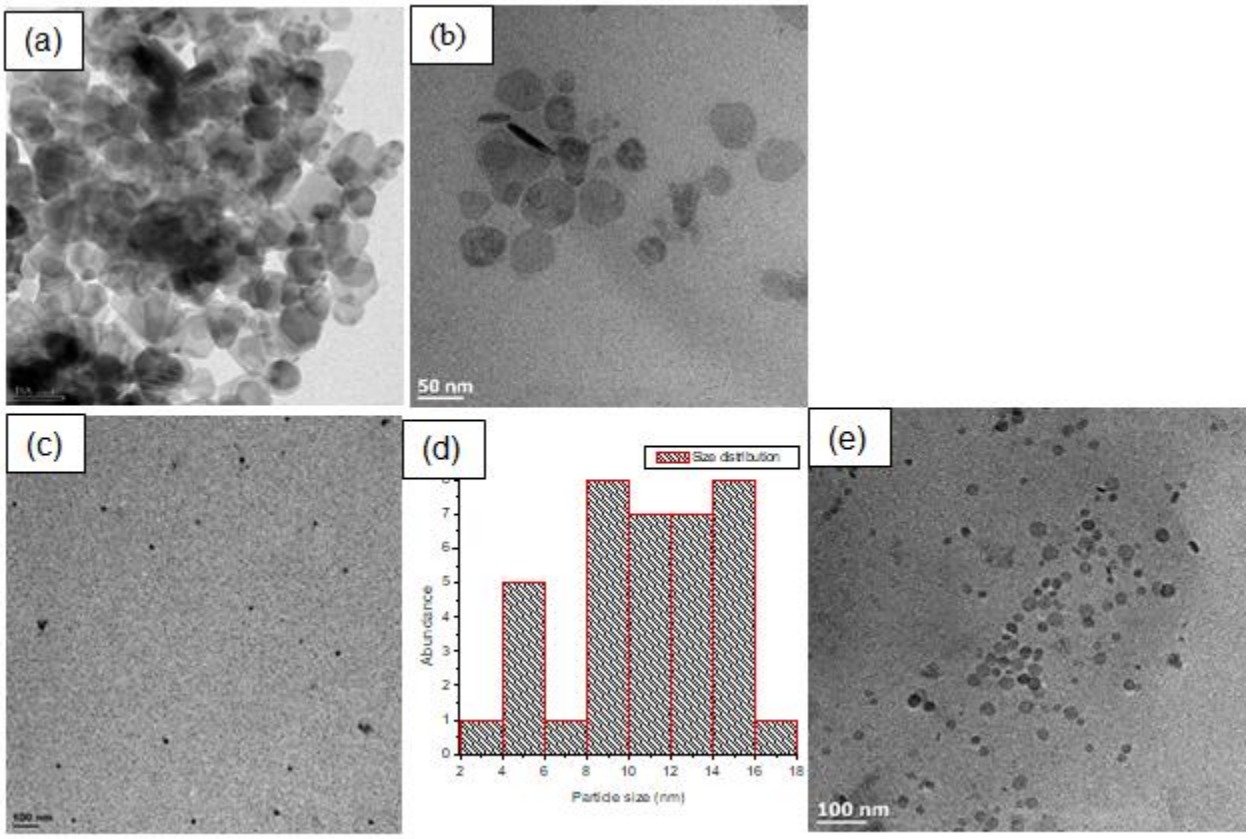

Figure 3.43: TEM images and histogram of copper sulphide nanoparticles synthesized at 160 °C (a); 190 °C (b); 220 °C (c) & (d) and 240 °C (e) for 30 min in OLA using 1:1 mole ratio of CuS.

XRD patterns of the material synthesized at 220 °C and 240 °C are depicted on Figure 3.44. The XRD diffraction patterns confirmed that copper suphide nanoparticles were successfully synthesized in both temeratures. 220 °C material exhibit mixture of phases which were assigned to Rhombohedral Cu_9S_5 (Digenite) phase indexed to PDF card no 04-047-1748 and Covellite CuS phase indexed to PDF card no 04-001-1461. The diffraction pattern produced by the material synthesized at 240 °C were assigned to Covellite CuS phase indexed to PDF card no 04-001-1461. The Covellite phase of the of this material is in agreement with the shape of the absorption band of the correspondance. The major peaks of the materials synthesized at 220 °C were found at 2θ values 26°, 28°, 29°, 32°, 36°, 28°, 42°, 46°, 50°, 51°, 57°, 64°, 67°, 72°, 75° and 86° responding to planes (101), (0015), (107), (1010), (1013), (0114), (0117), (0120), (119), (0027), (0030), (0033), (2020), (1127), (207) and (1220). The crystal planes of the second phase were located at 2θ values 48°, 55°, 60°, 74° and 79° corresponding to (107)*, (311)*, (116)*, (208)* and (209)*. The major peaks of the materials synthesized at 240 °C were found at 2θ values 27°, 30°, 39°, 48°, 53°, 57°, 59°, 63°,74°, 78°, 79°, 86°and 90° corresponding to crystal planes (101), (102), (105), (110), (108), (202), (205), (208), (212), (213), (216) and (300). The crystal planes of the second phase were located at 2θ values 32°, 46°, 55° and 68° corresponding to (200)*, (220)*, (311)* and (400)*. Few impurities that could be due to unreacted precursors were observed at 2θ values 42° and 70° and denoted by +. The diffraction patterns suggest that with higher temperatures, purer phases of nanomaterials are produced. The diffraction patterns revealed that temperature change had a slight effect on the phase composition of particles.

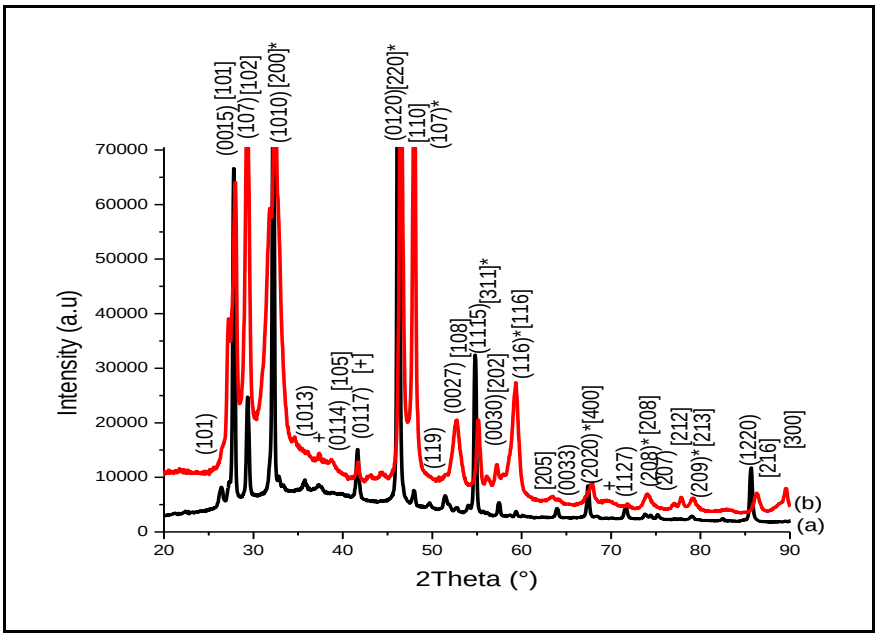

Figure 3.44: XRD patterns of copper sulphide nanoparticles synthesized at 220 °C (a) and 240 °C (b) for 30 min in OLA using 1:1 mole ratio of CuS.

3.5.3. The effect of temperature on the synthesis of copper oxide nanoparticles

(a) Optical properties of copper oxide nanoparticles

Figure 3.45 shows absorption spectra of copper oxide nanoparticles synthesized at different temperatures and the extracted optical parameters of the synthesized materials are assembled on Table 3.12 below. UV/Vis spectroscopy revealed that the absorption bands edges of the 160 °C, 190 °C, 220 °C, and 240 °C synthesized copper oxide nanoparticles are located at 491, 498, 515, and 529 nm respectively. The absorption spectra showed a considerable blue shift with respect to bulk counterparts which could be ascribed to quantum size effect of the nanoparticles.

Table 3.12: Optical parameters of copper oxide nanoparticles synthesized at 160, 190, 220 and 240 ºC for 30 min in OLA using 1:1 mole ratio

Temp (°C)	Band edge (nm: eV)	Emission peak (nm)	FWHM (nm)
160	491(2.53)	443	79
190	498(2.49)	444	89
220	515(2.42)	448	73
240	529(2.34)	463	95

As the temperature was increased, a red shift of absorption band was observed suggesting an increase in particle size through Ostwald ripening process (Ostwald *et al.* 1901; Cheng *et al.* 2010). This trend was not observed in copper selenide and copper sulphide nanoparticles, rather their band edges decreased with the increase in temperature up until 220 °C then increased when the temperature was increased to 240 °C. A high degree of tailing is observed in all four absorption spectra. This could be due to the dispersive scattering by the particles in the dispersion system (Xiao *et al.* 2012) or particles that are closely packed. All four materials produced similar absorption curves predicting similar optical properties. Figure 3.46 shows the corresponding emission spectra of all four materials with maximum intensities that are located at 443, 444, 448 and 463 nm, respectively. The emission peaks followed the same trend as the absorption peaks, by increasing to a higher wavelength with the increase of temperature. 160 °C and 220 °C materials produced a narrower emission peaks than the other two materials with a FWHM of 79 and 73 nm while 190 °C and 240 °C materials produced wider emission peaks with FWHM of 89 and 95 nm respectively. The narrowness of the emission peaks of 160 °C and 220 °C materials suggesting a narrow size distribution of particles.

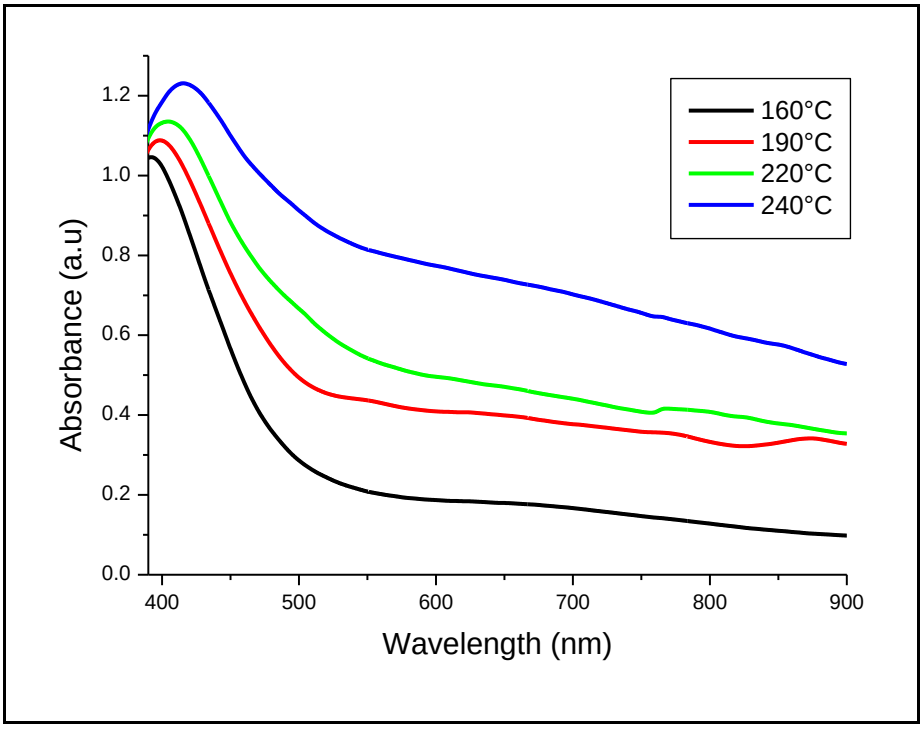

Figure 3.45: Absorption spectra of copper oxide nanoparticles synthesized at 160 ºC, 190 ºC, 220 ºC and 240 ºC for 30 min in OLA using 1:1 mole ratio of CuO.

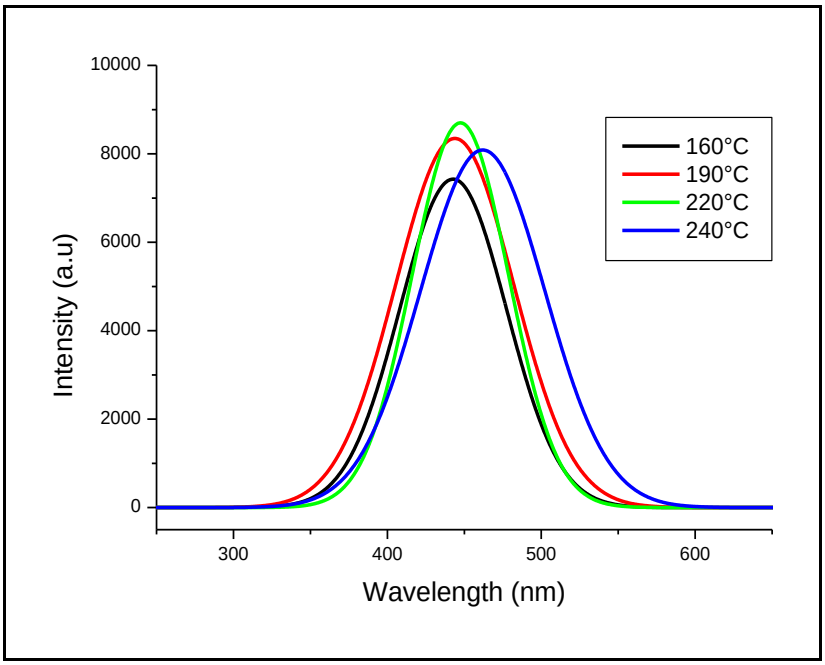

Figure 3.46: Emission spectra of copper oxide nanoparticles synthesized at 160 ºC, 190 ºC, 220 ºC and 240 ºC for 30 min in OLA using 1:1 mole ratio of CuO.

(b) Morphology of the synthesized copper oxide nanoparticles

The TEM images of copper oxide nanoparticles prepared with various temperature reactions are depicted on Figure 3.47 together with their coresponding size distribution graphs. Copper oxide nanoparticles synthesized at 160, 190, 220 and 240 °C yielded particles of average size of 1.5, 2, 3 and 3.5 nm respectively. TEM results revealed that copper oxide nanoparticles are prepared at lower temperatures (160, 190, and 220 ºC) are all almost spherical and their sizes increased with temperature of the reaction, whereas 240 °C material produced short rod like structure. The increase in particle size is in good agreement with what was predicted by their optical properties. The increase in particle size is due to the fact that an increase in temperature leads to increased solubility and hence reduced supersaturation of the solution and as consiquence large particle size are produced. All four materials produced well distributed particles and this is in agreement with their corresponding narrower emission peaks predicting a monodispersed population. The four materials were further characterized by XRD to study their crystallinity and size composition.

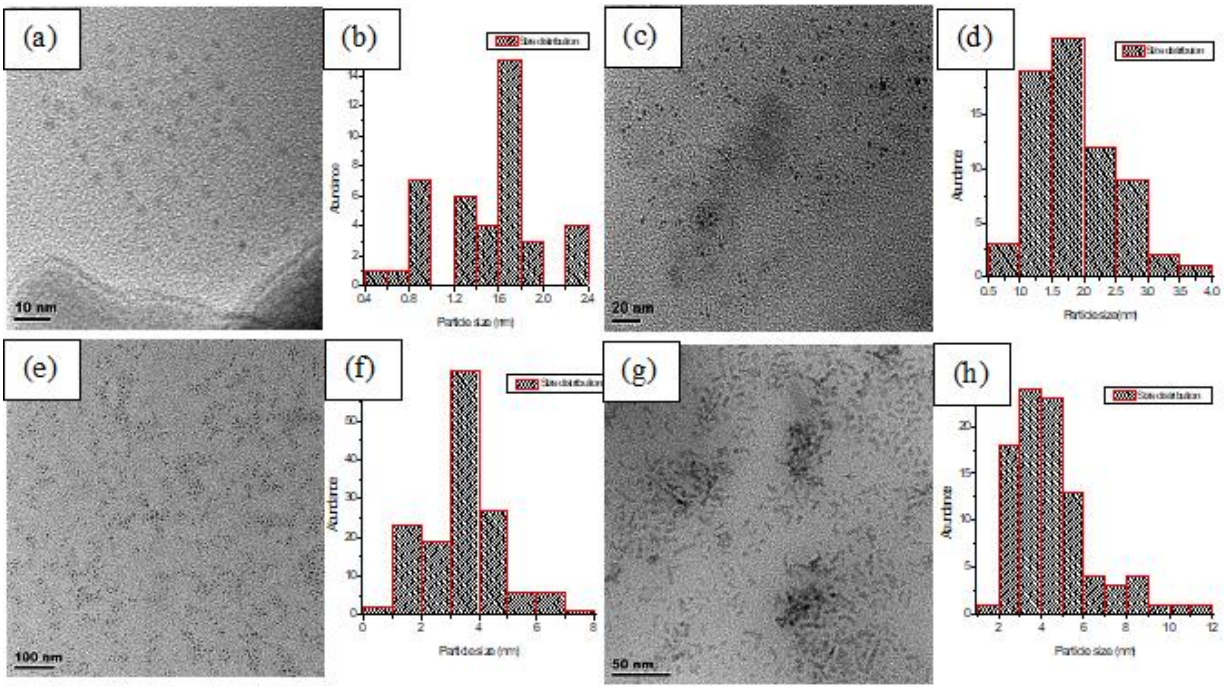

Figure 3.47: TEM images and histograms of copper selenide nanoparticles synthesized at 160 °C (a & b); 190 °C (c & d); 220 °C (e & f) and 240 °C (g & h) for 30 min in OLA using 1:1 mole ratio of CuO.

XRD analysis was undertaken to complement the structure of synthesized materials and the diffraction patterns are depicted in Figure 3.48. XRD pattern revealed that 160 °C and 190 °C materials are found in Monoclinic CuO phase indexed to PDF card No. 45-0937. The diffraction peaks of 160 °C were observed at 2θ values of 31°, 32°, 33°, 48°, 54°, and 77° which closely correspond to planes (110), (002), (111), (202), (020), and (222). The material synthesized at 190 °C showed similar diffraction peaks at 160 °C material except for the peaks that were observed at 2θ values of 48° and 54° which were not observed on the material synthesized at 160 °C. The material synthesized at 220 °C and 240 °C produced diffraction peaks that were found as face-centered Cubic structure of Cu_2O phase indexed to PDF card No. 78-2076. The characteristic peaks were observed at 2θ values of 37°, 44°, 64°, and 78° corresponding to planes (111), (200), (220), and (222). The diffractogram peaks of 240 °C material at observed at 38° and 44° were not well defined and this might be due to the material that is highly amorphous. The results indicates an increase in peak width with the increase in temperature predicting an increase of particle size.

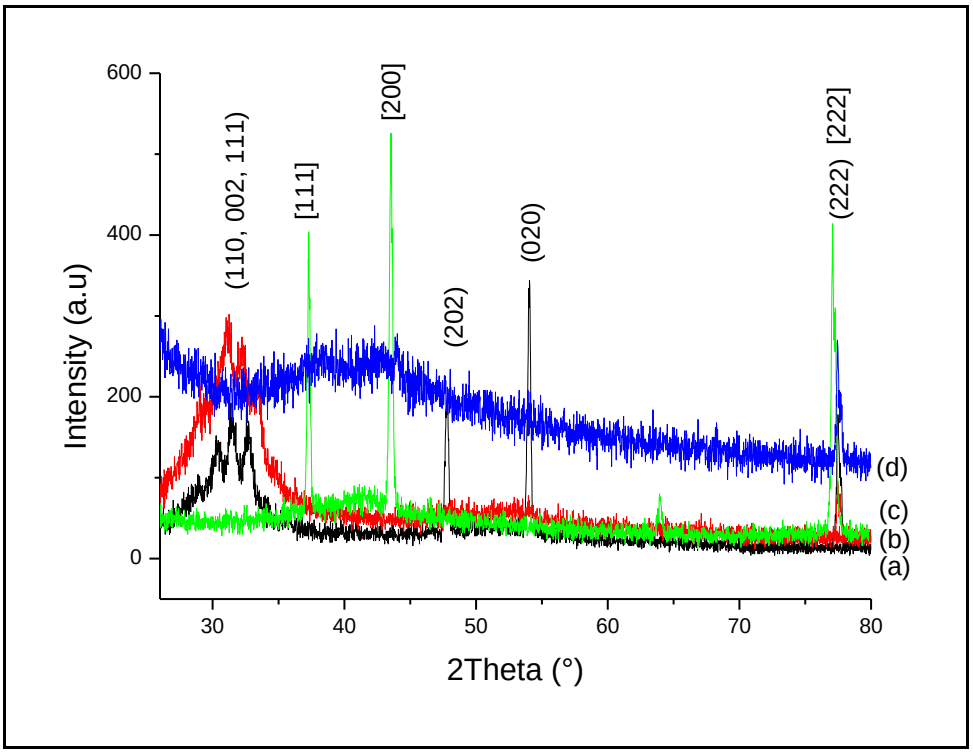

Figure 3.48: XRD patterns of copper oxide nanoparticles synthesized at 160 ºC, 190 ºC, 220 ºC and 240 ºC for 30 min in OLA using 1:1 mole ratio of CuO.

3.6. Characterisation of medicinal plants (*Combretum molle* and *Acacia mearnsii*)

Combretum molle and *Acacia mearnsii* were phytochemically screened for bioactive compounds. The content of phenols, flavonoids, and antioxidants properties were determined for extracts different polarities.

3.6.1. Phytochemical analysis of plants extracts

In this study, the presence of different colours after spraying with the vanalin spray indicated the presence of chemical constituents of plant extracts as per Wagner *et al.* (1996). According to Wagner *et al.* (1996) the characteristic green and blue fluorescence indicates the presence of flavonoids while yellow colour after spraying with DPPH (Lapornik *et al.* 2004) indicates the antioxidant capabilities. *Combretum molle* and *Acacia mearnsii* demonstrated all the characteristic colors of the compounds of interest and confirmed the presence of phenols, flavonoids and antioxidant capabilities, respectively.

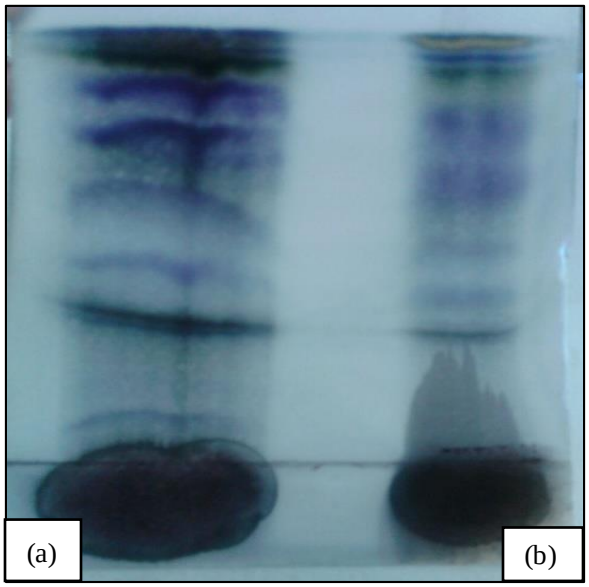

Figure 3.49: TLC separation of components of *Combretum molle* (a) and *Acacia mearnsii* (b) methanolic plant extracts.

According to literature, antioxidant activity of plants is due to the presence of phenolic compounds (Cook *et al*. 1996). A relationship of total flavonoid and phenol contents with antioxidant activity has also been found. Some evidence suggests that the biological actions of flavonoids compounds are related to their antioxidant activity. Recently, bioactive flavonoids have also been investigated for potent anti-viral/bacterial activity (Pourmoradi *et al*. 2006). An easy, rapid and sensitive method for determining the content of antioxidant in plant extracts used was the free radical scavenging assay using 1,1-diphenyl-2-picryl hydrazyl (DPPH) stable radical spectrophotometrically. When the antioxidants are present, the DPPH radical obtain one electron from the plant extract and this lead to a decrease in absorbance (Koleva *et al*. 2002). In this study, the total content of phenolic and flavonoids compounds in *Combretum molle* and *Acacia mearnsii* were investigated to estimate their antioxidant activity. The phenolic content of *Combretum molle* and *Acacia mearnsii* plants was determined using Folin Ciocalteu reagent which is also known as Gallic Acid Equivalence method (GAE) and therefore gallic acid was used as a standard reference material for the determination of phenols. Aluminum chloride colorimetric method was used for the determination of flavonoids and quercetin was used as a reference because they are natural flavonoids that are found abundantly in plants. This is expressed as Quecertin Equivalence QUE method.

3.6.2. Determination of total phenolic contents in the plant extracts

The crude plant extracts of both *Combretum molle* and *Acacia mearnsii* were tested for the total concentration of phenols using solvents with different polarities. The phenolic content was determined by Ultraviolet Visible spectroscopy and was measured by Folin's reagent in terms of gallic acid equivalence using the standard curve equation:

$$y = 0.0031x + 0.0424,\ r^2 = 0.9967 \quad (13)$$

which is the result of a linear fit shown in the appendix.

The concentration of phenols in samples was determined as milligrams of gallic acid equivalent by using the following equation:

$$A = (c \times v) / m \quad (14)$$

where,

A = Total phenols content (mg/g gallic acid)

C= X/ 1000 = Concentration of gallic acid in mg/ml

v = Volume of extract

m = Mass of the extract (g)

An alternative formula $M_1V_1=M_2V_2$ can be used to calculate the total phenol content in plants.

The calibration curve of gallic acid where the equation was obtained is displayed in the appendix together with Table 3.19 that shows the concentration and absorbance values of the calibration curve. The phenolic concentration results of *Combretum molle* and *Acacia mearnsii* extracts for each solvent are shown in Figure 3.50(a) 3.50(b), respectively. In *Combretum molle*, chloroform, methanol, acetone and water extracts gave phenol content of 89.87, 84.07, 97.29 and 88.90 mg/g respectively. In *Acacia mearnsii*, chloroform extract gave the phenolic concentration of 53.74 mg/g, methanol extract gave a concentration of 89.87 mg/g. Acetone extract showed the phenol concentration of 98.54 mg/g which is the highest followed by water extract which produced a phenolic concentration of 96.65 mg/g. The results revealed that both *Combretum molle* and *Acacia mearnsii* acetone extracts gave the highest concentration of phenol. Zlotek *et al*. (2012) reported

his findings on *Combretum molle* using acetone and confirmed that acetone produced highest phenolic content. The lowest concentration of phenols in *Combrettum molle* was observed in methanol extract whereas in *Acacia mearnsii* it was observed in chloroform extract.

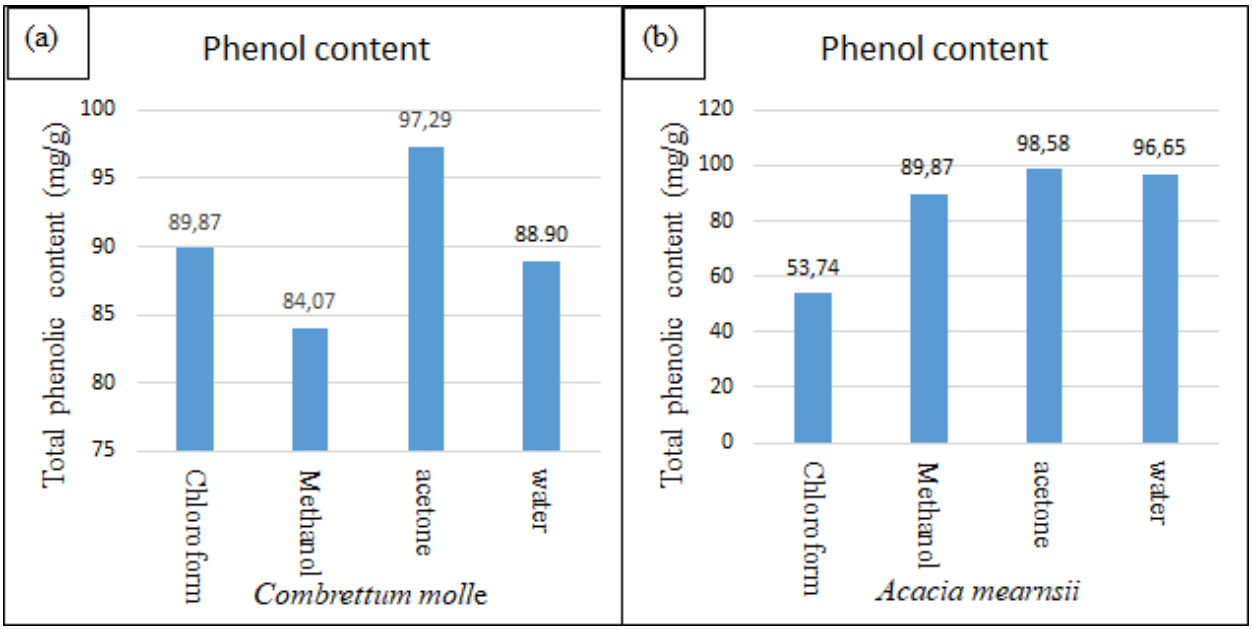

Figure 3.50: The percent relative phenolic content of *Combretum molle* (a) and *Acacia mearnsii* (b) with different solvent extracts.

The methanol extract gave the lowest phenolic concentration compared to the other three solvents of extracts with a significant difference value of >13 mg/g. Chloroform gave the lowest concentration of phenols with a significant difference value of >3 mg/g. These significant values show that the total concentration of phenols highly depends on the solvent used for extraction. For *Combretum molle,* the total phenol varied from 53.74 ± 5 to 97.29 ± 3 mg/g in the extraction powder. For *Acacia mearnsii* with the highest content of phenols, the concentration varied from 53.74 ± 7 to 98.58 ± 2 mg/g. *Acacia mearnsii* produced slightly higher phenolic concentration than *Combretum molle*.

Table 3.13: Data for the determination of Gallic acid content of *Combretum molle* and *Acacia mearnsii*

Plant name	Solvent name	GAC as GAE (mg/g)
Combretum molle	Chloroform	89.87 ± 2
	Methanol	84.07 ± 3
	Acetone	97.29 ± 5
	Water	53.74 ± 3
Acacia mearnsii	Chloroform	53.74 ± 7
	Methanol	89.87 ± 3
	Acetone	98.58 ± 2
	Water	96.65 ± 3

3.6.3. Determination of flavonoids concentration in the plant extracts

The concentration of flavonoids in *Combretum molle* and *Acacia mearnsii* plant extracts was determined with Ultraviolet Visible spectroscopy using aluminum chloride method. The content of flavonoids on these plant species was expressed in terms of quercetin equivalent (the standard curve):

$y = 0.0072x + 0.0023,\ r^2 = 0.9976$ (15)

which is the result of a linear fit shown in the appendix.

The concentration of flavonoids in samples was determined as milligrams of quercetin equivalent by using the following equation:

$A = (c \times v) / m$

where,

A = Total flavonoid content (mg/mg quercetin)

C= X/ 1000 = Concentration of quercetin in mg/ml

v = Volume of extract

m = Mass of the extract (mg)

The results are presented on Table 3.14 below. The results showed that concentration of flavonoids in *Combretum molle* varies from 114.54 ± 0.18 to 76.90 ± 2 mg/g. In *Combretum molle* solvents of extracts chloroform, methanol, acetone and water gave the flavonoids concentrations of 89.68, 114.54, 103.43 and 76.90 mg/g, respectively. Methanol gave the highest concentration of flavonoids followed by acetone then chloroform. Water solvent gave the lowest concentration of flavonoids. In *Acacia mearnsii*, the content of flavonoids varied from 89.40 ± 3 to 105.45 ± 0.15 mg/g. Chloroform, methanol, acetone and water showed their flavonoids concentration to be 89.40, 95.93, 105.45 and 90.24 mg/g, respectively. Acetone gave the highest concentration of flavonoids followed by methanol then water. Considering the experimental error, both chloroform and water gave the lowest concentrations with no significant difference. These results confirmed that the total flavonoid content is also dependent on solvent of extracts. The concentration of flavonoids of these plant extracts is also presented in a graphical form in Figure 3.51 below to indicate their concentration differences. *Combretum molle* extract gave higher flavonoids concentration than *Acacia Mearnsii* extracts.

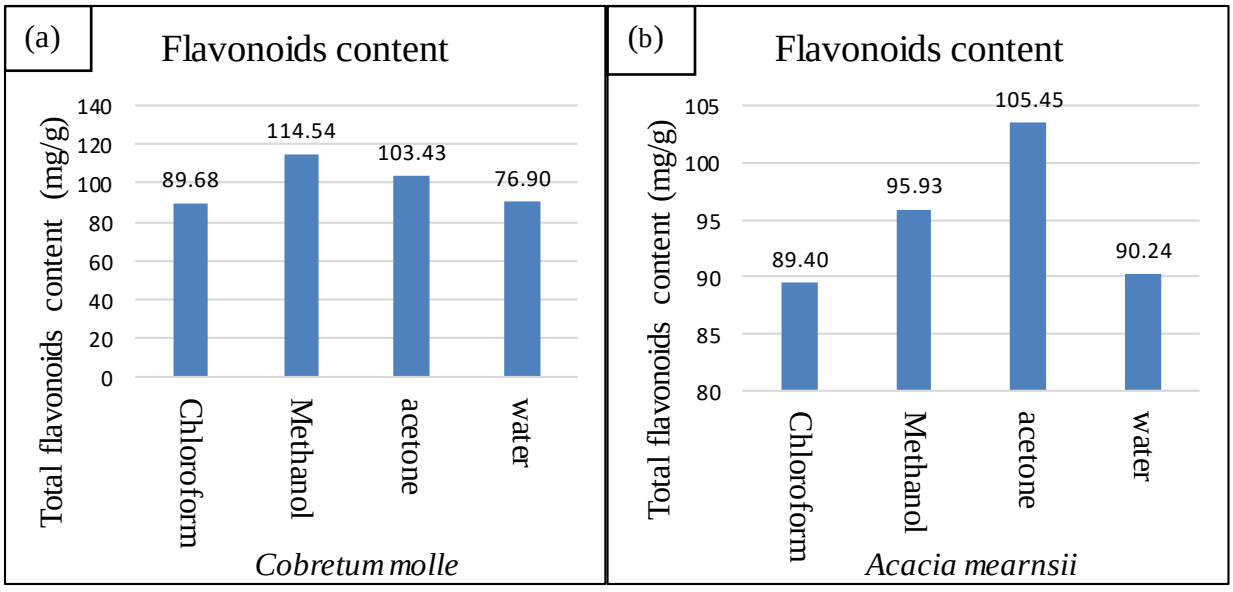

Figure 3.51: The percent relative flavonoids content of (a) *Combretum molle* (b) *Acacia mearnsii* with different solvent extracts.

Table 3.14: Data for the determination of quercetin content of *Combretum molle* and *Acacia mearnsii*

Plant name	Solvent name	QUC as QUE (mg/g)
Combretum molle	Chloroform	89.68 ± 1
	Methanol	114.54 ± 0.2
	Acetone	103.4 ± 0.2
	Water	76.90 ± 2
Acacia mearnsii	Chloroform	89.40 ± 3
	Methanol	95.93 ± 0.9
	Acetone	105.45 ± 0.2
	Water	90.24 ± 1

3.6.4. DPPH radical scavenging assay

The DPPH radical scavenging assay was done in crude extract from *Combretum molle* and *Acacia mearnsii* with different solvents including methanol, ethanol, acetone, and chloroform at different concentrations. The data was presented in form of line graphs together with ascorbic acid and gallic acid which were both used as phenol reference standards. The experiments were performed in triplicate readings. % DPPH inhibition was determined using formula:

Scavenged DPPH % = $[(A_0 – A1) / A_0] \times 100\%$

where, A_0 is the absorbance of the control and A_1 is the absorbance of extract

Figure 3.62 shows a plot of methanolic extract of *Combretum molle*. This extract displayed 99.54% inhibition of DPPH radical scavenging activity at 0.5 mg/ml and 99.3% at 0.1 mg/ml while ascorbic acid showed a minimum radical scavenging activity of 99.37% at 0.1 mg/ml and maximum activity of 99.52% at 0.5 mg/ml. This is an indication of a high scavenging capacity. Figure 3.63 display a graph of acetone extract of *Combretum molle*. The results revealed that this

extract displayed 99.64% DPPH inhibition at 5 mg/ml and 99.52% at 1 mg/ml while ascorbic acid showed a maximum activity of 99.64% at 5 mg/ml and a minimum activity of 99.37% at 1 mg/ml. This is also an indication of a high scavenging capacity for acetone extract. Figure 3.64 displays a graph of ethanolic extract of *Combretum molle*. The DPPH scavenging activity of this extract has reached up to 33.99% at 5 µg/ml and 20.04% at 1 µg/ml while ascorbic acid showed a maximum activity of 44.6% at 5 µg/ml and a minimum activity of 25.14% at 1 µg/ml. Ethanolic extract of *Combretum molle* also showed a significant and higher scavenging activity. The DPPH scavenging activity of chloroform extract of *Combretum molle* is shown on Figure 3.65. The graph displayed a maximum activity of 99.64% at 0.5 mg/ml and minimum activity of 99.31% at 0.1 mg/ml while ascorbic acid showed 99.52% at 0.5 mg/ml and 99.37% at 0.1 mg/ml. This is also a good indication of high scavenging activity. The graph that displayed the results of methanolic extract of *Acacia mearnsii* is shown on Figure 3.66. The results revealed that the maximum DPPH scavenging activity of this extract is observed at 99.39% for 0.5 mg/ml and 99.22% at 0.1 mg/ml while ascorbic acid showed a maximum activity of 99.52% at 0.5 mg/ml and a minimum activity of 99.37% at 0.1 mg/ml. The DPPH scavenging activity of acetone extract of *Acacia mearnsii* is displayed on Figure 3.67 and the graph revealed that this extract showed a maximum activity of 85.53% at 5 µg/ml and 59.95% at 1 µg/ml while ascorbic acid showed a maximum activity of 85.44% at 5 µg/ml and a minimum activity of 59.95% at 1 µg/ml. This plant extract showed the highest scavenging activity in comparison to other selected plant extracts and this is in agreement with its high phenolic content.

DPPH scavenging activity of ethanol extract of *Acacia mearnsii* is displayed on Figure 3.68. The results revealed that the maximum scavenging activity extract of *Acacia mearnsii* ethanol extract is observed at 79.75% at 5 mg/ml and minimum activity of 52.8% at 1 mg/ml while ascorbic acid showed a maximum activity of 90.06% at 5 mg/ml and a minimum activity of 70.1% at 1 mg/ml and this indicates an average scavenging capacity. Figure 3.69 displayed the graph of DPPH scavenging activity of chloroform extract of *Acacia mearnsii*. The graph revealed that its maximum scavenging activity is observed at 35.80% at 5 µg/ml and minimum activity of 27.49% at 1 µg/ml while ascorbic acid showed a maximum activity of 85.44% at 5 µg/ml and a minimum activity of 59.95% at µg/ml. This extract displayed a value that is not significant, indicating a lower

scavenging capacity. This is in line with its low phenolic and flavonoids content. All the scavenging activity graphs for both plants are displayed on the appendix.

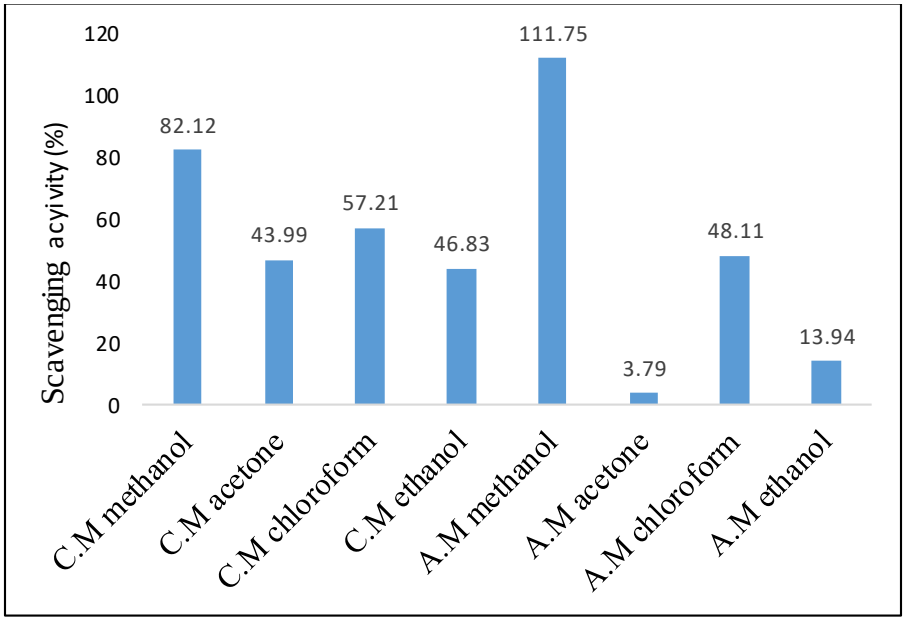

Figure 3.52: Free radical scavenging activity (IC_{50}) of *Combretum molle* and *Acacia mearnsii* in different solvent extracts.

Figure 3.52 showed the IC_{50} values of the selected plant extracts and these values represent the concentration of the test extract where the inhibition of test activity reached 50%. Therefore, this graph displayed the amount of each plant extract required for 50% inhibition of DPPH activity. The IC_{50} values were calculated using the equation of line obtained from the curve of each solvent of extract. The free radical scavenging activity of solvents on both *Combretum molle* and *Acacia mearnsii* showed this order: acetone > ethanol > chloroform > methanol. Therefore, both plants showed their highest scavenging activity in acetone extracts. The highest phenolic content in acetone extracts for both plants explains the highest scavenging acting of DPPH for both plants. Acetone extract also showed the highest flavonoids content in *Acacia mearnsii* and this might have contributed to its highest scavenging activity.

Table 3.15: Free radical (DPPH) scavenging activity of the two medicinal plants on four solvents of extracts

Names of plant	Solvent of extract	IC_{50} mg/ml
Combretum molle	Methanol	82.12
	Acetone	43.99
	Chloroform	57.21
	Ethanol	46.83
Acacia mearnsii	Methanol	111.75
	Acetone	3.79
	Chloroform	48.11
	Ethanol	13.94

3.7. Combination of copper chalcogenides with medicinal plant extracts

Combretum molle and *Acacia mearnsii* have been found to contain phenols, flavonoids, antioxidants, tannins, etc. The functional groups of *Combretum molle* have been identified using Fourier Transform Infrared spectroscopy. The vibrations include -C=C which is observed at 1594 cm^{-1}, -C-O observed at 1012 cm^{-1}, -C=O observed at 1705 cm^{-1} and -O-H observed at 3228 cm^{-1}. Similar vibrations were observed in *Acacia mearnsii* at 1605 cm^{-1}, 1015 cm^{-1}, 1696 cm^{-1}, and 3280 cm^{-1} responding to -C=C, -C-O, -C=O and -OH respectively.The oleylamine that was used as a capping molecule in the synthesis of copper chalcogenides nanoparticles has organic functional groups that are also observed in the FTIR spectra. Its major peaks are observed approximately at 2800 cm^{-1}, 1600 cm^{-1}, 1500 cm^{-1} and 1400 cm^{-1} corresponding to -CH, $-NH_2$, $-CH_3$ and –CN respectively.

FTIR spectra of copper chalcogenides and that of *Combretum molle* were separately done in comparison with the FTIR spectral analysis of copper chalcogenides combined with *Combretum molle* ethanol extracts and *Acacia mearnsii* ethanol extracts. Figure 3.53 (a), (b) and (c) depicts

FTIR spectra of copper selenide, copper sulphide and copper oxide, respectively. The spectra of copper selenide nanoparticles did not show any visible peak that can be assigned to organic groups. This might be due to their black color. Copper sulphide and copper oxide nanoparticles spectrum produced peaks that were observed approximately at 2845 cm^{-1}, 1618 cm^{-1} 1420 cm^{-1} and 1582 cm^{-1} corresponding to -CH from alkyl group, -NH from alkyl amine, -CN from alkyl amine and –NH stretching from amine group, respectively. Due to blackish color of copper selenide nanoparticles, the peaks produced were not as pronounced as those of copper oxide nanoparticles. All the observed functional groups emerged from the structure of olaylamine.

Figure 3.54 (a) shows the FTIR spectra of *Combretum molle* alone, (b) *Combretum molle* and copper selenide, copper sulphide, copper oxide. FTIR spectra of *Combretum molle* combined with copper chalcogenides nanoparticles revealed that the wide peak that was observed at 3228 cm^{-1} responding to the –OH group on the spectra of *Combretum molle* alone was reduced to a small peak indicating an interaction between plant extract and nanoparticles. The sharp peak that was observed at 1703 cm^{-1} corresponding to –C=O group in a spectrum of *Combretum molle* extract was not observed when the plant extract was combined with nanoparticles. The peak seemed to be displaced by a vibration observed at 2829 cm^{-1}, 2826 cm^{-1}, and 2844 cm^{-1} corresponding to $–CH_3$, CH_2 and CH group indicating an interaction of *Combretum molle* extract and (CuSe, CuS and CuO), respectively, from alkyl chain of oleylamine. Many intense peaks that were observed on the spectrum of *Combretum molle* extract between the range 1700 cm^{-1} to 1000 cm^{-1} were also displaced by two peaks on the spectra of the three chalcogenides (CuSe, CuS and CuO) that are combined with *Combretum molle*. These two peaks were observed at 1427 cm^{-1}, 1445 cm^{-1}, 1434 cm^{-1} corresponding to -C=C group; and 1016 cm^{-1}, 1007 cm^{-1}, 1013 cm^{-1} corresponding to C–O-C group corresponding to CuSe, CuS and CuO, respectively. This confirmed another interaction of plant extract and nanoparticles.

The significant peak that was observed at 1039 cm^{-1} corresponding to –OC group in the spectrum of *Combretum molle* extract became more intense when the active ingredient of *Combretum molle* was added to copper chalcogenide (CuSe, CuS and CuO) nanoparticles indicating more interaction between plant extract and nanoparticles. A new peak that was not observed at the spectrum of *Combretum molle* alone was observed on the spectra of the three chalcogenides (CuSe, CuS and

CuO) nanoparticles that are combined with *Combretum molle* at 2805 cm^{-1}, 2826 cm^{-1}, and 2832 cm^{-1}, respectively corresponding to –CH group.

FTIR spectrum of *Acacia mearnsii extracts* alone is shown on Figure 3.55(a) and the spectra of the combination of copper selenide, copper sulphide and copper oxide nanoparticles together with *Acacia mearnsii* are shown in Figure 3.55 (b). In the FTIR spectra of copper chalcogenide (CuSe, CuS and CuO) nanoparticles that are combined with the active ingredient of *Acacia mearnsii*, a new vibration was observed at 2321 cm^{-1}, 2351 cm^{-1}, and 2339 cm^{-1}, respectively. This vibration was not observed in the spectra of *Acacia mearnsii* alone, therefore it was assumed to have emerged from the interaction of plant extracts and copper chalcogenides nanoparticles. The broadness of the peak observed at 3280 cm^{-1} responding to the –OH group was reduced after the addition of copper chalcogenides nanoparticles suggesting an interaction between plant extracts and nanoparticles. The vibration of –C-O-C group that was observed at 1015 cm^{-1}, became more pronounced when the copper chalcogenides combined with the active ingredient of *Acacia mearnsii* the peak could have been enhanced by the presence of alkyl amine. A similar behavior as in *Combretum molle* spectra is observed whereby some significant peaks that were observed at lower wavenumber in the spectrum of *Acacia mearnsii* are displaced by one peak (567 cm^{-1}) in the spectra of copper chalcogenides nanoparticles that are combined with the active ingredient of *Acacia mearnsii* and this peak can be attributed to another interaction of copper chalcogenide (CuSe, CuS and CuO) nanoparticles and plant extracts.

Table 3.16: Functional groups present in nanoparticles, *Combretum molle* and *Acacia Mearnsii*

Name	Functional group of interest	Wavenumber (cm^{-1})
Oleylamine (capping molecule)	C-H	~2800
	N-H	~1600
	C-H	~1500
	C-N	~1400
Combretum molle	O-H	~3228
	C=O	~1705
	C=C	~1594
	C-O	~1012
Acarcia mearnsii	O-H	~3280
	C=O	~1696
	C=C	~1605
	C-O	~1015
Combretum molle + Copper chalcogenides	O-H	~3228
	CH_3-CH_2-CH	~2829
	C=C	~1427
	C-O-C	~1016
	OC	~1039
	C-H	~2805
Acacia mearnsii + Copper chalcogenides	O-H	~3280
	CH_3-CH_2-CH	~23395
	C=C	~1430
	C-O-C	~1015
	OC	~1040
	CH	~2800

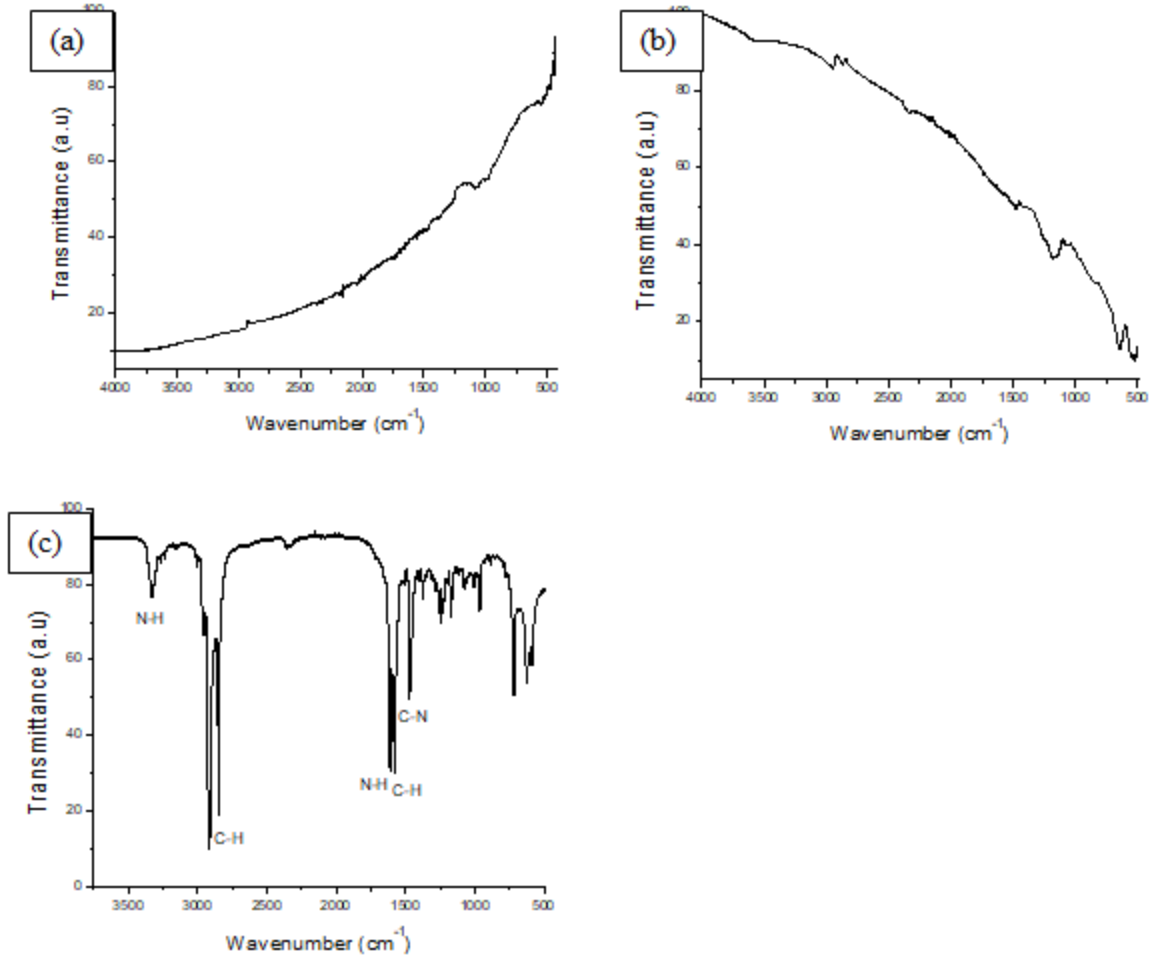

Figure 3.53: FTIR spectra of copper selenide (a), copper sulphide (b), copper oxide nanoparticles (c).

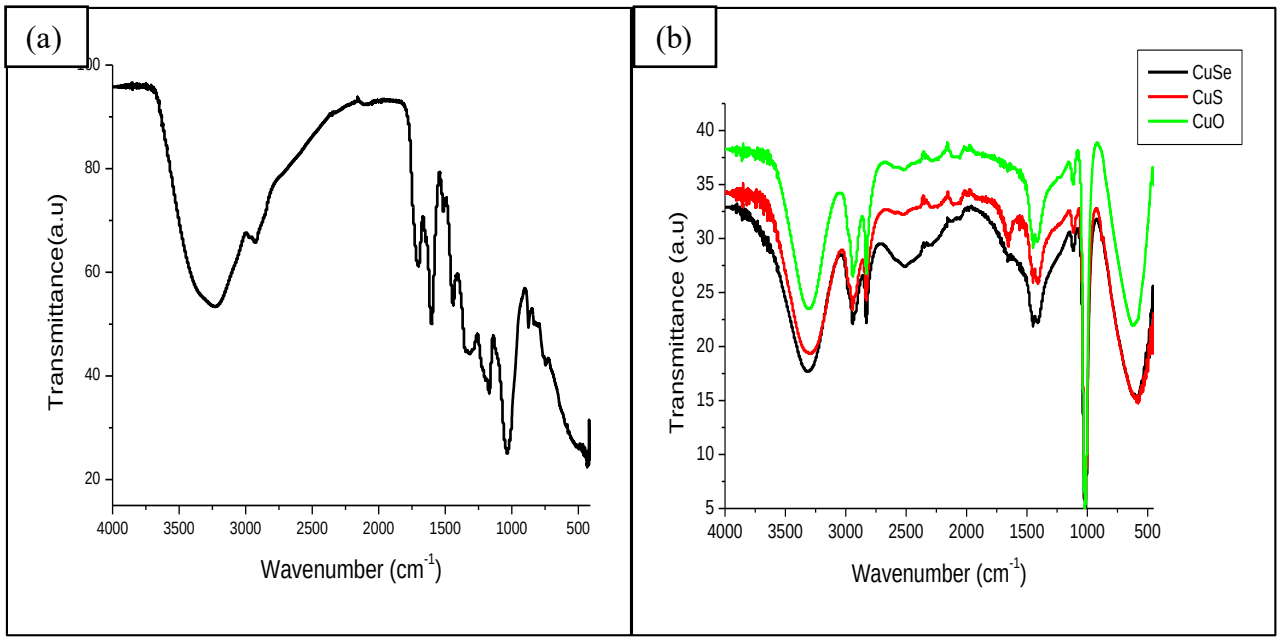

Figure 3.54: FTIR spectra of *Combretum molle* (a), *Combretum molle* and copper selenide, copper sulphide, copper oxide nanoparticles (b).

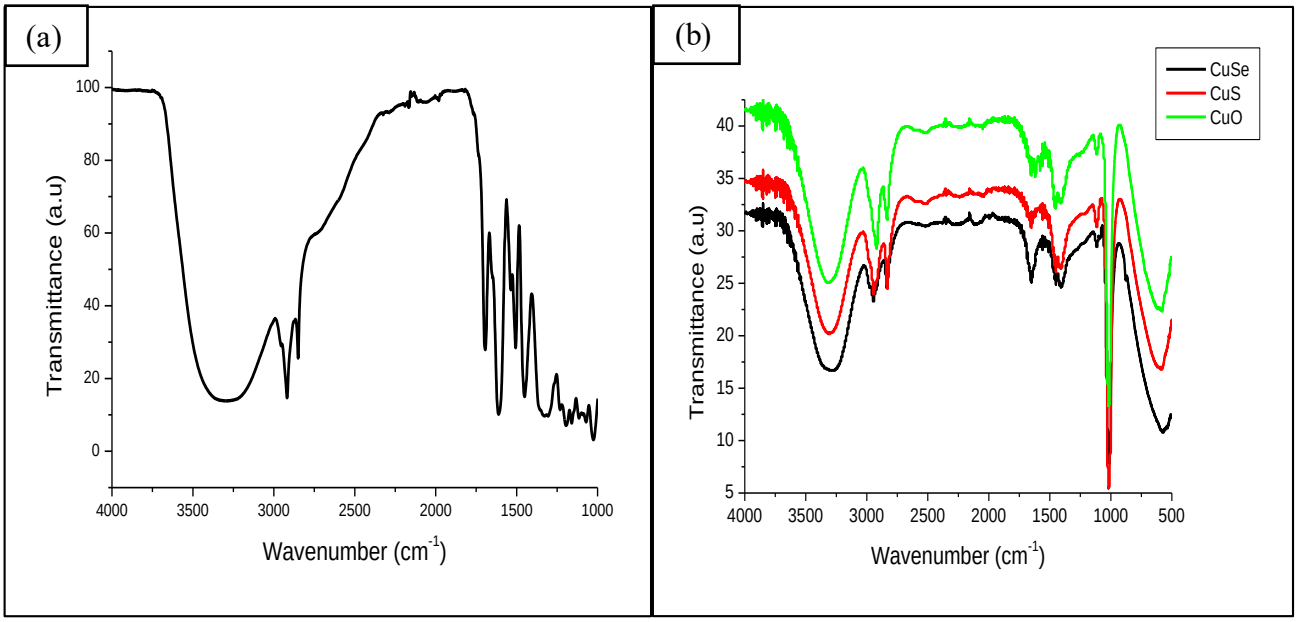

Figure 3.55: FTIR spectra of *Acacia mearnsii* (a), *Acarcia mearnsii* and copper selenide, copper sulphide, copper oxide nanoparticles (b).

3.8. Solubility test results

Generally, traditional medicinal products are designed in such a way that they become soluble in water for ingestion purposes and to avoid the use of toxic solvents. Therefore, it is a general practice to dissolve these products in water when testing them in living microorganism such as bacteria and fungi. Water is used to dissolve antimicrobial agents to ensure that the growth of living microorganisms is not inhibited by toxic solvents that are used to dissolve the antimicrobial agents as this would lead to in accurate results. It is therefore necessary to minimize the use of toxic solvents. The synthesized copper chalcogenides nanoparticles were water insoluble, they dispersed in organic solvents such as toluene. Since these nanoparticles were going to be tested for antimicrobial activity and mixed with plant extracts, it was therefore important to investigate their solubility in order to understand their surface properties and to adapt them to be water soluble prior to the antimicrobial study or to identify the suitable solvent for both nanoparticles and plant extracts. Five solvents namely; water, chloroform, ethanol, acetone and dichloroethane were selected for the solubility test. The results are shown in Figure 3.56. Amongst the five solvents, ethanol showed better solubility results for (copper selenide, copper sulphide, copper oxide, *Combretum molle* extracts and *Acacia mearnsii* extracts) solids compared to other four solvents (water, acetone, chloroform and dichloroethane) that were used in the study. The solvent ethanol was advantageous since it is miscible when added to water. Ethanol diluted with deionized water (0.17%) was therefore used to dissolve the antimicrobial agents (copper selenide, copper sulphide, copper oxide, *Combretum molle* extracts and *Acacia mearnsii* extracts) prior for antibacterial and antifungal activity test.

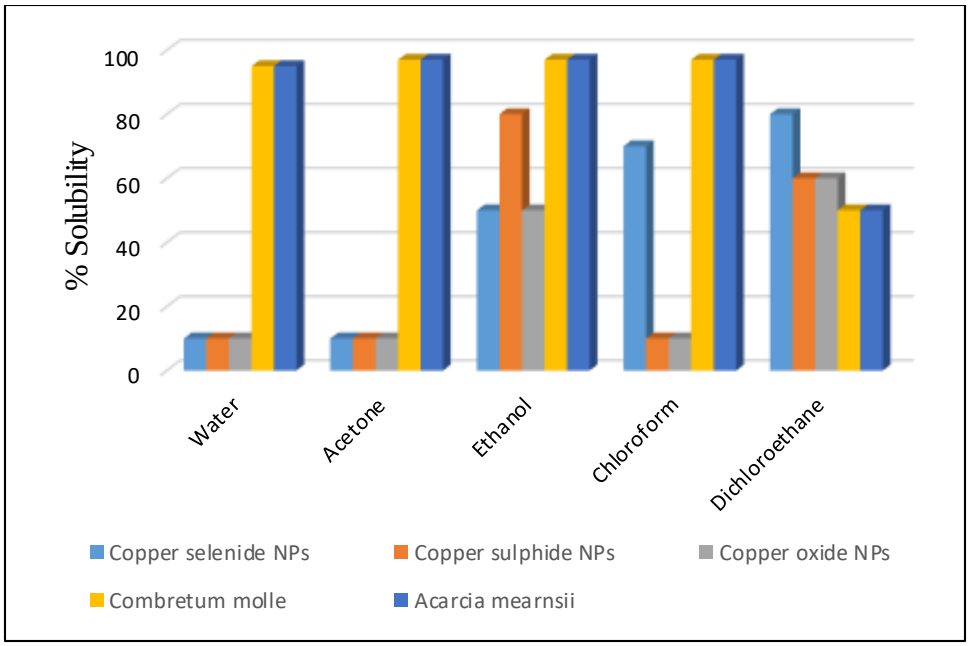

Figure 3.56: Solubility of copper selenide, copper sulphide, copper oxide nanoparticles, *Acacia mearnsii* and *Combretum molle*.

3.9. Antimicrobial study

Copper chalcogenide nanoparticles have been suggested for various potential applications, and antimicrobial has been listed among those applications (Honary *et al*. 2012). Disk diffusion and MIC methods have been used to test for the antibacterial and antifungal of the synthesized copper sulphide, copper selenide, copper oxide and the extracted active ingredients of *Combretum molle* and *Acacia mearnsii*. From the copper chalcogenides, $Cu_{0.87}Se$, Cu_9S_5, and CuO produced best properties and therefore were tested for antibacterial and antifungal. The bacterial species that were tested are namely: (1) *E. coli* which is a Gram-negative, rod-shaped bacterium that is commonly found in the lower intestines of warm-blooded organisms. In 1999, Mead *at al*. estimated that this organism was responsible for approximately 73, 000 cases of human illness and 61 deaths per year in the United States. (2) *P. aeruginosa* which is also a Gram-negative, oxidase-positive, rod that belongs to the family *Pseudomonadacae*. This organism is an opportunistic pathogen that causes nosocomial infections, and it can also be found in other environments through the world. *P. aeruginosa* typically infects the pulmonary tract, urinary tract, burns, wounds and causes blood infections. (3) *S. aureus* is a Gram-positive bacterium that is a member of the *Staphylococcaeceae*

which causes diseases such as bacteremia, endocarditis, toxic shock syndrome, sepsis and other metastatic infections. (4) *E. faecalis* is also a Gram-positive, non-motile, facultatively anaerobic bacterium inhabiting the gastrointestinal tracts of humans and other mammals. *E. faecalis* can also cause endocarditis and bacteremia, urinary tract infections, meningitis, and other infections in humans. *C. albicans* were used for testing the fungal activity of the selected agents. *C. albicans* are the predominant commensal fungus inhibiting the human oral activity, genito-urinary tract and leads to many candida infections.

A disk diffusion method was used to determine the sensitivity of the above-mentioned microorganisms that were used for antibacterial and antifungal study with respect to the antimicrobial agents (copper selenide, copper sulphide, copper oxide, *Combretum molle* extracts and *Acacia mearnsii* extracts). The sensitivity determination was carried out by measuring the inhibition zone which is the area of media where bacteria are unable to grow due to their sensitivity towards the antibacterial agent. A large zone of inhibition is an indication of high sensitivity of bacteria to the antibiotic drug. The results of plants extract according to their solvents of extracts, the synthesized nanoparticles and the combination of nanoparticles with plant extracts are listed in Table 3.17 below. Amongst the antibacterial agents that were used, *S. aureus,* showed more sensitivity towards the acetone extracts of *Combretum molle* by having the highest inhibition zone of 22 mm while this microorganism showed more resistance towards copper selenide nanoparticles by giving the smallest inhibition zone of 5 mm compared to other antibacterial agents. *P. aeruginosa,* showed maximal sensitivities towards copper oxide nanoparticles with inhibition zone of 24 mm while it showed some resistance towards chloroform extracts of *Combretum molle,* and chloroform extracts of *Acarcia mearnsii* showed. *E. coli* showed more sensitivity towards copper oxide with maximal inhibition zone of 28 mm, *Faecali* showed more sensitivity towards acetone extracts of *Combretum molle* with inhibition zone of 20 mm. *C. albicans* had more sensitivity towards ethanol extracts of *Combretum molle* with inhibition zone of 32 mm.

After the screening of the antimicrobial activity, a more accurate and quantitative method (MIC) was used to determine the lowest concentration of the antimicrobial agent to inhibit bacterial activity and the results are displayed on Table 3.18. The results revealed that all the microorganism that were tested were susceptible to all the plant extracts as well as the synthesized nanoparticles.

The growth was completely inhibited. Gram-negative (*E. coli)* revealed to be the most resistant microorganism towards the selected antimicrobial agents. In most cases, higher concentration of the antimicrobial agent was required to inhibit *E. coli* microorganisms in comparison to other microorganisms. Ethanol and methanol extracts of *Combrettum molle* showed highest antimicrobial activity towards *E. coli* with minimum inhibition concentration of 78.13 mg/µl. Gram-negative (*P. aeruginosa)* showed high sensitivity towards ethanol, methanol, acetone and chloroform extracts of *Combrettum molle,* ethanol and chloroform extracts of *Acacia mearnsii,* copper selenide, copper sulphide, copper oxide, copper selenide combined with *Combrettum molle,* and copper sulphide combined with *Combrettum molle* with a minimum inhibition concentration of 39.06 mg/µl. Gram-positive S. *aureus* revealed to be more sensitive towards copper selenide, copper sulphide, copper oxide and copper oxide mixed with *Acacia mearnsii* with a minimum concentration of 78.13 mg/µl. It showed some resistance towards ethanol extracts of *Acacia mearnsii* with 625 mg/µl for minimum inhibition with four times more folds compared to the previous. *E. faecalis* showed high resistance towards the selected antimicrobial agents, especially the chloroform extracts of *Combretum molle* which requires a minimum concentration of 10 000 mg/µl to inhibit its growth.

Nonetheless, this microorganism showed sensitivity towards the synthesized copper chalcogenides, copper selenide that has been combined with *Combretum molle*, copper oxide that has been combined with *Combretum molle,* copper selenide that has been combined with *Acacia mearnsii and* copper oxide that has been combined with *Acacia mearnsii* with a minimum concentration of 78.13 mg/µl for inhibition. *C. albicans* showed high sensitivity towards copper chalcogenides nanoparticles and the selected plant extracts that are mixed with copper chalcogenides nanoparticles with a minimum concentration of 78.13 mg/µl but lower sensitivity towards the selected plant extract that are not combined with nanoparticles. These results are also shown in Figure 3.57 and Figure 3.58 below. Mogashoa *et al*. (2017) reported on acetone extracts of *Combretum molle* to have highest antibacterial activity compared to ethyl acetate and dichloromethane. This concurs with the findings of this study. Masevesha *et al*. (2015) also confirmed the antibacterial activity of *Combretum molle*. In (2011), Njume *et al*. reported the highest bacterial activity of *Combretum molle* using acetone followed by ethanol and methanol. These findings are inconsistent with the findings of this study. Asres *et al*. (2006) observed the

highest bacterial activity of *Combretum molle* acetone extract against *E. coli*. Smith et al. (2003) reported on the inhibition of growth of *Escherichia coli* by *Acacia Mearnsii*. Olajuyigbe *et al.* (2012); Olajuyigbe *et al.* (2014) undertaken scientific validation of the antifungal and antibacterial activities of *Acacia mearnsii* for the treatment of microbial infections. Olajuyigbe *et al.* (2012) found antibacterial potentials of crude methanolic extract of *Acacia.mearnsii* against some bacteria of clinical importance in shigellosis. These studies proved that the solvent extracts selected for *Combretum molle* and *Acacia mearnsii* are all able to inhibit microbial growth but with different concentrations.

Table 3.17: Agar disk-diffusion test for screening the activity of the antimicrobial agents

Antimicrobial agent	solvent of plant extract	*E. Faecalis* Size of inhibition (mm)	*S. aureus* size of inhibition (mm)	*P. aeruginosa* Size of inhibition (mm)	*E. coli* Size of inhibition (mm)	*C. albicans* Size of inhibition (mm)
Combretum molle	ethanol	15	17	11	12	32
Combretum molle	methanol	14	19	14	16	28
Combretum molle	acetone	20	22	22	24	23
Combretum molle	chloroform	14	16	8	10	23
Acacia mearnsii	ethanol	12	12	23	11	18
Acacia mearnsii	methanol	6	7	23	14	22
Acacia mearnsii	acetone	16	13	11	20	11

Acacia mearnsii	chloroform	12	13	8	6	20
CuSe	ethanol	12	5	12	14	6
CuS	ethanol	8	9	24	25	5
CuO	ethanol	12	13	26	28	12
CuSe + *Combretum molle*	ethanol	18	18	24	26	24
CuS + *Combretum molle*	ethanol	12	14	20	22	22
CuO + *Combretum molle*	ethanol	16	18	11	14	28
CuSe + *Acacia mearnsii*	ethanol	10	10	13	12	22
CuS + *Acacia mearnsii*	ethanol	9	10	10	12	20
CuO + *Acacia mearnsii*	ethanol	9	9	15	16	27

Table 3.18: Determination of minimum inhibitory concentrations (MICs) of antimicrobial agents by broth dilution

Antimicrobial agent	solvent of plant extract	*E. faecalis* MIC (mg/µl)	*S. aureus* MIC (mg/µl)	*P. aeruginosa* MIC (mg/µl)	*E. coli* MIC (mg/µl)	*C. albicans* MIC (mg/µl)
Combretum molle	ethanol	312.5	156.25	39.06	78.13	156.25
Combretum molle	methanol	1250	156.25	39.06	78.13	156.25
Combretum molle	acetone	1250	156.25	39.06	778.13	156.25
Combretum mole	chloroform	10000	156.25	39.06	10000	156.25
Acacia mearnsii	ethanol	78.13	625	39.06	2500	78.13
Acacia mearnsii	methanol	312.5	78.125	156.25	156.25	78.13
Acacia mearnsii	acetone	78.13	156.25	39.06	312.5	625
Acacia mearnsii	chloroform	625	156.25	39.06	10000	78.13
CuSe	ethanol	78.13	78.13	39.06	5000	78.13
CuS	ethanol	156.25	78.13	39.06	312.5	78.13
CuO	ethanol	78.12	78.13	39.06	312.5	78.13

CuSe + *Combretum mole*	ethanol	78.13	312.5	39.06	312.5	78.13
CuS + *Combretum mole*	ethanol	156.25	156.25	78.125	312.5	78.13
CuO + *Combretum molle*	ethanol	78.13	156.25	39.06	312..50	78.13
CuSe + *Acacia mearnsii*	ethanol	78.13	312.5	78.13	625	78.13
CuS + *Acacia mearnsii*	ethanol	156.25	312.5	78.13	625	78.13
CuO + *Acacia mearnsii*	ethanol	78.13	78.126	78.13	625	78.13

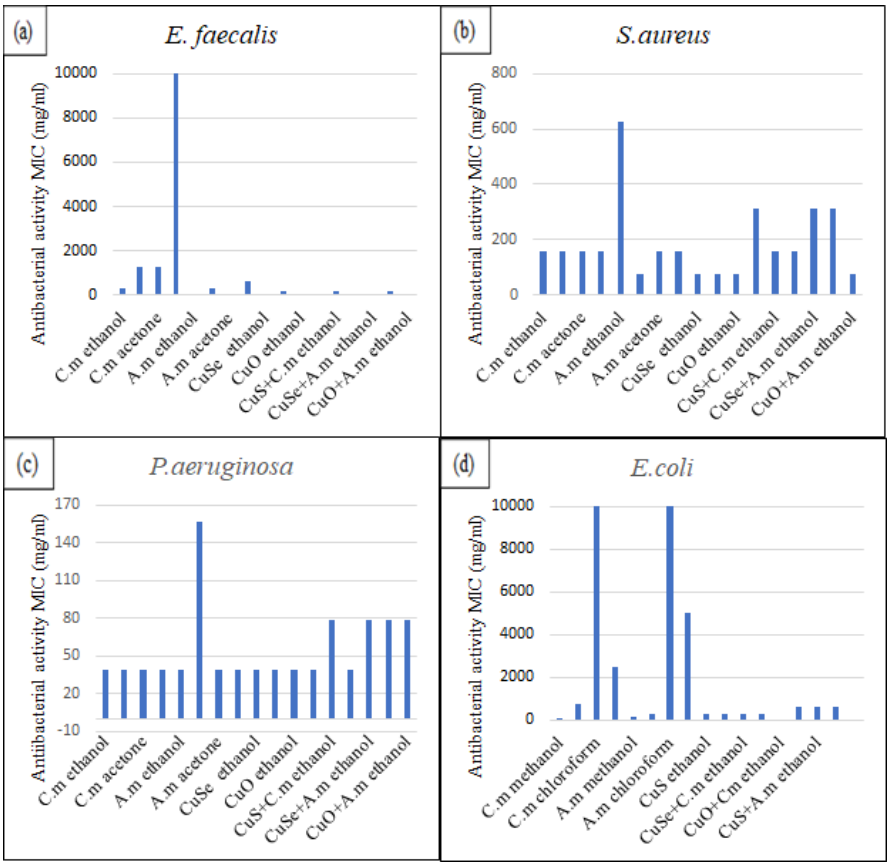

Figure 3.57: Antibacterial study of the synthesized copper chalcogenides and medicinal plant extracts against (a) *E. feacalis*, (b) *S. aureus*, (c) *P. aureginosa* and (d) *E. coli*

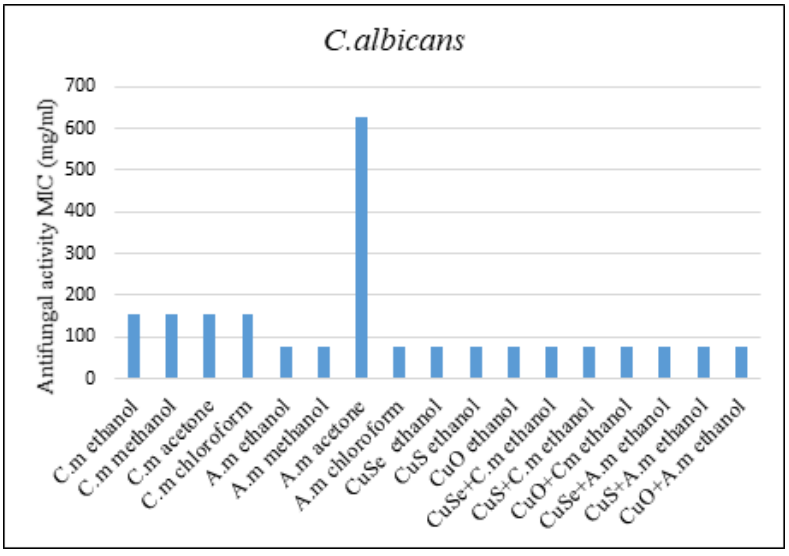

Figure 3.58: Antifungal study of the synthesized copper chalcogenides and medicinal plant extracts against *C. albicans*.

Chapter 4

Conclusions and Future work

4.1. Conclusions

Copper chalcogenides (CuSe, CuS and CuO) nanomaterials were synthesized by colloidal hot injection method in both OLA and TOP as capping agents. The nanomaterials prepared in OLA alone gave a wider variety of particle shapes compared to particles prepared in a mixture of OLA and TOP. OLA was therefore used as both solvent and capping agent to optimize other parameters including the reaction time, temperature and precursor concentration ratio in the synthesis of copper in their application. The effect of precursor concentration revealed a large effect on particle size. Nanomaterials synthesized using 1:1 precursor concentration ratio of Cu: Se/S gave best optical and structural properties compared to nanomaterials that were synthesized using 1:2 and 2:1 ratio. Copper oxide revealed a different behaviour from the two chalcogenides (Cu: Se/S) by showing its best optical and structural properties from nanomaterials that were prepared by precursor concentration ratio of 2:1 copper/oxide. Nonetheless, the effect of time was studied using 1:1 precursor concentration ratio.

The reaction time showed a large influence on the sizes and shapes but not much effect on the crystallinity and phase composition of the synthesized copper chalcogenides (CuSe, CuS and CuO) nanomaterials. The best optical properties of copper selenide and copper sulphide were found in nanomaterials that were synthesized for 30 minutes and 15 minutes for copper oxide. However, since the nanomaterials were going to be compared at the end of the study, 30 minutes was used as optimum reaction time for all the three copper chalcogenides when the effect of temperature was investigated. Copper selenide and copper sulphide nanomaterials decreased in size with the increased temperature up until 220 °C was reached, thereafter increased when the temperature was increased to 240 °C. This unusual trend was only observed on copper selenide and copper sulphide but not observed on copper oxide nanomaterials. However, copper oxide nanomaterials showed an increase in particle size with the increased reaction temperature. A difference in phase composition of the yielded nanoparticles was also observed when the reaction temperature was

changed. This confirmed that temperature affects particle size and shape as well as phase composition of crystals. 220 °C reaction temperature was deduced to be the optimum temperature for the synthesis of the three chalcogenides that were tested for their antibacterial study. During antibacterial study, copper oxide showed a higher sensitivity towards both Gram negative and positive bacteria and fungi compared to the two chalcogenides (CuSe/CuS) followed by copper selenide, then copper sulphide showed the least sensitivity amongst the three.

Extracts from *Combretum molle* and *Acacia mearnsii* medicinal plants collected with acetone showed the highest phenolic content. The flavonoid content was high in methanolic extract from *Combretum molle* whereas acetone extracts gave high content when collected from *Acacia mearnsii*. Acetone extracts showed the highest scavenging activity in both plants. The solubility of the synthesized nanoparticles was studied using water, acetone, ethanol, chloroform and dichloroethane. Ethanol was found to be the most suitable solvent and therefore, was used to dissolve and mix copper chalcogenide with the plant extract. Ethanol was also used in the antimicrobial study which was conducted against *Staphylococcus aureus, Enterococcus faecalis, Escherichia coli* and *Pseudomonas aeruginosa*, and *Candida albicans*. Amongst the plant extracts that were tested for antimicrobial activity, ethanol extracts from both plants showed the highest sensitivity towards all the microorganisms that were tested. Nonetheless, their sensitivity was found to be less than those of copper chalcogenides nanoparticles. Therefore, when the copper chalcogenides were mixed with plant extracts to enhance the performance of nanoparticles towards the selected microorganisms, the performance of the coordinated nanoparticles was not improved. It rather remained the same or performed worse towards certain microorganisms.

4.2. Future work

Following the conditions used for synthesizing nanoparticles and combining them with plant extracts as well as testing them against selected bacteria species, several observations were made bringing new information possible for expanding the work. Further work or tasks are outlined as follows:

- A further parameter optimization such as concentration of capping agent for the preparation of the copper chalcogenides nanocrystals especially copper selenide and copper sulphide

to get a narrower size distribution which can possibly improve their performance on their applications.

- To explore the effect of temperature on reaction temperatures above 240 ºC since the trend that was observed in temperatures below 220 ºC started to change when the temperature was increased to 240 ºC. This could be an indication of particle shape and size evolution of copper chalcogenides nanoparticles at temperature above 240 ºC.
- To do the toxicity study on the synthesized nanoparticles and plant extracts. This will apply for those with similar antibacterial activities and slightly improved activity.
- To synthesize the copper chalcogenides (copper selenide, copper sulphide, and copper oxide) with a green synthesis method using the same plant extracts as capping agents. These will be tested if their antibacterial activity improves or not as well as possible reduction of their toxicity.

4.3. References

ABASS, R. H; AHAR HALEEM, M; MAZIN HAMID, K; KADHIM, A; RID JAWAD, S., 2017. *Intern. J. of Comp. and Appl. Sci. IJOCAAS.*, **2**, pp.2399-4509.

ABDULLAEVA, Z; OMURZAK, E; MASHIMO, T., 2013. *World Academy of Sci. Eng. And Tech.*, **78**, pp.1057-1060.

AHMADI, T.S; WANG, L; GREEN, T.C; HENGLEIN, A; EL-SAYED, M.A., 1996. *Sci.*, **272**, pp. 1924-1926.

ALEJANDRA, C.B.G., LUIS, E.J. & JOSE, Y.M. 2008. *Mat. Character.*, **59**, pp. 204-212.

ALI, B. F; AL-SOU'OD, K. A; AL-FAR, R; JUDEH, Z., 2006. *Struct. Chem.*, **17**, pp. 423–429, 2006.

ALIVISATOS, A.P., 1996. *J. Phys. Chem.*, **100**, pp.13226–13239.

ALIVISATOS, A.P., 1997. *Endavour.*. **21**, pp.56-60.

ALIVISATOS, A.P; HARNS, A.L; LEVINOS, N.J; STEIGERWALD, M.L; HARRIS, L.E., 1998. *J. Chem. Phys.*, **89**, pp. 4001-4011.

AMELIA, M; LINCHENEAU, C; SILVI, S; CREDI, A., 2011. *Chem. Soc.*, **41**, pp.5728-5743.

ANIKEEVA, P.O; HALPET, J. E; BAWEDI, M.G; BULOVIC, V., 2007. *Nano. Lett.*, pp. 2169-2200.

AOKIE, T; AKASHI, T; AYABE, S., 2000. *J. Plant. Res.*, **113**, pp.475–488.

APARNA, Y; VENKATESWARA, K.R; SRINIVASA S.P., 2012. *J. of Nano and Electro. Phys.*, **4**, pp.3005-3014.

ARNOLD, T.H; DE WET, B.C., 1993. *Memoirs of the Botanic. Surv. Of. S. Africa.*, **26**, pp.397-423.

ASFAW, B; WHITE, T; LOVEJOY, D; LATIMR, B; SIMPSON, S., 1998, *Jr. Science.*, **284**, pp.629-635.

ASRES, K; MAZUMDER, A; BUCAR, F., 2006. *Ethiop. Med. J.*, **3**, pp.269-277.

BABA-MOUSSA, F; AKPAGANA, K; BOUCHER, P., 1999. *J. of. Ethnopharmacol.*, **66**, pp.335-338.

BALAZ, P; BOLDIZAROVA, E; GODOCIKOVA, E; BRIANCIN, J., 2003. *Mat. Lett.*, **57**, pp.1585-1589.

BALIS, N; DRACOPOULOS, V; BOURIKAS, K; LIANOS, P., 2013. *Electr. Acta.*, **9,** pp.246-252.

BALITSKII, O.A; SYTNYK, M; STANGL, J; PRIMETZHOFER, D; GROISS, H; HEISS, W., 2010. *ACS Appl. Mat. Inter.*, **6**, pp.17770–17775.

BAWENDI, M.G; STEIGERWALD, M.I; BRUS, I.E., 1990. *Annu. Rev. Phys. Chem.*, **41**, pp.477-496.

BHUSE, V.M; HANKARE, P.P; GARADKAR, K.M; KHOMANE, A.S., 2003. *Mater. Chem. Phys.*, **80**, pp.82–88.

BOHR, R.H; CHUN, S.Y; DAU, C.W; TAN, J.T; SUNG, J., 2009. *New Carbon Mater.*, **24**, pp.97-101.

BI, H; ZHAO, W; SUN, S; CUI, H; LIN, T; HUANG, F; XIE, X; JIANG, M., 2013. *Carbon.*, **61**, pp. 116-123.

BURDA, C; CHEN, X; NARAYANAN, R; El-SAYED, M.A., 2005. *Chem. Rev.*, **105**, pp. 1025-1102.

BRUS, L. E., 1985. *J. Phys. Chem.*, **90**, pp. 2555-2560.

BRUS, L. E., 1991. *Apply. Phys. A.*, **53**, pp.465-474.

BONFIELD, J.F; WELCH, S.A; ZHANG, H; EBERT, T.T; PENN, R.L., 2000. *Science.*, **289**, pp.751-754.

CAO, M; LIAN, H; HU, C., 2010. *Nanoscale.*, **2**, pp.2619-2623.

CAO, Y. C; WANG. J., 2004. *J. Am. Chem. Soc.*, **126**, pp.14336-14337.

CARUSO, F., 2000. *Chem. Europ. J.*, **6**, pp.413-419.

CHANG, C; YANG, M; WEN, H; CHERN, J., 2002. *J. Food Drug Analysis.*, **10**, pp.178-182.

CHEN, C; PEARSON, M. A., 1992. *Food Chem.*, **43**, pp.177-183.

CHEN, L; CHEN, Y. B; WU, L. M., 2004. *J. Am. Chem. Soc.*, **126**, pp.16334-16335

CHEN, S; FAN, Z; CARROL, D.L., 2002. *J. Phys. Chem. B.*, **106**, pp.10777-10781.

CHEN, X; YANG, J; WU, T; LI, L;LUO, W; JIANG, W; WANG, L., 2018. *Roy. Soc. Of Chem.*, **10**, pp.15130-15163.

CHENG, Z; WANG, S; WANG, Q; GENG, B., 2010. *Cryst. Eng. Comm.*, **12**, pp.144-149.

CHEON, J; JUN, Y; CHOI, J., 2006. *Angew. Chem. Int. Ed.*, **45**, pp.3414-3439.

CHESTNOY, N.; HARRIS, T.D.; HULL, R.; BRUS, L.E., 1986. *J. Phys. Chem.*, **90**, pp.3393-3399.

CHO, K.S; TALAPIN, D.V; GASCHELEV, W; MURRAY, C.B., 2005. *J. Am. Chem. Soc.*, **127**, pp.7140-7147.

CHOI, J; KANG, N; YANG, H.Y; KIM, H.J; SON, S.U., 2010. *Chem. Mat.*, **22**, pp.3586-3588.

COOK N. C; SAMMAN, S., 1996. *Nutritional Biochem.*, **7,** pp. 66- 76.

COUGHLAN, C; IBANEZ, M; DOBROZHAN, O; SINGH, A; COBOT, A; RYAN, K. M., 2017. *American. Chem. Soc.*, **17**, pp.5865-6109.

CORDOVA, R; GOMEZ, H; SCHREBLER, R; CURY, P; ORELLANA, M; GREZ, P; LEINEN, D; RAMOS-BARRADO, J. R; RIO, R. D., 2002. *Langmuir.*, **18,** pp.8647-8654.

COZZOLI, P.D; MANNA, L; CURRI, M.L; KUDERA, S; GIANNINI, C; STRICCOLI, M; AGASTIANO, A., 2005. *Chem.*, **17**, pp.1296-1306.

COZZOLI, P.D; SNOECK, E; GARCIA, M.A; GINNINI, C; GUAGLIARDI, A; CERVELLINO, A; GOZZO, F; HERNANDO, A; ACHTERHOLD, K; CIABANU, M; PARAK. F.G; CINGOLANI, R; MANNA, L., 2006. *Nano. Lett.*, **6**, pp.1966-1972.

DAJAN, V; MAJA, L; VERONOVSKI, N; SAMARDZIJA, Z; KRISTINA, Z; MIRAN, CEH.,2014. *Acta. Chin. Slov.*, **61**, pp.468-479.

DAS, S. K; PUTRA, N; THIESEN, P; ROETZEL, W., 2003. *ASME J. Heat Transfer.*, **125**, pp.567-574.

DEMORTIERE, A; PANISSOD, P; PICHON, B; POURROY, G; GULLON, D; DONNIO, B; BEGIN-COLIN, S.,2011. *Nanoscale.*, **3**, pp.225-232.

DE MELLO DONEGA, C; LILJEROTH, P; VANM EKELBERGH, D., 2005. *Small.*, **1**, pp.1152-1162.

DILENA, E; DORFS, D; GEORGE, C; MISTA, K; POVIA, M; GENOVESE, A; CASU, A; PRATO M; MANNA, L., 2012. *J. Mater. Chem.*, **22**, pp.13023–13031.

DORFS, D; HARTLING, T; MISZTA, K; BIGALL, N.C; KIM, M.R; GENOVESE, A; FALQUI, A; POVIA, M; MANNA, L., 2011. *J. Am. Chem. Soc.*, **133**, pp.11175–11180.

DU, W; QIAN, X; MA, X; GONG, Q; CAO, H; YIN, J., 2007. *Chem. Eur. J.*, **13**, pp.3241-3247.

DUNG, D. T; THU LE, T. T; FRIBOURG-BLANE, E; CHIEN DANG, M., 2011. *Nanosci. Nanotech.*, **2**, pp.15009.

ELOFF, J. N; FAMAKEN, J. O & KATERERE, D. R. P., 2005. *African Journ. Of. Biotech.*, **4**, pp.1161-1168.

ELOFF, J. N; KOTZE, M., 1998. *S. Afr. J. Bot.*, **68**, pp.62-67.

ELOFF, J. N., 1999. *S. A. Journ. Of Sci.*, **95**, pp.148-152.

ELOFF, J. N; KATERERE, D. R; McGAW, L.J., 2008. *J. Of. Ethnopharmacol.*, 119, pp.686-699.

EL-SAYED, M.A., 2004. *Acc. Chem.* Res., **37**, pp.326-333.

EVANS, H. T., 1979. *Jr. Science.*, **203**, pp.365-358.

EVY, C.L; EMENT, C.L; NEUMANN-SPALLART, M; HARAM AND, S.K; SANTHANAM, K.S.V., 1997. *Thin Solid Films.*, **302**, pp.12–16.

FENG, X.P; LI, Y.X; LIU, HB; LI, YL; CUI, S; WANG, N.,2007. *Nanotech.*, **18**, pp.145705-145711.

FRANKEL. E., 1995. *Intern. Conf. On food fact.*, **31**, pp.C6-2.

GAO, X.H; NIE. S.M., 2004. *Anal Chem.*, **76**, pp. 2406-2410.

GHEZELBASH, A; KORGEL, B. A., 2005. *J. Am. Chem. Soc.*, **21**, pp. 9451-9456.

GRACIA, S; LAKSHIMI, B; RAMANI, R., 2010. *Inter. Journ. Of comp. App.*, **16**, pp.256-280.

GRACIA, V.M; NAIR, P.K; NAIR, M.T.S., 1999. *J. Cryst. Growth.*, **203**, pp.113-124.

GREENWOOD, N.N; EARNSHAW, E. A., 1990. *Pergamon. Oxford.*, **12**, pp.1403-1542.

GROZDANOV, I., 1994. *Synthetic Metals.*, **63**, pp.213-216.

GUPTA, P; RAMRAKHIANI, M., 2009. *Open. Nano. J.*, **3**, pp.15-19.

HALAS, N.J; LAL, S; CHANG, W.S; LINK, S; NORDLANDER, P., 2011. *Chem. Rev.*, **111**, pp.3913–3961.

HARAM, S.K; SANTHANAM, K.S.V; NUMANN-SPALLAR M; LEVY-CLEMENT. C., 1992. *Mater Res Soc Bull.*, **27**, pp.1185-1191.

HARBONE, J. B; WILLIAMS, C. A., 2000. *Photochem.*, **55**, pp.481-504.

HARBOTTLE, J. E; FISCHER, S. B., 1982. *B. Nature.*, **299**, pp.139-140.

HEYDING, R.D; MURRAY CAN, R.M., 1976. *J. Chem.*, **54**, pp. 841-848.

HOLGATE, S. A., 2009, *CRC. Press.*, pp.177-178.

HU, C.D; CHINENOV, Y; KERPPALA, T.K., 2002, *Jr. Science.*, **9**, pp.789-798.

HU, X; ZRAZHEVSKIY, P; GAO, X., 2009. *Ann. Biomed. Eng.*, **37**, pp.1960-1966.

HU, J; BANDO, Y; GOLDBERG, D., 2005. *Small.*, **1**, pp.95-99.

HU, J; LI, L-S; YANG, W; MANNA, L; WANG, L-W; ALIVISATOS, A. P., 2001. *Sci.*, **292,** pp.2060-2063.

HUNG, K. L; LI, X. G; LIU, S. Q; TAN, N; CHEN, L. Q., 2008. *Ren. Ener.*, **33**, pp.186-192.

HONG, Z. S; CAO, Y; DENG, J. F., 2002. *Mater. Lett.*, **52**, pp.34–38.

HONARY, S; BARABADI, H; GHARAEIFATHABAD, E; NAGHIBI, F., 2012. *Dig. J. Nanomater. Bios*., **7**, pp.999-1005.

HRUBARU, M; ONWUDIWE, D, C; HOSTEN, E., 2015. *J. of Sulfur Chem.*, **37**, pp.37-74.

IIENIKHENA, P.A., 2008. *Physics Rev.*, **2**, pp.59-67.

IRYNA, S., 2018. *Bioproc. of Plant in Vitro. Syst.*, **146**, pp.154-155.

JAIN, K.K., 2003. *Expert Rev. Mol. Diagn*., **3**, pp.153-161.

JAIN, P.K; HUANG, X; El-SAYED, I; El-SAYED, M.., 2008. *Acc. Chem. Res*., **41**, pp. 1578–1586.

JESS, K; NICOLAS, G; RICHARD, R; ERIC, M., 2009. *Sol. Energy. Mat. Sol C.*, **94**, pp.12-16.

JIANG TANG, J: SEAN HINDS, S; KELLEY, S.O; SARGENT, E. H., 2008. *Chem. Mater.*, **20**, pp.6906-6910.

JIANG, C.W., 2004. *Journ. Of. Inorg. Biochem.*, **3**, pp. 497–501.

JIN. Z; HILDEBRANDT, N., 2012. *Trends. Biotechnol.*, **30** pp.394-403.

JIANLIANG C, YAN W, TIANYI, MA YUPING LIU, ZHONGYONG YUAN., 2011, *J. Nat. Gas. Chem.*, **20**, pp.669-676.

JUN, Y.W; LEE, J.H; CHOI, J.S., 2005. *J. Phys. Chem.* B., **109**, pp. 14795-14806.

KADHIM, A; AZHAR HALEEM, M; RUAA ABASS, H., 2016. *Adv. in Enviro. Biology.*, **10**, pp.43-54.

KADHIM, A; LEIQAA HAMEED, A; RAID JAWAD, S., 2015. *Eng. & Tech. Journal.*, **33**B, pp.172-177.

KAJIKAWA, K; TSUBOI, K., 2006. *Handai. Nanophotonics*., **2**, pp.3-316.

KALENGA, M. P; MOLOTO, N; MOLOTO, M. J; SIKHWIVHILU, L., 2012. *57th Annual Conference of South African Institute of Physics*., ISBN 987-1-86888-688-3.

KARPOVA, E. A; KHRAMOVA, E. P; FERSHALOVA, T. D., 2009. *Khim. Rast. Syara*., **2**, pp.105-110.

KATEROVA, Z; TODOROVA, D; TASHEVA, K; SERGIEV, I., 2012. *Inst. Of Plant Physio. And Genetics, Bulgarian Acad. of Sci*., **2**, pp.3-4.

KOLEVA, I. I; VAN BEEK, T. A; LINSSEN, J. P. H; DE GROOT, A; EVSTATIEVA, L. N., 2002. *Phytochem. Analys*., **13**, pp. 8-17.

KRIEGEL, I; RODRÍGUEZ-FERNÁNDEZ, J; WISNET, A; ZHANG, H; WAURISCH, C; EYCHMÜLLER, A; DUBAVIK, A; GOVOROV, A.O; FELDMANN, J., 2013. *ACS Nano*. **7**, pp.4367–4377.

KRYCH, J; GEBICKA, L., 2013. *Int J Biol Macromol.*, **58**, pp.148–153.

KWON, S. G; HYEON, T., 2011. *Small.*, **19**, pp.2685-2702.

LAKSHMIKUMAR AND, S.T; RASTOGI, M.A.C., 1994. *Sol. Ener. Mat. Sol. Cells.*, **32**, pp.7–19.

LANE, A.S; NINGTHOUJAM, R.S; SHARMA, S.J; VATSA, SR. K; PODE, R.B., 2010. *Int. Jour. Of Nanotech.*, **7**, pp.979-988.

LAPORNIK, B; WONDRA, A. G; PROŠEK, M., 2004. *J. Planar Chromatogr.*, **3,** pp.207–212.

LEE, S. M; CHO, S. N; CHEON, J., 2003. *J. Adv. Mater.*, **15**, pp.441-444.

LI, L. S; ALIVISATOS, A.P., 2003. *Phys. Rev. Letter*., **90**, pp.097402-097405.

LI, S; WANG, H; XU, W; SI, H; TAO, X; LOU, S; DU, Z; LI, L. S., 2009. *J. Colloidal Interface Sci.*, **330**, pp.483-487.

LI, W; R. ZAMANI, R; RIVERA. PILAR, R.G; PELAZ, B; IBANEZ, M; CADAVID, D; SHAVEL, A; ALVAREZ-PUABLA, R.A; PARAK, W.J; ARBIOL, J; CABOT, A., 2013. *J. Am. Chem. Soc.*, **135**, pp.7098 –7101.

LI, W; SHAVEL, A; GUZMAN, R; RUBIO-GRACIA, J; FLO, C; FAN, J; CADAVID, D; IBANEZ, M; ARBIOL, J; CABOT, A., 2011. *Chem. Commun*., **47**, pp. 10332-10334.

LI, H; ZHU, Y; AVIVI, S; PALCHIK, O; XIONG, J; KOLTYPIN, Y; PALCHIKB, V; GEDANKEN, A.., 2002. *J. Mater. Chem.*, **12**, pp.3723-3727.

LI, X; SHEN, H; LI, S; NIU, J; WANG, H; LI, L., 2010. *Chem.*, **20**, pp.923-928.

LIAO, X. H; WANG, H; ZHU, J.J; CHEN, H.Y. 2001. *Mat. Res. Bulletin.*, **36**, pp.2339-2346.

LIM, W. P; WONG, C. T; AN, S. I; LOW, H. Y; CHIN, W. S., 2006. *Chem. Mater.*, **18**, pp.6170-6177.

LIM, Y; CHOI, J; HANRATH, T., 2012. *Nanomat.*, **20**, pp.4-6.

LIN, Y; ZHANG, L; YOO, W; QIAN, H; DING, D; WU, W; JIANG, X., 2011. *ACS Appl. Mater. Interfaces.*, **3**, pp.995-1002.

LINK, S; EL-SAYED, M.A., 1999. *J. Phys. Chem.*, **103**. pp. 4212-4217.

LISIEKCKI, I; PILENI, M. B., 1993. *J. Am. Soc.*, **115**, pp.3887–3896.

LUI, X; WANG, X; SWIHART, M.T., 2013. *Chem. Mater.*, **25**, pp.4402–4408.

LIU, X.; WANG, F. 2007. *Chem. Ind. For. Prod.*, **27**, pp.43–48.

LUI, J; XUE, D., 2010. *Mater. Res. Bull.*, **45**, pp.309-313.

LIU, Z; ROBINSON, J.T; SUN, X; DAI, H., 2008. *J. Am. Chem. Soc.*, **130**, pp.10876–10877.

LUI, Z; XU, D; LIANG, J; SHEN, J; ZHANG, S; QIAN, Y.,2005. *J. Phys. Chem. B.*, **109**, pp. 10699-10704.

LONGANO, D; DITARANTO, N; CIOFFI, N; DI NISO, F; SIBILLANO, T; ANCONA, A; CONTE, A; DEL NOBILE, M. A; SBBATINI, L; TORSI, L., 2012. *Analyticl and Bioanalytical Chemistry*., **403**, pp.1179-1186.

LUTHER, J.M; JAIN, P.K; EWERS, T; ALIVISATOS, A.P., 2011. *Nat. Mater.*, **10**, pp. 361–366.

MAHAJAN, S; RANI, M; DUBEY, R. B; MAHAJAN, J., 2013. *Int. Jour. Of Latt. Reas. In Sci. and Nanotech*., **1**, pp.518-521.

MALIK, M. A; O'BRIEN, P; REVAPRASADU, N., 1999. *Adv. Mater.*, **11**, pp.1441-1444.

MANMEET, K; MUTHEA, K.P; DESPANDEB S.K; SHIPRA, C; SINGHD, J.B, NEETIKA, V; GUPTA, S.K; YAKHMI, J.V., 2011. *J Cryst Growth*., **289**, pp.670-675.

MANNA, L; SCHER, E.C; ALIVISASTOS, A.P., 2000. **122**, pp.12700-12706.

MASLENNIKOV, P. V; CHUPAKHINA, G. N; SKRYPNIK, L. N., 2013. *Seriya. Biologicheskaya*., **5**, pp.551-557.

MASOKO, P; ELOFF, J.N., 2007a. *S. A. Journ. Of. Botany*., **73**, PP.173-183.

MCDONALD, S; PRENZLER, P. D; AUTOLOVICH, M; ROBARDS, K., 2001, *Food Chem.*, **73**, pp.73-84.

McGAW, L.J; RABE, T; SPARG, S.G; JAGER, A. K; ELLOFF, J.N., 2001. *Journ. Of. Ethnopharmacol*., **75**, pp.45-50.

MEAD, P. S; SLUTSKER, L; DIETZ, V; McCAIG, L. F; BRESEE, J. S; SHAPIRO, C; GRIFFIN, P. M; TAUXE, R.V., 19991. *Emerg. Infect. Disease*., **5**, pp.607-625.

MILLIRON, D.J; HUGHES, S.M; CUI, Y; MANNA, L; LI, J; WANG, L.W; ALIVISATOS, A.P., 2004. *Nature*., **430**, pp.190-195.

MILMAN, V., 2002. *Acta Crystallogr., B*, **58**, pp.437-447.

MIRANDA, M; GELLIN, M; SIMONELLI, C; TIBERI, A; GIAMMANCO, M; GIORGETTI, F., 2013. *Appl. Phys. A.*, **110**, pp.829-833.

MNQIWU, K; XABA, T; MOLOTO, M. J; MUBIAYI, P. K; SIBOKOZA, S. B., 2017. *Mat. Lett.*, **199**, pp.28-31.

MOLOTO, N; RAY, S. S; MOLOTO, M. J., 2008. *J. of Nanosci. Nanotechnol.*, **12**, pp. 6181-6187.

MOLOTO, N; REVAPRASADU, N; MUSETHA, P. L; MOLOTO, M. J., 2012. *J. of Nanosci. and Nanotech*., **10**, pp.219-223.

MOLOTO, N; MOLOTO, M. J; CONVILLE, N. J; Ray, S. S., 2011. *J. of Cryst. Growth*., **324**, pp. 41-52.

MONTEIRO, O.C., NOGUEIRA, H.I.S., TRINDADE, T; MOTEVALLI, M. 2001. *Chem. of Mat.*, **36**, pp.2103-2011.

MORRIS, C.A; ANDERSON, M.L; STROUD, R.M; MERZBACHER, C.I; ROLISON, D, R., 1999. *Sci.*, **284**, pp.622-624.

MOSOKO, P ELOFF, J. N., 2005. *Afr. J. Trad. CAM.*, **4**, pp.231-239.

MULLER, A.H; PETRUSKA, M.A; ACHERMANN, M; WERDER, D.J; AKHADOR, E.A; KOLESKE, D.D; HOFFBAUER, M.A; KLIMOR, V.I., 2005. *Chem. Soc. Rev.*, **3**, pp. 1039-1044.

MUMME, W. G; SPARROW, G, J; WALKER, G.S., 1998. *Min. Mag.*, **52**, pp.323-330

MURPHY, C. J; SAU, T. K; GOLE, A. M; ORONDERFF, C. J; GAO, J; GOU, L; HUNYADI, S.E; Li, T., 2005. *J. Phys. Chem. B.*, **109**, pp.13857–13870.

MURRAY, C.B; SUN, S.H; DOYLE, H; BETLEY, T., 2001. *Mrs. Bull.*, **26**, pp.985-991.

MURRAY, C. B., NORRIS, D. J., BAWENDI, M. G., 1993. *J. Am. Chem. Soc.*, **115,** pp.8706-8715.

NAIR, P. K; NAIR, M. T. S., 1991. *J Phys. D.*, **24**, pp.450-453.

NARONGDET, W; PIYANUT, C; NARATIP, V; WISANU, P., 2011. *Energy. Procedia.*, **29**, pp.404-409.

NELWAMONDO, S. M. M; MOLOTO, M. J; KRAUSE, R. W; MOLOTO, N., 2012. *Mater. Res. Bull.*, 47, pp.4392-4397.

NJUME, C; AFOLAYAN, A; SAMIE, A; NDIP, R. N., 2011. *J. Health. Popul. Nutr.*, **5**, pp.438-445.

NOUMEDEM, J. A; MIHASON, M; KULATE, J. R; STEFAN, M; COJOCARU, D; DZOYEM, J. P; KUETE., 2013b. *Altern. Med.*, **18**, pp.13-26.

OLAJUYIGBE, O. O; AFOLAYAN, A. J., 2012. *In. Molecules.*, **17**, pp.2103–2118.

OLAJUYIGBE, O. O; AFOLAYAN, A. J., 2012. *Int. J. Mol. Sci.*, **13**, pp.4255–4267.

OLAJUYIGBE, O. O; AFOLAYAN, A. J., 2014. *J. Pure Appl. Microbiol.*, **8**, pp.1243–1257.

OLDENBURG, S.J; AVERITT, R, D; WESTCOTT, S.L; HALAS, N.J., 1998.*Chem. Phys. Lett*., **288**, pp.243–247.

OLUWAFEMI, O. S; REVAPRASADU, N., 2009. *Mater. Res. Soc. Symp. Proc*., **1138**, pp.12-19.

ONWUDIWE, D. C; HRUBARU, M; EBENSO, E. E., 2015. *Journ. Of Nanomat*., **7**, pp.9-15.

ORAVI, C. S; MANMEET, P. S; ONKAR, PARAMDEEP, S., 2009. C. *Sens. and Actuators B: Chem.*, **143**, pp.226-232.

OSTWALD, W., 1901. Z. *Phys. Chem.*, **37**, pp.385.

OWEN, R.W; MIER, W; GIACOSA, A; HULL, W.E; SPIEGELHALDER, B; BARTSCH, H., 2000. *Nat. Res. and the Enviro*., **21**, pp.460-480.

PALLET, A; HAND, K., 2010. *J. Antimicrob. Chemother*., **52**, pp.25-33.

PATHAN, H.M; LOKAHDE, C.D., 2004. *Bull. Mater*., **27**, pp.85-111.

PENG, X; MANNA, L; YANG, W; WICKHAM J; SCHER, E; KADAVANICH, A., 2000. *Nature*., **404**, pp.59-61.

PENG, Z.A; PENG, X.G., 2001. *J. Am. Chem. Soc*., **123,** pp.183-184.

PENG, X; WICKHAM. J; ALIVISATOS, A.P., 1995. *J. Am. Chem.*, **120**, pp. 5343-5344.

POURMORAD, F; HOSSEINIMEHR, S. J; SHAHABIMAJD, N., 2006. *S. Afr. J. Biotechnol*., **5**, pp.1142-1145.

PRAVEEN, K; ASHISH, W., 2012. *Sci. Techno. And Medicine Open Access*., **11**, pp.120-123.

QIN, A.M., FANG, Y.P., OU, H.D., LIU, H.Q; Su, C.Y. 2005. *Cryst. Grow. Design*., **5**, pp.855-860.

QUAN, Q; XIE, J; GAO, H; YANG, M; ZHANG, F; LIU, G; LIN, X; WANG, A; EDEN, H.S; LEE, S; ZHANG, G; CHEN, X., 2011. *Mol. Pharmaceutics*., **8**, pp.1669-16786.

RAGAD, F. A; YAHRA, T. A. A; EL-NAA, M. M., 2014. *Eur. J. Med. Chem.*, **82**, pp.206-520.

RAMAKRISHNAN NA, DRESCHER MJ, SHEIKHALI SA, KHAN KM, HATFIELD JS, DICKSON MJ, DRESCHER D. G., 2006. *Neuroscience*., **139**, pp.1417–1434.

RAMASAMY, K; MANEERPRAKORN, W; MALIK, M. A; O`BRIEN, P., 2010. *Phil. Trans. R. Soc. A.*, **368**, pp.4249-4260.

RAVI, C. S; MANMEET, P. S; ONKAR, PARAMDEEP, S., 2009. C. *Sens and Actuat B: Chem.*, **143**, pp.226-232.

RAY, P. C., 2010. *Chem. Rev.*, **110**, pp.5332-5365.

RAY, P; SRIVASTAVA, S.K., 2007. *Mater. Lett.*, **61**, pp. 1693-1697.

ROBEL, I; SUBRAMNIAN, V; KUNO, M; KAMAT, P.V., 2006. *J. Am. Chem. Soc.*, **128**, pp.2385-2393.

ROGACH, A. L; GAPONIK, N., 2008. *Spring. Wien. New York.*, **120**, pp. 73-100.

ROHMAN, A; RIYANTO, S; SAPUTRA, W. R; UTAMI, R., 2010, *Int. Food. Ress. J.*, **17**, pp.97-106.

ROKOVICH, Y. P; DONEGAN, J. F., 2008. *Springer-Verlag Wien.*, **90**, pp.256-258.

ROY, P; SKRIVSTAVA, S. K., 2007. *Mater. Lett.*, **62**, pp.1693-1697.

SAGADE, A. A, SHARMA, R., 2008. *Sensor Actuat B-Chem.*, **133,** pp.135-143.

SAFEKORDI, A. A; ATTAR, H; GHORBANI, H. R., 2011. *Chem. Eco. And Enviro Sci.*, pp.346-350.

SAGADE, A; SHARMA, R., 2008. *Sens. Actuators B.*, **133**, pp.135-143.

SALDANHA, P.L; BRESCIA, R; PRATO, M; Li, H; POVIA, M; MANNA, L; LESNYAK, V., 2014. *Chem. Mater.*, **26**, pp.1442–1449.

SALA, I.M; XAVIER, G.D; PANALD, M., 2002. *Fourth coming American Econo. Rev.*, **18**, pp.116-119.

SANG, B; SHAFARMAN, W.N; BIRKMIRE, R.W., 2002. IEE *Photovolt. Special. Confr.*, **29**, pp.632-635.

SANTRA, S; YANG, H; HOLLOWAY, P.H; STANLY, J.T; MERICLE, R.A., 2005. *J. Am. Chem. Soc.*, **127**, pp.1656-1657.

SANTRA, S; WANG, K.M; TAPEC, R; TAN. W.H., 2001. *J. Biomed. Opt.*, **6**, pp.160-166.

SAU, T.K; ROGACH, A. L; JAECKEL, F; KLAR, T. A; FELDAMAN, N., 2010. *J. Adv. Mater.*, **22**, pp.1805–1825.

SAVAGODO, O., 1998. *Sol. Ener. Mat. Sol. Cells*., **25**, pp.361-388.

SCHAFER, A; KOUWITZ, M; AHLRICHS, R., 1996. *J. Chem. Phys*., **104**, pp.7113-7122.

SCHUCK, P., 1997. *Annu. Rev. Biophys. Struct*., **26**, pp.541–566.

SEPULVEDA, B; ANGELOME, P.C; LECHUGA, L.M; LIZ-MARZAN, L., 2009. *Nano Today.*, **4**, pp.244–251.

SHAFIZADE, K. D; IVANOVA, I. V; KAIZINETS, M.M., 1978. *Thin. Sol. Films*., **55**, pp.211-220.

SHEN, H; WANG, H; YUAN, H; MA, L; LI, L.S., 2012. *Cryst. Eng. Comm.*, **14**, pp. 555-560.

SHEN, X.P; ZHAO, H; SHU, H.Q; ZHOU, H; YUAN, A.H., 2009. *J. Mater Chem.*, **70**, pp.422-427.

SHERRY, L.J; CHANG, S.H; SCHATZ, G.C; VAN DUYNE, R.P; WILEY, B.J; XIA, Y., 2005. *Nano. Lett.*, **5**, pp. 2034-2038.

SHEVCHENKO. E.V; TALAPI, D.V; SCHNABLEGGES, H; KORNOWSKI, A; FESTIN, O; SVEDLINDH, P; HAASE. M; WELLER, H., 2003. *J. Am. Chem.*, **125**, pp.9090-9101.

SHI, J; HO, C. T; SHAHIDI, F., 2011. *J. Agric. Food Chem.*, **54**, pp.3617–3624.

SIBIYA, N. P; MOLOTO, M. J., 2014. *Chalcogen. Lett.*, **11**, pp.577-588.

SIBOKOZA, S. B; MOLOTO, M. J; MOLOTO, N; SIBIYA, P.N., 2017. *Chalcogen. Letts*., **14**, pp.68-78.

SIGMAN, M. B; GHEZELBASH, J. A; HANRATH, T; SAUNDERS, A. E; LEE, F; KORGEL, B. A., 2003. *J. Am. Chem. Soc*., **125**, pp.16050-16057.

SKIRMA, A; VITALIJUS, J., 2012. *Mat. Sci-Medzg*., **18**, pg.112-118.

SMITH, A. M; SHUMING, N., 2010. *Acc. of chem. Res*., **43**, pp.190-200.

SMITH, A.H; IMLAY, J.A; MACKIE, R.I., 2003. *Appl. Environ. Microbiol*., **69**, pp.3406–3411.

SON, D; YOU, C; KI, T., 2009. *Appl. Surf. Sci*., **255**, pp.8794-8797.

STOIMENOV, P.K; KLINGER, R.L; MARCHIN, G.L; KLABUNDE, K.J., 2002. *J Mat. Chem.*, **18**, pp.6679-6686.

SUGIMOTO, T., 2001. *J. Am. Chem. Soc*., **93**, pp.209-216.

SULEIMAN, M; MAOUSA, M; HUSSEIN, A; HAMMOUTI, B; HADDA, T. B; WARAD, I., 2013. *J. Mat. Environ. Sci*., **4**, pp.792-797.

SUN, X; LIU, Z; WELSHER, K; ROBINSON, J; GOODWIN, A; ZARIC, S; DAI, H., 2008. *Nano Res*., 1, pp.203–212.

SUN, J; WANG, L.W; BUHRO, W.E., 2008. *J. Am. Chem. Soc*., **130**, pp.7997-8005.

SWANKAR, S.C; SINGH, S.C; GOPAL, R., 2010. *Int. Jour. Of. Nanotech.*, **8**, pp.571-582.

SWAPNIL, B; AMBANDE, R.S; MANE, S.S; KALE, S.H; SONAWANE, ARIF V; SHAIKHHAN, S.H., 2006. *App. Surf. Sci*., **253**, pp.2123-2126.

SYED, A., 2012. *J. Intern. Med. Sci. Acad.*, **25**, pp.187-192.

TACHAN, Z; SHALOM, M; HOD, L; RUHLES, S; TIROSH, S; ZABAS, H., 2010. *J. Phys. Chem.*, 115, pp.6162-6166.

TENG, X; YANG, H., 2005. *Nano. Lett*., **5**, pp.885-891.

TETERIS, J., 2003. *Curr. Opin. in Sol. State and Mat. Sci*., **7**, pp.127-134.

TIAN, S. S, JIANG, F. S; ZHANG, K., 2014. *Fitoterapia*., **92**, pp.34-40.

TOSUN, M., ERCISLI, S., SENGUL, M., OZER, H., POLAT, T., 2009, *Biol. Res*., **41**, pp.175-181.

UNDERWOOD, D.F; KIPPENY, T; ROSENTHAL, S.J., 2001. *J. Phys. Chem. B*., **105**, pp.436-443.

USTIS, S; EL-SAYED, M.A., 2006. *Chem. Soc. Rev*., **35**, pp. 209-217.

VANAJA, M; RAJESHKUMAR, S; PAULKUMAR, K; GNANAJOBITHA, G; MALARKODI, C; ANNADURAI, G., 2013. *Adv. in App. Sci. Res*., **4**, pp.50-55.

VOORHEES, P. W., 1985. *Journ. of Statis. Phys*., **38**, pp.231-252.

WAGNER, H; BLADT, S., 1996. *Plant. Drug. Anal*., **2**, pp.204-247.

WANG, H; ZHU, J.J; ZHU, J.M; CHEN, H.Y., 2002. *J. Phys. Chem B*., **106**, pp.3848-3854.

WANG, Y; ZHUKOVSKYI, M; M; TONGYING, M.P; TIAN, Y; M. KUNO, M., 2014. *J. Phys. Chem. Lett*., **5**, pp.3608–3613.

WANG W. Z, YAN P, LIU FY, XIE Y, GENG Y., 1998. *J. Mater. Chem.*, **8**, pp.2321.

WANG, Y; HERON, N., 1991. *J. Phys. Chem.*, **95**, pp.252-532.

WANG, W.Z; GENG, Y; YAN, P; LIU, F.Y; XIE, Y; QIAN, Y.T., 1999. *J. Am. Chem. Soc*., **121**, pp.4062-4063.

WILEY, B.J; XIONG, Y.J; CHEN, J.Y; LI, Z.Y; YIN, Y.D; XIA, Y.N.,2005. *Angew. Chem. Int. Ed*., **117**, pp.8127-8131.

WOLF, A; KODANEK, T; DORFS, D., 2015. *Nanoscale*., **7**, pp.19519-19527.

WU, C; SHI, J.-B; CHEN, Y.-C; CHEN, Y.-T; LIN, P.-F; WU, S.-Y., 2008. *Mat. Lett*., **62**, pp.1074-1077.

WU, T; HE, M; ZANG, X., 2013. *Biochim. Biophys. Acta*., **11**, pp.2751– 2756.

XIAO, G; NING, J; LUI, Z; SUI, Y; WANG, Y; DONG, Q; TIAN, W; LUI, B; ZOU, G; ZOU, B., 2012. *Cryst. Eng. Commun*., **14**, pp.2139-2141.

XIE, Y; RIEDINGER, A; PRATO, M; CASU, A; GENOVESE, A; GUARDIA, P; SOTTINI, S; SANGERGORIO, C; MISZTA, K; GHOSH, S; PELLEGRINO, T; MANNA, L., 2013. *J. Am. Chem. Soc*., **135**, pp.17630–17637.

XIONG, Y; LIU, C; WANG, J; HAN, J; ZHAO, X., 2017. *Optics. Epress*., 25, pp.6874-6882.

XU, J; ZHANG, W.X; YANG, Z.H; DING, S.X; ZENG, C.Y; CHEN, L.L; WANG, Q; YANG, S.H.,2009. *Adv. Funct. Mater*., **19**, pp.1759–1766.

YAMAGUCHI, T; YAMAMOTO, Y; TANAKA, T; DEMUZI, Y; YOSHIDA, A., 1996. *Thin Solid Films*., **281**, pp.375-378.

YAMUKYAN, M.H; MANUKYAN, K.V; KHARATYAN, S.L., 2008. *Energy. Proced*., **137**, pp.636-642.

YANG, Z; XIULI, H; JIANPING, L; HUIGANG, Z; XIAOGUANG, G., 2007. *Sensor.*, **128**, pp.293-298.

YANG, L.J; LI, Y.B., 2006. *Analyst.*, **131**, pp.394-401.

YAO, W; YU, S; ZHOU, Y; JIANG, J; WU, Q; ZHANG, L., 2005. *J. Phys. Chem. B.*, **109**, pp.14011-14016.

YU, R; REN, T; SUN, K.J; FENG, Z.C; LI, G.N; LI, C., 2009. *J. Phys. Chem. C*., **113**, pp.10833-10837.

ZEYU, Z; TAN, C; YAXIN, Z; HONGTAO, W; WENJING, L., 2014. *Biores. Techno*., **4**, pp.84-95.

ZHANG, H; ZHANG, Y; YU, J; YANG, D., 2008. *J. Phys. Chem. C*., **112**, pp.13390-13394.

ZHANG, J; ZHANG, Z., 2008. *Mat. Lett*., **62**, pp.2279-2281.

ZHANG, X; HUANG, H; ZHAO, X., 2015. *J. Funct. Foods*., **14**, pp.144-153.

ZHANG, W. X; ZHANG, X. M; ZHANG, L; WU, J.X; HUI, Z.H., 2000. *Inorg. Chem.*, **39**, pp.1838-1839.

ZHANG, Y; QIAO, Z.P; CHEN, X. M., 2002, *J. Mater. Chem.*, **12**, pp.2747-2748.

ZHANG, Y; WIGGINGS, B.E; LAWRENCE, C; PETRIK, J; IVASHUTA, S; HECK, G.,2012. *BioMed. Cent*., **14**, pp.30-34.

ZHAO, S.M; HAN, S.A., 2010. *J. Chin. Chem. Soc*., **57**, pp. 1353-1360.

ZHAO, Y; PAN, H; LOU, Y; QIU, X; ZHU, J; BURDA, C., 2009. *J. Am. Chem. Soc*., **131**, pp.4253–4261.

ZHENG, W; WANG, Y. S., 2001. *J. Agric. Food. Chem.***, 49**, pp.5165-5170.

ZHU, J; LI, D; CHEN, H; YANG, X; LU, L; WANG, X., 2004. *Mater. Lett.*, **58**, pp.3324-3327

ZIEGLER, C; EYCHMULLER, A., 2011 *J. Phys. Chem. C.*, **115**, pp.4502–4506.

ZLOTEK, U; MIKULSKA, S; NAGAJEK, M; SWIECA, M., 2016. *Saudi. Journ. Of. Bio. Scie.*, **23**, pp.628-633.

ZOU, J; ZHANG, J., ZHANG, B; ZHAO, P; HUANG, K., 2007. *Mat. Lett.*, **61**, pp. 5029-5032.

ZOU, R; Wu, X; HAO, X; ZHOU, F; Li, H; RAO, W., 2008. *Instrum. Methods B.*, **266**, pp.599–603.

Appendix

Table 3.19: Absorbance of gallic acid standards

Concentration (µg/ml)	Absorbance
0	0.03
10	0.074
20	0.112
30	0.141
40	0.169
50	0.202
60	0.230
80	0.293
100	0.349

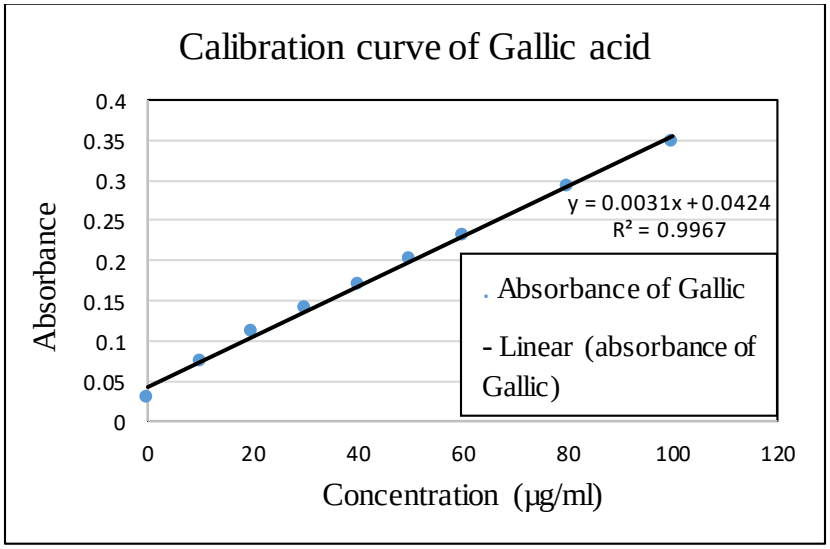

Figure 3.59: Calibration curve of gallic for total phenolic content determination.

The concentration of phenols in plant samples was determined by using an equation that was obtained from standard gallic acid graph. The equation is given below:

Table 3.20: Absorbance of quercetin standards

Concentration (µg/ml)	Absorbance
0	0.000
10	0.100
20	0.169
30	0.250
50	0.382
80	0.601
100	0.730

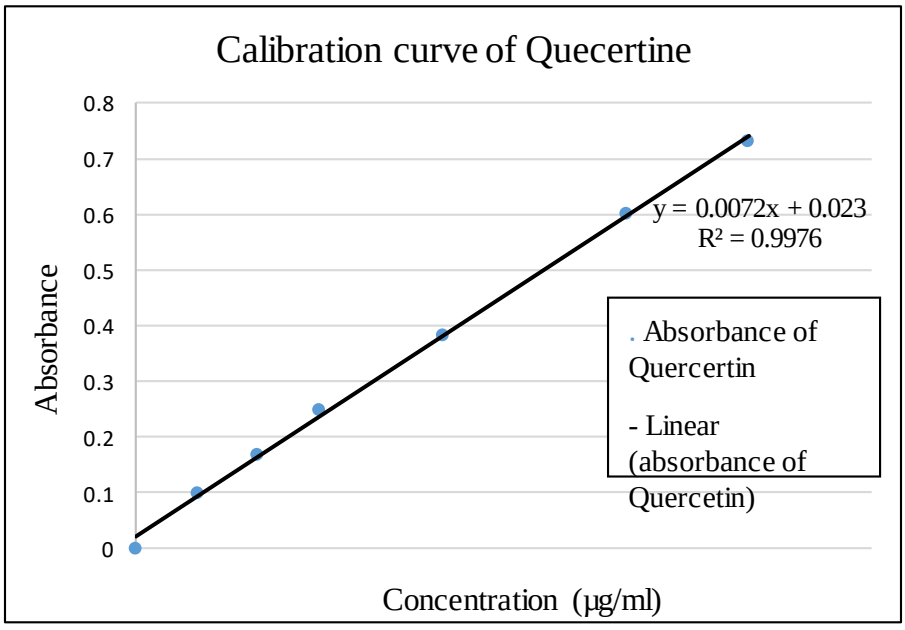

Figure 3.60: Calibration curve of quercetin for total flavonoids content determination.

Table 3.21: Absorbance of DPPH standards

Concentration (µg/ml)	Absorbance
0	0.085
40	0.447
80	0.894
100	1.065

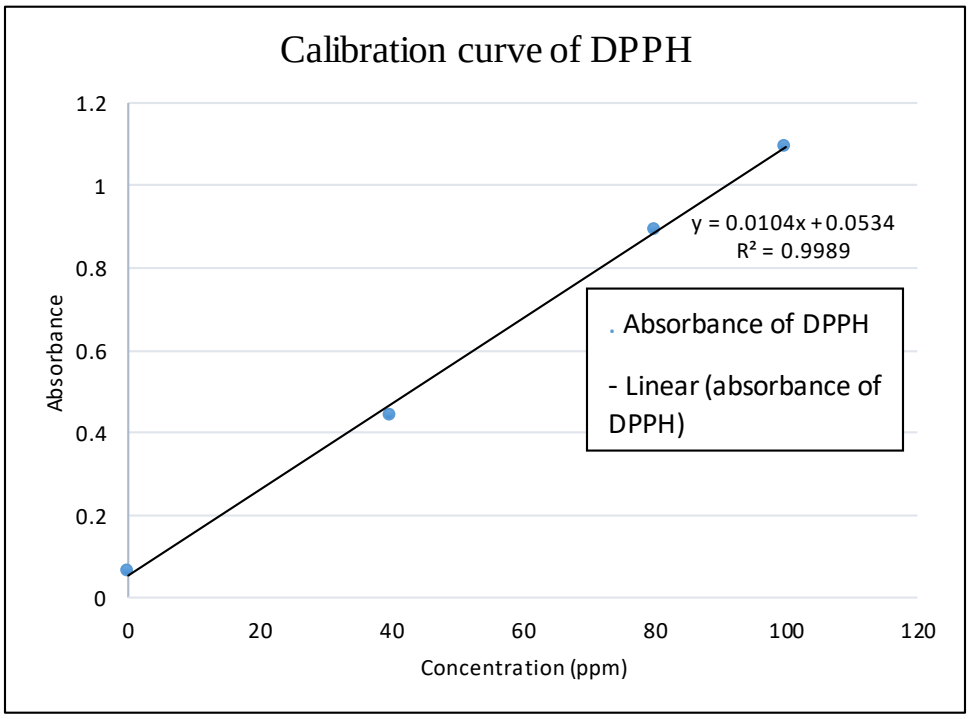

Figure 3.61: Calibration curve of DPPH for antioxidant content determination.

The concentration of antioxidant in plant samples was determined by using an equation that was obtained from standard DPPH graph. The equation is given below:

$y = 0.0104x + 0.0534$

Where,

y = absorbance

x = DPPH concentration (µg/ml)

m = slope=0.0104

x = y -0.0534/ 0.0104

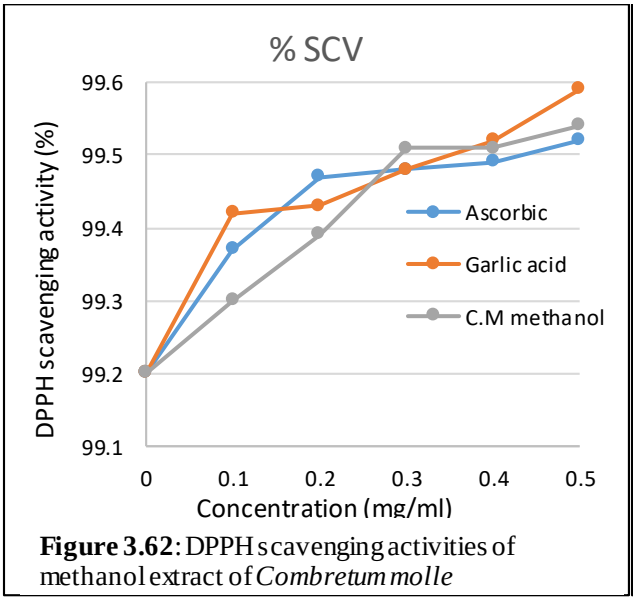

Figure 3.62: DPPH scavenging activities of methanol extract of *Combretum molle*

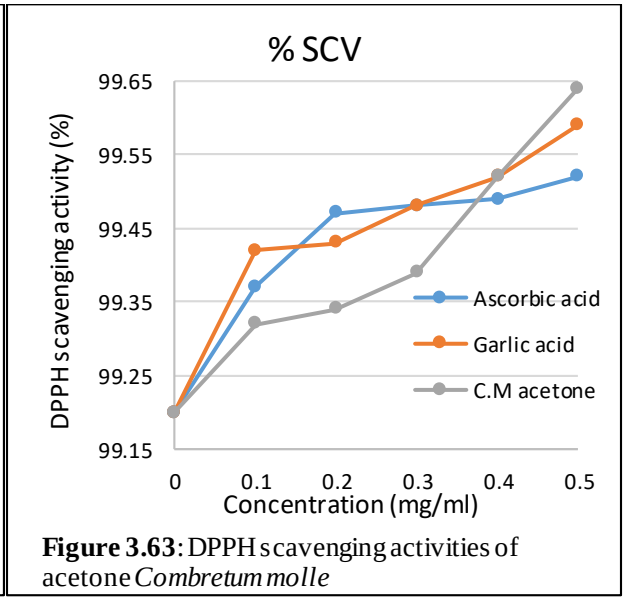

Figure 3.63: DPPH scavenging activities of acetone *Combretum molle*

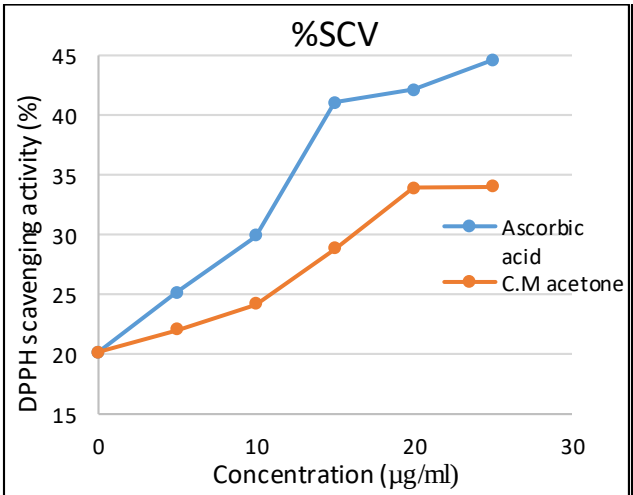

Figure 3.64: DPPH scavenging activities of ethanol extract of *Combretum molle*

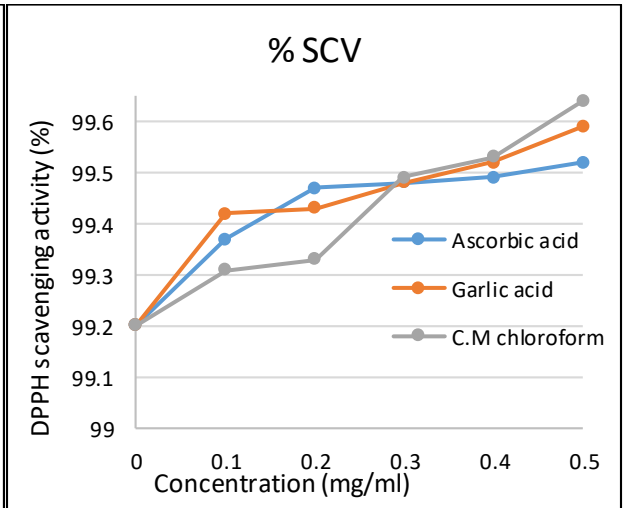

Figure 3.65: DPPH scavenging activities of chloroform *Combretum molle*

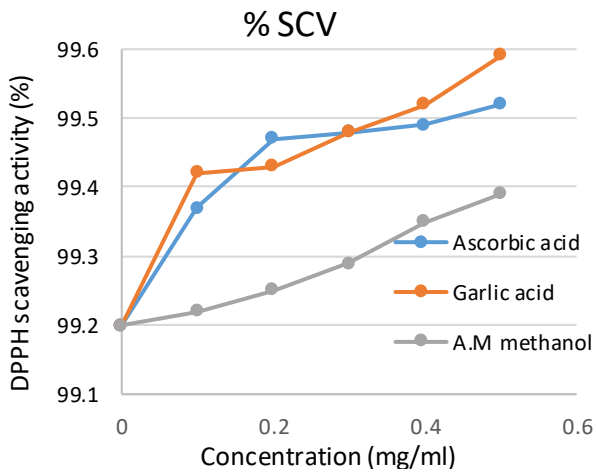

Figure 3.66 : DPPH scavenging activities of methanol extract of *Acacia mearnsii*

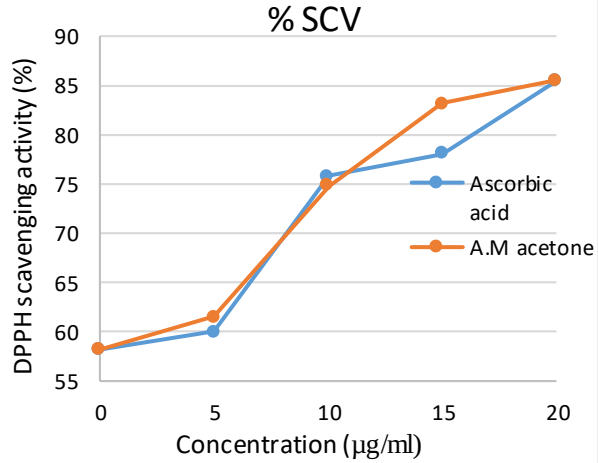

Figure 3.67: DPPH scavenging activities of acetone extract of *Acacia mearnsii*

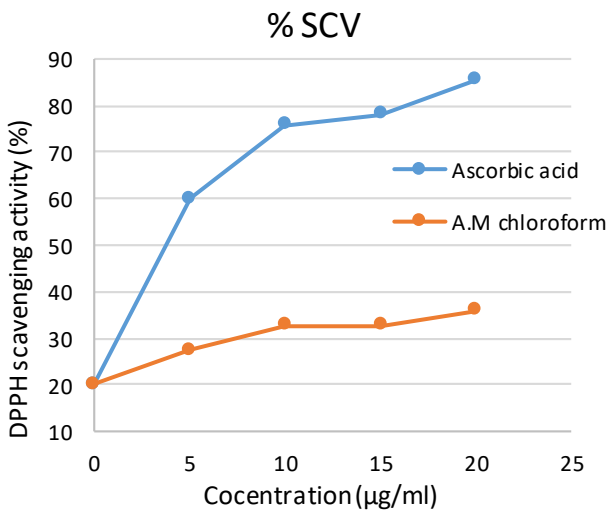

Figure 3.68: DPPH scavenging activities of chloroform extract of *Acacia mearnsii*

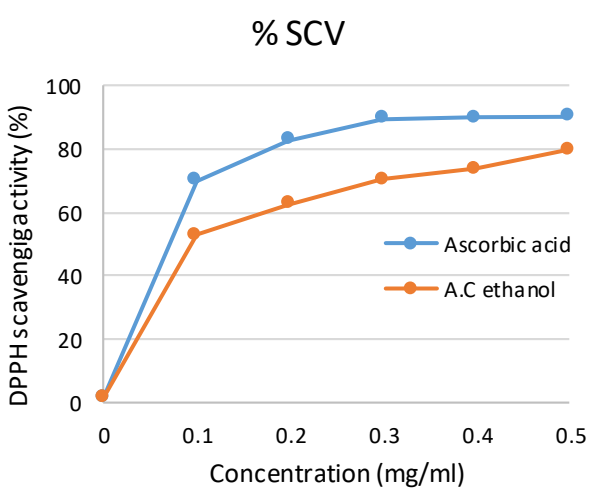

Figure 3.69: DPPH scavenging activities of ethanol extract of *Acacia mearnsii*